Nonlinear dynamics in colloidal model systems under confined flow

vorgelegt von

Diplom-Physiker

Sebastian Reddig

geboren in Berlin

Von der Fakultät II - Mathematik und Naturwissenschaften
der Technischen Universität Berlin
zur Erlangung des akademischen Grades
Doktor der Naturwissenschaften (Dr. rer. nat.)

genehmigte Dissertation

Promotionsauschuss:

Vorsitzender:	Prof. Dr. Martin Schoen
Erster Gutachter:	Prof. Dr. Holger Stark
Zweiter Gutachter:	Prof. Dr. Roland Netz

Tag der wissenschaftlichen Aussprache: 20.11.2013

Berlin 2013

D83

Contents

1 Introduction

«Newton hat ganz Recht, wenn er bemerkt, daß dasjenige, was wir Gesetz in der Natur nennen, eigentlich nicht existiert, und daß es nur Formeln sind, die unserer Fassungskraft zu Hilfe kommen, um eine Reihe von Erscheinungen in der Natur zu erklären.»

Henrich Heine

In the last decades, technology has evolved considerably. For example, the first computers easily filled an entire room, whereas nowadays nearly everyone carries a much more powerful smart device in their pocket. But not only the physical size of computer chips decreased in the recent years, also the size of microfluidic devices changed drastically. Since one can create micrometer or sub-micrometer sized mechanical structures in silicon and other materials it is possible to design devices that integrate one or several laboratory functions on a single chip of only a few square millimeters in size. These so called *Lab on a chip* devices find applications in many physical, biological or chemical systems, such as DNA sequencing, polymerase chain reaction, cell sorting, cell culturing, microfabrication, and as microreactors [1, 2, 3, 4] to name just a few examples. Furthermore, microfluidic channels provide an ideal tool for basic research. They allow controlled studies on the influence of confinement or mimic biological systems where confinement is essential. Examples are the flow of red blood cells through blood vessels or single actin filaments in the actin network of the cell cortex [5]. Most importantly, using the pressure driven Poiseuille flow through a microchannel, one can controllably drive suspended objects out of equilibrium and thereby induce novel and intriguing dynamic structure formation in complex fluids. One thing that all these microfluidic devices have in common is that they crucially depend on the precise manipulation of particles interacting hydrodynamically, such as emulsion droplets, polystyrene microbeads, biological cells, etc. [6, 7, 8]. Therefore, an essential aspect for developing and understanding such devices is the flow induced cross-streamline migration of suspended objects in confined geometries.

Already in 1836, Jean Louis Marie Poiseuille revealed in his pioneering work that blood flow in arterioles and venules features a layer of red blood cell-free plasma near the vessel wall [9]. More than one hundred years later, Segré and Silberberg investigated a dilute suspension of neutrally buoyant rigid particles flowing in circular tube. They found that the particles equilibrates at a distance of 0.6 times the tube radius from the centerline [10]. So, in addition to depletion at confining walls reported in earlier studies [9, 11], migration of the particles away from the channel's centerline occurs. A fundamental consequence of this famous *Segré-Silberberg effect* is that even if the injected particles are uniformly distributed, they move across streamlines and are well focused between the centerline and the wall of the tube while traveling along the channel. This offers potential applications in filtration and separation of bioparticles, such as red blood cells [12, 13, 14]. This effect is confirmed by further experiments [15, 16, 17, 18] and is explained by inertial forces acting on the particles in non-zero Reynolds number flow [19, 20, 21, 22, 23].

At low Reynolds numbers close to zero, where viscous forces dominate over inertial forces, this effect does no longer occur. Single spherical particles just follow the streamlines in a laminar flow as a result of the kinematic reversibility

of the Stokes equations [24], which is explicitly demonstrated in [18, 25]. Therefore, at low Reynolds numbers rigid particles distribute homogeneously across the channel due to Brownian motion, whereas at finite Reynolds numbers they migrate to a position between the channel wall and centerline. However, in dense colloid suspensions the lateral particle profiles also become inhomogeneous [26]. The cross-streamline migration in such dense suspensions gives rise to interesting dynamical patterns in particulate flow, such as the characteristic phonon modes of one-dimensional microfluidic crystals in flat microchannels [27, 28, 29] or the collective dynamics in two-dimensional arrays [30, 31, 32, 33]. To gain a better understanding for the rheology of such suspensions, their relative motion is essential. Whereas the motion of a pair of rigid particles is well studied in bounded and unbounded shear flow [34, 35], there are fewer studies in confined Poiseuille flow.

Cross-streamline migration at low Reynolds numbers is also observed for deformable objects [36], such as a polymers [37, 38, 39], emulsion droplets [40, 41] or red blood cells [42, 43]. Investigations of dilute suspensions of biopolymers in confined flow, such as DNA or actin filaments [44, 45, 46, 47, 48, 49, 50, 51] reveal a depletion of polymers near walls in planar shear flow as well as in Poiseuille flow. In addition, migration away from the channel's centerline is also observed, especially for semiflexible polymers [37, 38, 52]. As a result, the concentration of the polymer becomes bimodally distributed across the channel. Whereas the migration away from bounding channel walls is fully understood in terms of hydrodynamic wall-polymer interactions [53, 54], the migration away from the centerline is explained by a position-dependent diffusivity, which gives rise to a diffusion current away from the center [37, 52].

The focus of this work is to explore the potential of hydrodynamic interactions to induce novel motional patterns in confined flow, and therefore to gain a deeper understanding of relevant physical and biological processes, introduced above.

First, we investigate the cross-streamline migration of semiflexible polymers, which are confined between two planar walls and are driven out of equilibrium using the pressure driven Poiseuille flow. To do so, we perform Brownian dynamics simulations for a bead-spring chain with bending elasticity. Since the dynamics of the bead-spring chain takes place at very low Reynolds numbers, where viscous forces dominate over inertial effects, it is predominantly governed by hydrodynamic interactions between the point-like beads. We take these interactions into account by the two-wall Green tensor of the Stokes equations [55]. Our simulations reproduce the bimodal distribution only when hydrodynamic interactions are taken into account. In addition, we derive a Smoluchowski equation for the center-of-mass distribution and carefully analyze the different contributions to

the probability current that causes the bimodal distribution. We show that the flow-induced deterministic drift current mainly determines the migration away from the centerline, whereas diffusional currents due to a position-dependent diffusivity become less important with increasing polymer stiffness.

Then, we investigate the dynamics of a pair of force- and torque-free spherical colloids, whose diameter is comparable to the distance of the two walls. For this situation, we can no longer work with the simplified point particles but have to take into account their finite size. We determine the grand mobility matrix using a multipole expansion of the force densities on the spheres and taking into account the imposed Poseuille flow as well as the no-slip condition at both bounding walls [55, 56]. We truncate the expansion after the fifth order in the inverse particle separation and apply a lubrication correction [56] to take nearly touching spheres into account. We show that the bounded Poiseuille flow gives rise to new classes of trajectories resulting in cross-streamline migration. Two particles moving on these new trajectories exhibit either bound or unbound states. In the first case they oscillate on closed trajectories in the center-of-mass frame. In the second case, they exhibit cross-swapping trajectories in addition to swapping trajectories which were already observed in unbounded or bounded linear shear flow [34, 35]. The different classes of trajectories occur depending on the initial positions of the two particles and their size. We present state diagrams in the lateral positions, where we categorize the trajectories and color code the oscillation frequencies of the bound states. Finally, we discuss how the results on the two-particle system help to understand the stability of particle trains composed of several particles.

This work is organized as follows:

Chapter 2 In this chapter, we introduce the hydrodynamic equations, which are the basis to describe the interactions of suspended particles. We first briefly derive the Stokes equations, which govern the dynamics of a Newtonian fluid at low Reynolds number. We then introduce the concepts to describe hydrodynamic interactions of spherical particles suspended in an unbounded fluid as well as in a bounded fluid under the influence of a pressure driven Poiseuille flow. At the end of this chapter we also guide through the Stokesian dynamics simulation method, which is used in the present work.

Chapter 3 In this chapter, we introduce the basic concept of Brownian motion. First, we present the Langevin equation, a stochastic differential equation describing the time evolution of the suspended particles. We then introduce an equivalent approach to consider the probability distribution of the particles, which is given by the Smoluchowski equation. At the end of this chapter we guide through the method of Brownian dynamics simulation.

Chapter 4 In this chapter, we present and discuss our numerical results for a bead-spring chain as model for a semiflexible polymer in confined Poiseuille flow. After introducing the model system, we analyze the steady-state probability distribution for the center of mass and study both conformation and orientational order of the polymer in the channel. Then, we derive the Smoluchowski equation for the center-of-mass distribution and investigate the different contributions to the probability current.

Chapter 5 In this chapter, we investigate the nonlinear dynamics of a pair of force and torque-free spherical particles in Poiseuille flow. First we introduce the model and analyze the particle trajectories for different lateral and axial initial positions of the two particles as well as for different particle sizes. Finally, we discuss how the results on the two-particle system help to understand the stability of particle trains composed of several particles.

Chapter 6 In this chapter, we summarize and conclude our results.

2 Hydrodynamics at low Reynolds number

«... the scientist finds his reward in what Henri Poincaré calls the joy of comprehension, and not in the possibilities of application to which any discovery of his may lead.»

Albert Einstein

Hydrodynamic interactions play an important role whenever two or more particles move in a viscous fluid. Due to their long-range nature, the dynamics of colloidal suspensions are governed by these interactions. Since the suspended particles are much larger than the solvent molecules, the fluid can be considered to be continuous on the length scale of the colloids. The mechanical state of the fluid is described by the local flow velocity $\boldsymbol{u}(\boldsymbol{r}, t)$ at the position $\boldsymbol{r}$ in the fluid at some time t, the pressure $p(\boldsymbol{r}, t)$ and the mass density $\rho(\boldsymbol{r}, t)$. For our purpose the mass density is considered to be constant, both spatially and in time. This *incompressibility* is a good approximation for a wide range of fluids, such as water. The remaining two variables which describe the state of the fluid are governed by the incompressibility condition and the *Navier-Stokes equation* which is Newton's equation of motion for the fluid flow.

So, in principle, if the spatial distribution of the suspended particles is given along with their motions, one has to solve a well defined boundary value problem for the Navier-Stokes equation to describe the flow field $\boldsymbol{u}(\boldsymbol{r}, t)$. To do so, various numerical techniques have been developed in the recent years. One kind of simulations methods are coarse grained molecular dynamic techniques, such as the lattice Boltzmann technique [57, 58], dissipative particle dynamics [59, 60], multiparticle collision dynamics [61, 62] or stochastic rotation dynamics [63]. In all these concepts the fluid is described by "effective" fluid particles satisfying the fundamental balance equations of continuum theory. These fluid particles are on a larger scale than single solvent molecules but still smaller than the suspended colloids.

In the regime of low Reynolds number, where viscous forces dominate over inertial forces, the fluid dynamics is governed by the *Stokes equations*, which are both linear and independent of time. These equations can be solved using the method of Green's functions, which leads to the technique of Stokesian dynamics simulation [24, 64, 65]. This concept follows a different path. Instead of calculating the flow field explicitly it solves Newton's equation of motion for the colloidal particles only. The hydrodynamic coupling through the fluid flow is taken into account by the *mobility matrix* $\boldsymbol{\mu}$ or its inverse the *friction matrix* $\boldsymbol{\zeta} = \boldsymbol{\mu}^{-1}$, which describe the relation between the particles velocities and the hydrodynamic forces and torques.

In this chapter we introduce the essentials of the theory as well as methods to obtain expressions for mobility matrix in confined *Poiseuille flow*. At the end of this chapter we also guide through the numerical simulation method, which is used in the present work.

2.1 Hydrodynamic equations

In this section we introduce the theoretical concepts to describe the fluid dynamics, which are governed by the fundamental equations: the *continuity equation* and the Navier-Stokes equation, which can be simplified to the *Stokes equations* in the creeping flow regime.

2.1.1 Continuity equation and incompressibility

We consider a arbitrary volume V with the boundary surface ∂V, which is fixed in space. The total mass M of this volume is given by

$$M = \int_V \rho(\boldsymbol{r}, t)\ \mathrm{d}r^3 \tag{2.1}$$

where $\rho(\boldsymbol{r}, t)$ is the mass density, which is, in gerneral, a function of space $\boldsymbol{r}$ and time t. Since matter is neither created nor destroyed the number of fluid molecules flowing through the boundary ∂V must be equal to the number flowing outwards through ∂V.

$$\frac{\mathrm{d}}{\mathrm{d}t}M = \int_V \frac{\partial}{\partial t}\rho(\boldsymbol{r}, t)\ \mathrm{d}r^3 = -\oint_{\partial V} \boldsymbol{j}(\boldsymbol{r}, t) \cdot \boldsymbol{n}\ \mathrm{d}r^2. \tag{2.2}$$

Here, $\boldsymbol{j}(\boldsymbol{r}, t) = \rho(\boldsymbol{r}, t)\boldsymbol{u}(\boldsymbol{r}, t)$ is the flux of mass and $\boldsymbol{u}(\boldsymbol{r}, t)$ denotes the flow field.[1]. Using Gauss's law on the right hand side of equation (2.2) we obtain the well known continuity equation [24]

$$\frac{\partial}{\partial t}\rho(\boldsymbol{r}, t) + \nabla \cdot \boldsymbol{j}(\boldsymbol{r}, t) = 0, \tag{2.3}$$

where $\nabla = (\frac{\partial}{\partial x}, \frac{\partial}{\partial y}, \frac{\partial}{\partial z})$ denotes the Nabla operator. We consider the fluid to be incompressible, so that the mass density is constant, both spatially and in time $\rho(\boldsymbol{r}, t) = \rho$. Together with the continuity equation (2.3) we obtain the following condition for the flow field

$$\nabla \cdot \boldsymbol{u}(\boldsymbol{r}, t) = 0, \tag{2.4}$$

which is referred to as *incompressibility condition*. Note that this equation (2.4) is not sufficient to determine the flow field $\boldsymbol{u}(\boldsymbol{r}, t)$, it has to be supplemented by Newton's equation of motion for the fluid flow, the Navier-Stokes equation.

[1] In the present work, the dot symbol "$\cdot$" denotes the Euclidean scalar product of two vectors $\boldsymbol{a}$ and $\boldsymbol{b}$: $\boldsymbol{a}\cdot\boldsymbol{b} = \boldsymbol{b}\cdot\boldsymbol{a} = a_i b_i$. The product of a matrix $\boldsymbol{A}$ and a vector $\boldsymbol{b}$ is given by $(\boldsymbol{A}\boldsymbol{b})_i = A_{ij}b_j$, the product of a vector $\boldsymbol{a}$ and a matrix $\boldsymbol{B}$ is given by $(\boldsymbol{a}\boldsymbol{B})_i = a_j B_{ji}$ and the product of the matrices $\boldsymbol{A}$ and $\boldsymbol{B}$ is given by $(\boldsymbol{A}\boldsymbol{B})_{ij} = A_{ik}B_{kj}$. Note that we used Einstein's summation convention.

2.1.2 The Navier-Stokes equation for incompressible fluids

Again, we consider an arbitrary volume V with the boundary ∂V, which is fixed in space. Applying Newtons' second law to the fluid, we get

$$\frac{\mathrm{d}}{\mathrm{d}t}\boldsymbol{P} = \int_V \frac{\partial}{\partial t}\rho\boldsymbol{u}\ \mathrm{d}r^3 = -\oint_{\partial V} \boldsymbol{J}\boldsymbol{n}\ \mathrm{d}r^2 + \oint_{\partial V} \boldsymbol{t}\ \mathrm{d}r^2 + \int_V \boldsymbol{f}\ \mathrm{d}r^3. \tag{2.5}$$

Here, $\boldsymbol{P} = \int_V \rho\boldsymbol{u}\ \mathrm{d}r^3$ is the momentum of the fluid in the volume V. The first term on the right hand sight denotes the surface integral of the momentum current density $\boldsymbol{J} = \rho\boldsymbol{u} \otimes \boldsymbol{u}$[1], which is a tensorial quantity and describes the momentum per area and time, $\boldsymbol{n}$ denotes the surface normal vector. The second term on the right hand side of equation (2.5) describes the surface forces $\boldsymbol{t}(\boldsymbol{r}, t)$ due to interactions with the surrounding fluid and the last term describe the volume forces $\boldsymbol{f}(\boldsymbol{r}, t)$, which represents external forces acting on the fluid, e.g. gravitation. The surface forces are formally given in terms of the stress tensor $\boldsymbol{\sigma}$ [24]

$$\oint_{\partial V} \boldsymbol{t}\ \mathrm{d}r^2 = \oint_{\partial V} \boldsymbol{\sigma}\boldsymbol{n}\ \mathrm{d}r^2 = \int_V \nabla\boldsymbol{\sigma}\ \mathrm{d}r^3, \tag{2.6}$$

where we used Gauss's integral theorem. The divergence of the stress tensor $\nabla\boldsymbol{\sigma}$ can be interpreted as an internal volume force density, whose origin is from the interactions with the surrounding fluid. In general, there are two contributions to this term. One contribution arises from gradients in the hydrodynamic pressure ∇p, which is the only contribution in the static case [24]. So, the static stress tensor

$$\boldsymbol{\sigma}^{\mathrm{static}} = -p\mathbf{1}, \tag{2.7}$$

is proportional to the identity matrix $\mathbf{1}$. The other contribution to the stress tensor arises from the relative motion of neighboring fluid elements, which can be expanded in power series with respect to gradients in the flow velocity. If the velocity gradient are not too large, it is sufficient to take only the linear first order derivatives $\nabla \otimes \boldsymbol{u}$ and $\nabla \cdot \boldsymbol{u}$. For incompressible fluids the divergence $\nabla \cdot \boldsymbol{u} = 0$ vanishes and the only remaining term for an isotropic fluid is the symmetric part $(\nabla \otimes \boldsymbol{u} + (\nabla \otimes \boldsymbol{u})^{\mathrm{T}})$. Here, the subscript T denotes the transpose of the matrix. Finally the full stress tensor for an isotropic incompressible fluid is given by [24]

$$\boldsymbol{\sigma} = -p\mathbf{1} + \eta(\nabla \otimes \boldsymbol{u} + (\nabla \otimes \boldsymbol{u})^{\mathrm{T}}). \tag{2.8}$$

[1]The dyadic product of two vectors $\boldsymbol{a}$ and $\boldsymbol{b}$, denoted by $\boldsymbol{a} \otimes \boldsymbol{b}$, is defined such that the components of the second rank tensor are given by $(\boldsymbol{a} \otimes \boldsymbol{b})_{ij} = a_i b_j$.

The constant η is the (dynamic) *viscosity*, which is specific to each material. Fluids which are described by this equation are referred to as *Newtonian fluids*. Combining this equation together with equation (2.6), we can write equation (2.5) as

$$\int_V \frac{\partial}{\partial t}\rho \boldsymbol{u}\ \mathrm{d}^3 + \oint_{\partial V} \boldsymbol{J}\boldsymbol{n}\ \mathrm{d}r^2 = \int_V (\boldsymbol{f} - \nabla p + \eta\nabla^2\boldsymbol{u})\ \mathrm{d}r^3. \tag{2.9}$$

Again, using Gauss's integral theorem on the second term on the left hand side of this equation together with the continuity equation (2.3), we finally obtain the *Navier-Stokes equation* for incompressible fluids [24, 66, 67]

$$\rho\left(\frac{\partial}{\partial t}\boldsymbol{u} + (\boldsymbol{u}\cdot\nabla)\boldsymbol{u}\right) = \eta\nabla^2\boldsymbol{u} - \nabla p + \boldsymbol{f}. \tag{2.10}$$

2.1.3 The Reynolds number

The magnitude of the various terms in the Navier-Stokes equation (2.10) can vary differently depending on the physical system. In the present work we are interested in the flow field around small particles suspended in water. Let a denote the typical length scale of the physical system (e.g. the radius of the particle), τ the typical time scale and u the typical velocity. Introducing the following rescaled variables

$$\begin{aligned}
\boldsymbol{u}' &= \boldsymbol{u}/u,\\
\boldsymbol{r}' &= \boldsymbol{r}/a,\\
t' &= t/\tau,\\
p' &= p/\frac{v\eta}{a},\\
\boldsymbol{f}' &= \boldsymbol{f}/\frac{v\eta}{a^2},
\end{aligned} \tag{2.11}$$

we obtain the dimensionless Navier-Stokes equation

$$\frac{a^2\rho}{\eta\tau}\frac{\partial}{\partial t'}\boldsymbol{u}' + \mathrm{Re}(\boldsymbol{u}'\cdot\nabla')\boldsymbol{u}' = \nabla'^2\boldsymbol{u}' - \nabla' p' + \boldsymbol{f}'. \tag{2.12}$$

The dimensionless factor Re is the so called *Reynolds number*, which is defined as [24, 67]

$$\mathrm{Re} = \frac{\rho v a}{\eta}. \tag{2.13}$$

This number can be interpreted as the ratio of the inertial force $F^{\mathrm{inert.}} \sim \rho a^2 u^2$ and the dissipative force $F^{\mathrm{dis.}} \sim \eta a u$. If the Reynolds number is small (Re $\ll$

	Reynolds number
A large whale swimming at 10m/s	300000000
A tuna swimming at the same speed	30000000
A duck flying at 20m/s	300000
A large dragonfly going 7m/s	30000
A copepod in a speed burst of 0.2m/s	300
Flapping wings of the smallest flying insects	30
An invertebrata larva, 0.3mm long at 1mm/s	0.3
A sea urchin sperm advancing the species at 0.2mm/s	0.03
A bacterium, swimming at 0.01mm/s	0.00001

Table 2.1: A spectrum of Reynolds numbers for different sized organisms (after Vogel [68])

1) the friction terms on the right hand side of the Navier-Stokes equation are important, whereas for high Reynolds number ($\mathrm{Re} \gg 1$) the nonlinear convective term on the left hand side dominates, which causes turbulence. Table (2.1) shows the Reynolds number for different sized organisms.

In the present work we are interested in spherical colloids ($a = 0.025\mu$m to 4μm) suspended in water ($\rho \approx 1\mathrm{g/cm}^3$, $\eta \approx 1\mathrm{mPa}\cdot\mathrm{s}$) and moving in a *Poiseuille flow* with a flow velocity of $u \approx 1$mm/s. For this situation, the Reynolds number is in the order of

$$\mathrm{Re} = 2.5 \cdot 10^{-5} \text{ to } 4 \cdot 10^{-3} \ll 1. \tag{2.14}$$

Therefore, we can neglect the convective term $(\boldsymbol{u} \cdot \nabla)\boldsymbol{u}$ in the Navier-Stokes equation (2.10) and obtain the *time-dependent Stokes equation*

$$\rho \frac{\partial}{\partial t}\boldsymbol{u} = \eta \nabla^2 \boldsymbol{u} - \nabla p + \boldsymbol{f}. \tag{2.15}$$

The flow described by this linear partial differential equation is laminar and no turbulence occurs [24]. Also, due to the linearity of equation (2.15) the principle of superposition is valid.

2.1.4 The Stokes equations

In section 2.1.3 we showed that for small Reynolds number the Navier-Stokes equation simplifies to the time-dependent Stokes equation (2.15), but so far we did

not specified the time scale τ that is relevant for the dynamics to be considered. To do so, we consider the equation of motion for a free particle with mass m and friction coefficient ζ suspended in a fluid

$$m\dot{\boldsymbol{v}} + \zeta \boldsymbol{v} = 0. \tag{2.16}$$

The time that the particle takes to lose its initial momentum due to the friction is given by the momentum relaxation time τ_r, which follows from equation (2.16) as

$$\tau_\mathrm{r} = \frac{m}{\zeta}. \tag{2.17}$$

As we will see in section 2.3.1, the friction coefficient of a spherical particle is $\zeta = 6\pi\eta a$. So, we can write down the time-dependent Stokes equation (2.15) in dimensionless form as

$$\frac{9}{2}\frac{\rho}{\rho_\mathrm{p}}\frac{\tau_\mathrm{r}}{\tau}\frac{\partial}{\partial t'}\boldsymbol{u}' = \nabla'^2\boldsymbol{u}' - \nabla' p' + \boldsymbol{f}', \tag{2.18}$$

where $\rho_\mathrm{p} = m/(4/3\pi a^3)$ is the mass density of the suspended particle. For spherical colloids the momentum relaxation time τ_r ranges typically from 1ns to 100ns, whereas the relevant time scale τ in experimental observations, which is referred to as the *Brownian timescale*, ranges from 1ms to 1s [24], hence $\tau \gg \tau_\mathrm{r}$. Furthermore, we can assume that the mass densities are in the same order of magnitude $\rho \approx \rho_\mathrm{p}$. Therefore, at low Reynolds number and on the Brownian time scale we can neglect the inertial terms on the left hand side of the Navier-Stokes equation (2.10). The *over-damped* fluid dynamics is then well described by the so called *Stokes equation* [24, 64]

$$\begin{aligned} \nabla p - \eta\nabla^2\boldsymbol{u} &= \boldsymbol{f}, \\ \nabla\cdot\boldsymbol{u} &= 0, \end{aligned} \tag{2.19}$$

where the last equation in (2.19) is just again the incompressibility condition (2.4). These two equations are also referred to as *creeping-flow equations*.

2.2 Solutions of the Stokes equations

As we showed in section 2.1, in the creeping-flow regime the fluid dynamics is described by the Stokes equation and the incompressibility condition (2.19). In this section we discuss the solutions to these equations.

2.2.1 Green's function of the Stokes equations

We consider an external force acting only at a single point $\boldsymbol{r}'$ in the fluid. Mathematically, this point force is described by a delta distribution

$$\boldsymbol{f} = \delta(\boldsymbol{r} - \boldsymbol{r}')\boldsymbol{F}, \tag{2.20}$$

where $\boldsymbol{F}$ is the total force acting on the fluid. Due to the linearity of the Stokes equations (2.19) the fluid flow $\boldsymbol{u}(\boldsymbol{r})$ and the pressure field $p(\boldsymbol{r})$ at some point $\boldsymbol{r}$ are directly proportional to the force

$$\begin{aligned} \boldsymbol{u}(\boldsymbol{r}) &= \boldsymbol{T}(\boldsymbol{r}, \boldsymbol{r}')\boldsymbol{F}, \\ p(\boldsymbol{r}) &= \boldsymbol{g}(\boldsymbol{r}, \boldsymbol{r}') \cdot \boldsymbol{F}. \end{aligned} \tag{2.21}$$

The matrix $\boldsymbol{T}(\boldsymbol{r}, \boldsymbol{r})$ and the vector $\boldsymbol{g}(\boldsymbol{r}, \boldsymbol{r}')$ are the Green's functions of the Stokes equations for the flow $\boldsymbol{u}(\boldsymbol{r})$ and the pressure field $p(\boldsymbol{r})$. They connect the point force at a point $\boldsymbol{r}'$ to the resulting flow velocity and pressure at a point $\boldsymbol{r}$. The velocity field of a point force is also referred to as *Stokeslet* [69].

For a continuous force density $\boldsymbol{f}(\boldsymbol{r})$ the flow and the pressure field at some point $\boldsymbol{r}$ are just the superpositions of the fields resulting from the forces acting in each point of the fluid [24]

$$\begin{aligned} \boldsymbol{u}(\boldsymbol{r}) &= \int \boldsymbol{T}(\boldsymbol{r}, \boldsymbol{r}')\boldsymbol{f}(\boldsymbol{r}') \, \mathrm{d}r'^3, \\ p(\boldsymbol{r}) &= \int \boldsymbol{g}(\boldsymbol{r}, \boldsymbol{r}') \cdot \boldsymbol{f}(\boldsymbol{r}') \, \mathrm{d}r'^3. \end{aligned} \tag{2.22}$$

Once these Green's functions are known and the external force is specified, we can calculate the resulting flow velocity and pressure using the equations above. In the following we introduce expressions for Green's functions for an unbounded fluid. For this situation the matrix $\boldsymbol{T}(\boldsymbol{r}, \boldsymbol{r}')$ is called *Oseen tensor*, which we will denote by the superscript O.

2.2.2 The Oseen tensor

To calculate the Oseen tensor $\boldsymbol{T}^{\mathrm{O}}(\boldsymbol{r}, \boldsymbol{r}')$ and the pressure vector $\boldsymbol{g}^{\mathrm{O}}(\boldsymbol{r}, \boldsymbol{r}')$[1] we substitute the integral representation of the fluid flow and the pressure field (2.22) into the Stokes equations (2.19). This leads to

$$\begin{aligned} \int \left[\nabla \otimes \boldsymbol{g}^{\mathrm{O}}(\boldsymbol{r}, \boldsymbol{r}') - \eta\nabla^2\boldsymbol{T}^{\mathrm{O}}(\boldsymbol{r}, \boldsymbol{r}') - \mathbf{1}\delta(\boldsymbol{r} - \boldsymbol{r}')\right] \boldsymbol{f}(\boldsymbol{r}') \, \mathrm{d}r'^3 &= 0, \\ \int \left[\nabla \boldsymbol{T}^{\mathrm{O}}(\boldsymbol{r}, \boldsymbol{r}')\right] \cdot \boldsymbol{f}(\boldsymbol{r}') \, \mathrm{d}r'^3 &= 0. \end{aligned} \tag{2.23}$$

[1] Note that the superscript O in $\boldsymbol{g}^{\mathrm{O}}(\boldsymbol{r}, \boldsymbol{r}')$ denotes the pressure vector for the unbounded geometry.

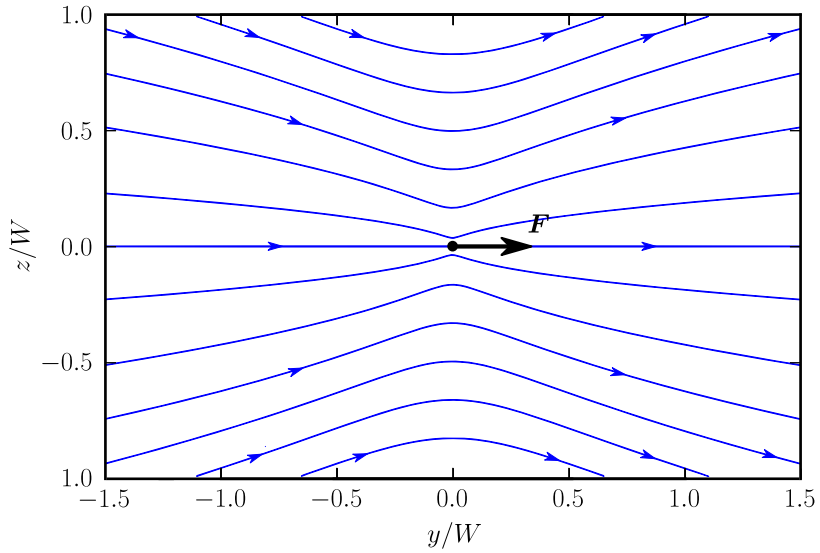

Figure 2.1: Flow field around a point force acting at the origin in the fluid. The y and z coordinates are rescaled using a typical length scale W of the system.

Since this equation is valid for any arbitrary external force density $\boldsymbol{f}(\boldsymbol{r})$, the expressions in the brackets have to be equal to zero. So, that the Green's functions have to satisfy the following differential equations

$$\begin{aligned} \nabla \otimes \boldsymbol{g}^{\mathrm{O}}(\boldsymbol{r},\boldsymbol{r}') - \eta\nabla^2\boldsymbol{T}^{\mathrm{O}}(\boldsymbol{r},\boldsymbol{r}') &= \mathbf{1}\delta(\boldsymbol{r}-\boldsymbol{r}'), \\ \nabla\boldsymbol{T}^{\mathrm{O}}(\boldsymbol{r},\boldsymbol{r}') &= \mathbf{0}. \end{aligned} \tag{2.24}$$

The Green's functions for an unbounded fluid have to vanish at an infinite distance from the point force ($\boldsymbol{T}^{\mathrm{O}}(\boldsymbol{r},\boldsymbol{r}') \to 0$ and $\boldsymbol{g}^{\mathrm{O}}(\boldsymbol{r},\boldsymbol{r}') \to 0$ as $(\boldsymbol{r}-\boldsymbol{r}') \to \infty$). Together with this boundary condition, equation 2.23 can be solved. Hence we obtain the following expressions [24]

$$\begin{aligned} \boldsymbol{T}^{\mathrm{O}}(\boldsymbol{r},\boldsymbol{r}') &= \boldsymbol{T}^{\mathrm{O}}(\boldsymbol{r}-\boldsymbol{r}') = \frac{1}{8\pi\eta|\boldsymbol{r}-\boldsymbol{r}'|}\left(\mathbf{1} + \frac{(\boldsymbol{r}-\boldsymbol{r}')\otimes(\boldsymbol{r}-\boldsymbol{r}')}{|\boldsymbol{r}-\boldsymbol{r}'||\boldsymbol{r}-\boldsymbol{r}'|}\right), \\ \boldsymbol{g}^{\mathrm{O}}(\boldsymbol{r},\boldsymbol{r}') &= \boldsymbol{g}^{\mathrm{O}}(\boldsymbol{r}-\boldsymbol{r}') = \frac{1}{4\pi}\frac{\boldsymbol{r}-\boldsymbol{r}'}{|\boldsymbol{r}-\boldsymbol{r}'|^3}. \end{aligned} \tag{2.25}$$

Note that, due to translational invariance the Oseen tensor $\boldsymbol{T}^{\mathrm{O}}(\boldsymbol{r}-\boldsymbol{r}')$ and the pressure vector $\boldsymbol{g}^{\mathrm{O}}(\boldsymbol{r}-\boldsymbol{r}')$ are functions of the relative vector $\boldsymbol{r}-\boldsymbol{r}'$ only. Or in other words, for an unbounded fluid the position of the origin is not significant. From equation (2.25), we see that the fluid flow around a point force decays with $1/(\boldsymbol{r}-\boldsymbol{r}')$, which means it is a *long ranged* field. In figure 2.1, we show the flow field around a point force (Stokeslet) acting at the origin in the fluid.

2.3 Flow past a sphere

In section 2.2 we introduced the Oseen tensor $\boldsymbol{T}^{\mathrm{O}}(\boldsymbol{r}-\boldsymbol{r}')$, which connects the force acting at a point $\boldsymbol{r}'$ in an unbounded fluid to the flow velocity at some point $\boldsymbol{r}$. In this section we find expressions for the fluid flow around a translating and rotating sphere. For this we consider a sphere with radius a suspended in a quiescent fluid at a position $\boldsymbol{r}_{\mathrm{p}}$. Due to attractive interactions between the fluid particles and the core material of the colloid, the fluid is assumed to "stick" onto the surface of the sphere. Therefore, we assume *stick boundary conditions* throughout this work. Thus the fluid velocity and the particle velocity are the same at the surface ∂V_{p} of the sphere

$$\boldsymbol{u}(\boldsymbol{r}) = \boldsymbol{v}_{\mathrm{p}} + \boldsymbol{\omega}_{\mathrm{p}} \times (\boldsymbol{r}-\boldsymbol{r}_{\mathrm{p}}), \quad \boldsymbol{r} \in \partial V_{\mathrm{p}}. \tag{2.26}$$

Here, $\boldsymbol{v}_{\mathrm{p}}$ denotes the translational velocity of the sphere and $\boldsymbol{\omega}_{\mathrm{p}}$ the angular velocity. The particle exerts a force on the fluid, which is concentrated on its surface. According to equation (2.22), the resulting flow and pressure fields are given by

$$\begin{aligned} \boldsymbol{u}(\boldsymbol{r}) &= \oint_{\partial V_{\mathrm{p}}} \boldsymbol{T}^{\mathrm{O}}(\boldsymbol{r}-\boldsymbol{r}')\boldsymbol{f}_{\mathrm{p}}(\boldsymbol{r}')\ \mathrm{d}r'^2, \\ p(\boldsymbol{r}) &= \oint_{\partial V_{\mathrm{p}}} \boldsymbol{g}^{\mathrm{O}}(\boldsymbol{r}-\boldsymbol{r}')\cdot\boldsymbol{f}_{\mathrm{p}}(\boldsymbol{r}')\ \mathrm{d}r'^2. \end{aligned} \tag{2.27}$$

Note that $\boldsymbol{f}(\boldsymbol{r}')$ is now a force density per unit area that a surface element of the particle exerts on the fluid. For an unbounded fluid, with the boundary condition at infinity

$$\boldsymbol{u}(\boldsymbol{r}) \to \boldsymbol{0}, \quad r \to \infty, \tag{2.28}$$

the flow field around a moving sphere can be calculated exactly. In the following, we discuss the resulting flow past a translating and rotating particle in an unbounded fluid separately.

2.3.1 The flow past a translating sphere

We consider a sphere moving with the constant velocity $\boldsymbol{v}_{\mathrm{p}}$ through an unbounded and quiescent fluid. The stick boundary condition at the particle's surface is given by

$$\boldsymbol{u}(\boldsymbol{r}) = \boldsymbol{v}_{\mathrm{p}}, \quad \boldsymbol{r} \in \partial V_{\mathrm{p}}. \tag{2.29}$$

There are two equivalent methods to calculate the resulting flow field $\boldsymbol{u}$ around this sphere, via the Stokes equations (2.19) or via the integral Green's function representation (2.22). In the following we choose the second option. A successful ansatz for the force density is given in [24]. There, $\boldsymbol{f}_\mathrm{p}(\boldsymbol{r})$ is chosen constant and proportional to the velocity of the sphere

$$\boldsymbol{f}_\mathrm{p} = \frac{c}{4\pi a^2}\boldsymbol{v}_\mathrm{p}, \tag{2.30}$$

where c is a constant. Before inserting the force density in equation (2.27), we first expand the Oseen tensor around the center of the sphere using Taylor's series

$$\boldsymbol{T}^\mathrm{O}(\boldsymbol{r}-\boldsymbol{r}') = \sum_{n=0}^{\infty}\frac{1}{n!}\left[(\boldsymbol{r}'-\boldsymbol{r}_\mathrm{p})\cdot\nabla_{\bar{\boldsymbol{r}}}\right]^n \boldsymbol{T}^\mathrm{O}(\boldsymbol{r}-\bar{\boldsymbol{r}})\Big|_{\bar{\boldsymbol{r}}=\boldsymbol{r}_\mathrm{p}}. \tag{2.31}$$

Here, $\nabla_{\bar{\boldsymbol{r}}}$ denotes the Nabla operator for the position vector $\bar{\boldsymbol{r}}$. Putting this into equation (2.27), we obtain for the fluid flow

$$\begin{aligned}\boldsymbol{u}(\boldsymbol{r}) &= \frac{c}{4\pi a^2}\oint\limits_{\partial V_\mathrm{p}}\sum_{n=0}^{\infty}\frac{1}{n!}\left[(\boldsymbol{r}'-\boldsymbol{r}_\mathrm{p})\cdot\nabla_{\bar{\boldsymbol{r}}}\right]^n \boldsymbol{T}^\mathrm{O}(\boldsymbol{r}-\bar{\boldsymbol{r}})\Big|_{\bar{\boldsymbol{r}}=\boldsymbol{r}_\mathrm{p}}\boldsymbol{v}_\mathrm{p}\,\mathrm{d}r'^2 \\ &= c\left(1+\frac{a^2}{6}\nabla^2_{\bar{\boldsymbol{r}}}\right)\boldsymbol{T}^\mathrm{O}(\boldsymbol{r}-\bar{\boldsymbol{r}})\Big|_{\bar{\boldsymbol{r}}=\boldsymbol{r}_\mathrm{p}}\boldsymbol{v}_\mathrm{p}.\end{aligned} \tag{2.32}$$

Note that higher order terms are proportional to $\nabla^2_{\bar{\boldsymbol{r}}}\nabla^2_{\bar{\boldsymbol{r}}}$, which are identical zero due to the *biharmonic equations*: $\nabla^2\nabla^2\boldsymbol{u} = 0$ [24], such that we obtain for an arbitrary point force $\boldsymbol{F}$ acting at $\boldsymbol{r}'$

$$\nabla^2\nabla^2\boldsymbol{u}(\boldsymbol{r}) \overset{(2.21)}{=} \nabla^2\nabla^2\boldsymbol{T}^\mathrm{O}(\boldsymbol{r}-\boldsymbol{r}')\boldsymbol{F} = 0 \;\Rightarrow\; \nabla^2_{\bar{\boldsymbol{r}}}\nabla^2_{\bar{\boldsymbol{r}}}\boldsymbol{T}^\mathrm{O}(\bar{\boldsymbol{r}})\Big|_{\bar{\boldsymbol{r}}=\boldsymbol{r}-\boldsymbol{r}'} = \boldsymbol{0}, \tag{2.33}$$

for $\boldsymbol{r}\neq\boldsymbol{r}'$. Defining now the translational differential operator

$$\mathcal{L}^\mathrm{t} = \boldsymbol{1} + \frac{a^2}{6}\nabla^2, \tag{2.34}$$

we can express the resulting flow field as

$$\begin{aligned}\boldsymbol{u}(\boldsymbol{r}) &= c\,\mathcal{L}^\mathrm{t}_{\bar{\boldsymbol{r}}}\boldsymbol{T}^\mathrm{O}(\boldsymbol{r}-\bar{\boldsymbol{r}})\Big|_{\bar{\boldsymbol{r}}=\boldsymbol{r}_\mathrm{p}}\boldsymbol{v}_\mathrm{p} \\ &= \frac{c}{6\pi\eta a}\left[\frac{3}{4}\frac{a}{|\boldsymbol{r}-\boldsymbol{r}_\mathrm{p}|}\left(\boldsymbol{1}+\frac{(\boldsymbol{r}-\boldsymbol{r}_\mathrm{p})\otimes(\boldsymbol{r}-\boldsymbol{r}_\mathrm{p})}{|\boldsymbol{r}-\boldsymbol{r}_\mathrm{p}|^2}\right)\right. \\ &\quad \left.+\frac{1}{4}\left(\frac{a}{|\boldsymbol{r}-\boldsymbol{r}_\mathrm{p}|}\right)^3\left(\boldsymbol{1}-3\frac{(\boldsymbol{r}-\boldsymbol{r}_\mathrm{p})\otimes(\boldsymbol{r}-\boldsymbol{r}_\mathrm{p})}{|\boldsymbol{r}-\boldsymbol{r}_\mathrm{p}|^2}\right)\right]\boldsymbol{v}_\mathrm{p}.\end{aligned} \tag{2.35}$$

To satisfy the no-slip condition, the constant c has to be chosen as $c = 6\pi\eta a$. Since c is known, we can now easily calculate the total force that the particle exerts on the fluid

$$\boldsymbol{F}_\mathrm{p} = \oint\limits_{\partial V_\mathrm{p}} \boldsymbol{f}_\mathrm{p}\, \mathrm{d}r^2 = \zeta^t \boldsymbol{v}_\mathrm{p}, \tag{2.36}$$

with the translational friction coefficient

$$\zeta^\mathrm{t} = \frac{1}{\mu^\mathrm{t}} = 6\pi\eta a, \tag{2.37}$$

where μ^t is the translational mobility of the sphere. This is *Stokes friction law for translational motion* of a sphere.

2.3.2 The flow past a rotating sphere

For a sphere, rotating with the constant angular velocity $\boldsymbol{\omega}_\mathrm{p}$, the stick boundary condition on its surface reads

$$\boldsymbol{u}(\boldsymbol{r}) = \boldsymbol{\omega}_\mathrm{p} \times (\boldsymbol{r} - \boldsymbol{r}_\mathrm{p}), \quad \boldsymbol{r} \in \partial V_\mathrm{p}. \tag{2.38}$$

Again, the force density is chosen to be proportional to the velocity of the surface element

$$\boldsymbol{f}_\mathrm{p}(\boldsymbol{r}) = \frac{c}{4\pi a^2} \boldsymbol{\omega}_\mathrm{p} \times (\boldsymbol{r} - \boldsymbol{r}_\mathrm{p}), \tag{2.39}$$

where c is again a constant, which has to be chosen such that the boundary condition (2.38) is fulfilled. Putting this into equation (2.27) yields [24]

$$\boldsymbol{u}(\boldsymbol{r}) = \frac{c}{12\pi\eta a} \left(\frac{a}{|\boldsymbol{r} - \boldsymbol{r}_\mathrm{p}|} \right)^3 \boldsymbol{\omega}_\mathrm{p} \times (\boldsymbol{r} - \boldsymbol{r}_\mathrm{p}), \tag{2.40}$$

Obviously, we have to choose c as $c = 12\pi\eta a$. Therefore, we obtain for the total torque that the rotating sphere exerts on the fluid

$$\boldsymbol{T}_\mathrm{p} = \oint\limits_{\partial V_\mathrm{p}} (\boldsymbol{r}' - \boldsymbol{r}_\mathrm{p}) \times \boldsymbol{f}_\mathrm{p}(\boldsymbol{r}')\, \mathrm{d}r'^2 = \zeta^\mathrm{r} \boldsymbol{\omega}_\mathrm{p}, \tag{2.41}$$

with the rotational friction coefficient

$$\zeta^\mathrm{r} = \frac{1}{\mu^\mathrm{r}} = 8\pi\eta a^3, \tag{2.42}$$

where μ^r is the rotational mobility of the sphere. This is *Stokes friction law for rotational motion* of a sphere.

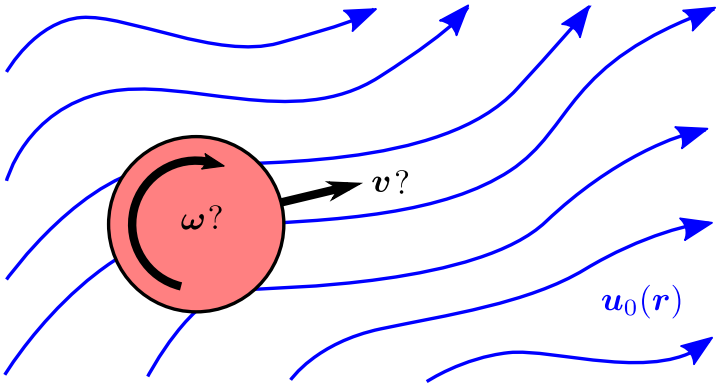

Figure 2.2: A spherical colloid is immersed in a fluid with the flow velocity $\boldsymbol{u}_0(\boldsymbol{r})$. This fluid flow influences the translational and rotational motion of the particle.

2.3.3 Faxén's theorem

So far, we introduced expressions for the fluid flow past a moving sphere. Here, we are interested how a given flow field $\boldsymbol{u}_0(\boldsymbol{r})$ influences the translational and rotational motion of a suspended particle. This flow is a solution of the Stokes equations (2.19) and may represents an imposed flow or the flow field induced by a moving sphere. At the particle's surface, centered at $\boldsymbol{r}_\mathrm{p}$ the stick boundary condition has to be fulfilled

$$\boldsymbol{v}_\mathrm{p} + \boldsymbol{\omega}_\mathrm{p} \times (\boldsymbol{r} - \boldsymbol{r}_\mathrm{p}) = \boldsymbol{u}_0(\boldsymbol{r}) + \oint\limits_{\partial V_\mathrm{p}} \boldsymbol{T}^\mathrm{O}(\boldsymbol{r} - \boldsymbol{r}')\boldsymbol{f}_\mathrm{p}(\boldsymbol{r}')\ \mathrm{d}r'^2,\ \boldsymbol{r} \in \partial V_\mathrm{p}. \tag{2.43}$$

The left hand side of this equation represents the particle's surface velocity and the right hand side the resulting flow field $\boldsymbol{u}(\boldsymbol{r})$, which is the superposition of the incident flow $\boldsymbol{u}_0(\boldsymbol{r})$ in the absence of the particle and the disturbance flow due to the present of the sphere $\oint_{\partial V_\mathrm{p}} \boldsymbol{T}^\mathrm{O}(\boldsymbol{r} - \boldsymbol{r}')\boldsymbol{f}_\mathrm{p}(\boldsymbol{r}')\ \mathrm{d}r'^2$. Multiplying this equation with $1/(4\pi a^2)$ and integrating over the sphere's surface ∂V_p, we obtain [24]

$$\boldsymbol{v}_\mathrm{p} = \mu^\mathrm{t}\boldsymbol{F}_\mathrm{p} + \frac{1}{4\pi a^2} \oint\limits_{\partial V_\mathrm{p}} \boldsymbol{u}_0(\boldsymbol{r})\ \mathrm{d}r^2. \tag{2.44}$$

Again, $\boldsymbol{F}_\mathrm{p} = \oint_{\partial V_\mathrm{p}} \boldsymbol{f}_\mathrm{p}(\boldsymbol{r}')\ \mathrm{d}r'^2$ is the total force that the particle exerts on the fluid. Note that, due to rotational symmetry the integration over the angular velocity in equation (2.43) vanishes. We expand the imposed flow field around the center of the sphere

$$\boldsymbol{u}_0(\boldsymbol{r}) = \sum_{n=0}^{\infty} \frac{1}{n!} \left[(\boldsymbol{r} - \boldsymbol{r}_\mathrm{p}) \cdot \nabla_{\bar{\boldsymbol{r}}}\right]^n \boldsymbol{u}_0(\bar{\boldsymbol{r}})|_{\bar{\boldsymbol{r}}=\boldsymbol{r}_\mathrm{p}} \tag{2.45}$$

and insert this into equation (2.44). As we already discussed in section 2.3.1, higher orders terms are proportional to $\nabla^2_{\bar{\boldsymbol{r}}}\nabla^2_{\bar{\boldsymbol{r}}}$, which vanish due to the biharmonic equations [24]. So finally, we obtain Faxén's theorem for the translational motion of a sphere [24, 64, 70]

$$\begin{aligned} \boldsymbol{v}_{\mathrm{p}} &= \mu^{\mathrm{t}}\boldsymbol{F}_{\mathrm{p}} + \boldsymbol{u}_0(\boldsymbol{r}_{\mathrm{p}}) + \frac{a^2}{6}\nabla^2_{\bar{\boldsymbol{r}}}\,\boldsymbol{u}_0(\bar{\boldsymbol{r}})|_{\bar{\boldsymbol{r}}=\boldsymbol{r}_{\mathrm{p}}} \\ &= \mu^{\mathrm{t}}\boldsymbol{F}_{\mathrm{p}} + \mathcal{L}^{\mathrm{t}}_{\bar{\boldsymbol{r}}}\boldsymbol{u}_0(\bar{\boldsymbol{r}})\Big|_{\bar{\boldsymbol{r}}=\boldsymbol{r}_{\mathrm{p}}}, \end{aligned} \tag{2.46}$$

where $\mathcal{L}^{\mathrm{t}}_{\bar{\boldsymbol{r}}}$ is the translational differential operator (2.34) with respect to $\bar{\boldsymbol{r}}$. Note that in the absence of the incident flow $\boldsymbol{u}_0(\boldsymbol{r}) = \boldsymbol{0}$ this equation reproduces Stoke's friction law for the translational motion (2.36).

Multiplying equation (2.43) with $(\boldsymbol{r} - \boldsymbol{r}_{\mathrm{p}})\times$ and integrating again over the surface of the particle, we obtain Faxén's law for the rotational motion [24, 64, 70]

$$\begin{aligned} \boldsymbol{\omega}_{\mathrm{p}} &= \mu^{\mathrm{r}}\boldsymbol{T}_{\mathrm{p}} + \frac{1}{2}\,\nabla_{\bar{\boldsymbol{r}}} \times \boldsymbol{u}_0(\bar{\boldsymbol{r}})|_{\bar{\boldsymbol{r}}=\boldsymbol{r}_{\mathrm{p}}} \\ &= \mu^{\mathrm{r}}\boldsymbol{T}_{\mathrm{p}} + \boldsymbol{\mathcal{L}}^{\mathrm{r}}_{\bar{\boldsymbol{r}}}\boldsymbol{u}_0(\bar{\boldsymbol{r}})|_{\bar{\boldsymbol{r}}=\boldsymbol{r}_{\mathrm{p}}}. \end{aligned} \tag{2.47}$$

Here, we have introduced the rotational differential operator

$$\boldsymbol{\mathcal{L}}^{\mathrm{r}} = \frac{1}{2}\nabla\times, \tag{2.48}$$

with Cartesian components $(\boldsymbol{\mathcal{L}}^{\mathrm{r}})_{ik} = \frac{1}{2}\epsilon_{ijk}\frac{\partial}{\partial_{x_j}}$, where ϵ_{ijk} is the *Levi-Civita tensor*. In the absence of an external flow $\boldsymbol{u}_0(\boldsymbol{r}) = \boldsymbol{0}$, equation (2.47) reproduces Stoke's friction law for the rotational motion (2.41).

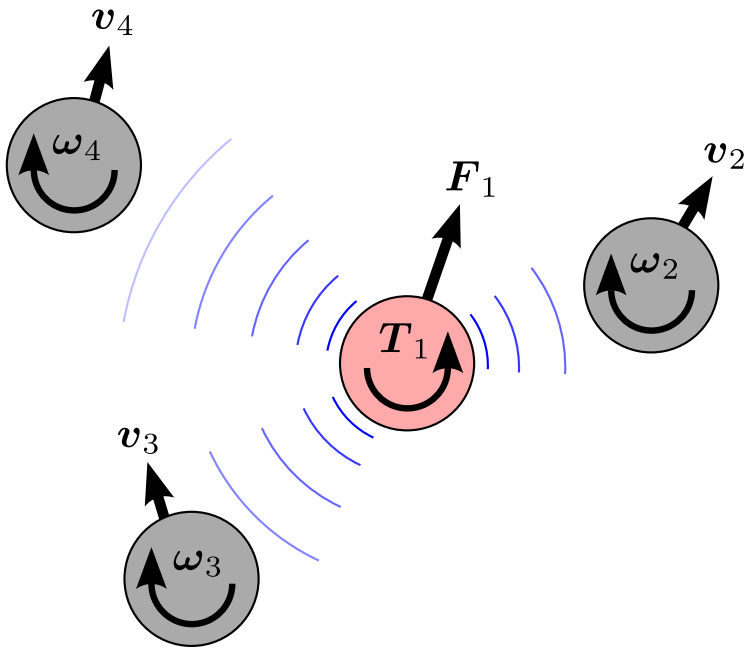

Figure 2.3: Sketch of hydrodynamic interactions. The motion of one sphere, due to external forces and torques acting on it induces a flow field. This fluid flow influences the motion of the other particles and is reflected at its surfaces, so that the translational and rotational motion of all particles are all mutually coupled via the surrounding flow field

2.4 Hydrodynamic interactions

In section 2.3 we calculated the flow field past a moving sphere and described how the particle's motion is influenced by the presence of a given fluid flow. We consider now N spheres suspended in an unbounded and quiescent fluid. External forces $\boldsymbol{F}_i$ and torques $\boldsymbol{T}_i$ are acting on these spheres such that they move with translational and angular velocity $\boldsymbol{v}_i$ and $\boldsymbol{\omega}_i$. The motion of each sphere induces a flow field, which on the other hand influences the motion of the other particles. In this section we introduce the theoretical framework to describe these hydrodynamic interactions.

2.4.1 Hydrodynamic interactions at the Oseen level

We consider N spherical particles suspended in an unbounded and quiescent fluid. Each sphere is subjected to external forces $\boldsymbol{F}_i$ such that they exert the

force density $\boldsymbol{f}_i(\boldsymbol{r})$ on the fluid. Due to the linearity of the Stokes equations (2.19) the resulting flow field reads

$$\boldsymbol{u}(\boldsymbol{r}) = \sum_{j=1}^{N} \oint_{\partial V_j} \boldsymbol{T}^{\mathrm{O}}(\boldsymbol{r}-\boldsymbol{r}')\boldsymbol{f}_j(\boldsymbol{r}')\ \mathrm{d}r'^2. \tag{2.49}$$

If we neglect the rotational motion of the spheres, the stick boundary condition at the surface of particle i is given by

$$\begin{aligned} \boldsymbol{v}_i &= \oint_{\partial V_i} \boldsymbol{T}^{\mathrm{O}}(\boldsymbol{r}-\boldsymbol{r}')\boldsymbol{f}_i(\boldsymbol{r}')\ \mathrm{d}r'^2 \\ &+ \sum_{j\neq i}^{N} \oint_{\partial V_j} \boldsymbol{T}^{\mathrm{O}}(\boldsymbol{r},\boldsymbol{r}')\boldsymbol{f}_j(\boldsymbol{r}')\ \mathrm{d}r'^2, \quad \boldsymbol{r}\in\partial V_i, \end{aligned} \tag{2.50}$$

where $\boldsymbol{v}_i$ is the translational velocity of particle i. Multiplying this equation by $1/(4\pi a^2)$ and integrating both sides over the surface of particle i, we obtain [24]

$$\boldsymbol{v}_i = \mu^{\mathrm{t}}\boldsymbol{F}_i + \frac{1}{4\pi a^2}\oint_{\partial V_i}\sum_{j\neq i}^{N}\oint_{\partial V_j} \boldsymbol{T}^{\mathrm{O}}(\boldsymbol{r}-\boldsymbol{r}')\boldsymbol{f}_j(\boldsymbol{r}')\ \mathrm{d}r'^2\mathrm{d}r^2,\ \boldsymbol{r}\in\partial V_i, \tag{2.51}$$

If the separation of the particles is very large ($|\boldsymbol{r}_i-\boldsymbol{r}_j| \gg 2a$), we can in good approximation evaluate the Oseen tensor at center of the spheres: $\boldsymbol{T}^{\mathrm{O}}(\boldsymbol{r}-\boldsymbol{r}') \approx \boldsymbol{T}^{\mathrm{O}}(\boldsymbol{r}_i-\boldsymbol{r}_j)$ for $\boldsymbol{r}\in\partial V_i$ and $\boldsymbol{r}'\in\partial V_j$. Therefore, equation (2.51) simplifies to

$$\boldsymbol{v}_i = \mu^{\mathrm{t}}\boldsymbol{F}_i + \sum_{j\neq i}^{N}\boldsymbol{T}^{\mathrm{O}}(\boldsymbol{r}_i-\boldsymbol{r}_j)\boldsymbol{F}_j. \tag{2.52}$$

Note, in this far-field approximation the particles are treated as point like particles (Stokeslets). The motion of each particle consists of their own motion (*self mobility*) and the influence of the induced flow fields by the other spheres (*cross mobility*). Introducing the mobility tensor for the translational motion

$$\begin{aligned} \boldsymbol{\mu}_{ii}^{\mathrm{tt}} &= \mu^{\mathrm{t}}\mathbf{1}, \\ \boldsymbol{\mu}_{ij}^{\mathrm{tt}} &= \boldsymbol{T}^{\mathrm{O}}(\boldsymbol{r}_i-\boldsymbol{r}_j) \end{aligned} \tag{2.53}$$

we can describe the many particle interaction completely by

$$\begin{pmatrix} \boldsymbol{v}_1 \\ \vdots \\ \boldsymbol{v}_N \end{pmatrix} = \begin{pmatrix} \boldsymbol{\mu}_{11}^{\mathrm{tt}} & \cdots & \boldsymbol{\mu}_{1N}^{\mathrm{tt}} \\ \vdots & \ddots & \vdots \\ \boldsymbol{\mu}_{N1}^{\mathrm{tt}} & \cdots & \boldsymbol{\mu}_{NN}^{\mathrm{tt}} \end{pmatrix} \begin{pmatrix} \boldsymbol{F}_1 \\ \vdots \\ \boldsymbol{F}_N \end{pmatrix}. \tag{2.54}$$

As we already mentioned, the above expression for the mobility tensor is only valid for far separated particles. They are the leading terms in an expansion with respect to the inverse particle separation a/r_{ij}. To describe the interactions more accurately, higher orders have to be considered. They can be calculated iteratively by the *method of reflections*.

2.4.2 Method of reflections

The idea behind this method is to determine the flow field $\boldsymbol{u}_0(\boldsymbol{r})$ by iteration, where the flow field, induced by the motion of one particle is reflected by the other spheres and then bounces from particle to particle. Consider an external force $\boldsymbol{F}_i$ and torque $\boldsymbol{T}_i$ acting on sphere i at position $\boldsymbol{r}_i$. Then in zeroth order the sphere moves with the velocity (2.36,2.41)

$$\begin{aligned} \boldsymbol{v}_i^0 &= \mu^{\mathrm{t}} \boldsymbol{F}_i, \\ \boldsymbol{\omega}_i^0 &= \mu^{\mathrm{r}} \boldsymbol{T}_i \end{aligned} \tag{2.55}$$

and generates the flow field $\boldsymbol{u}^0(\boldsymbol{r})$, which is the superposition of the velocity field caused by translation (2.35) and rotation of the sphere (2.40). Therefore, the stick boundary condition is fulfilled at this particle's surface ∂V_i. A neighboring particle j at position $\boldsymbol{r}_j$ undergoes this fluid flow. With the help of Faxén's theorem we can calculate its translational and rotational velocities

$$\begin{aligned} \boldsymbol{v}_j^1 &= \mu^{\mathrm{t}} \boldsymbol{F}_j + \mathcal{L}^{\mathrm{t}} \boldsymbol{u}^0(\boldsymbol{r})|_{\boldsymbol{r}=\boldsymbol{r}_j}, \\ \boldsymbol{\omega}_j^1 &= \mu^{\mathrm{r}} \boldsymbol{T}_j + \boldsymbol{\mathcal{L}}^{\mathrm{r}} \boldsymbol{u}^0(\boldsymbol{r})|_{\boldsymbol{r}=\boldsymbol{r}_j}. \end{aligned} \tag{2.56}$$

It is obvious, that the presence of this particle j disturbs the flow $\boldsymbol{u}^0(\boldsymbol{r})$ and an additional contribution $\boldsymbol{u}^1(\boldsymbol{r})$ has to be considered. One says the incident flow field $\boldsymbol{u}^0(\boldsymbol{r})$ is reflected on sphere j. The reflected flow can be calculated by solving the Stokes equations (2.19) considering the boundary condition $\boldsymbol{u}^0(\boldsymbol{r}) + \boldsymbol{u}^1(\boldsymbol{r}) = \boldsymbol{v}_j^1 + \boldsymbol{\omega}_j^1 \times (\boldsymbol{r} - \boldsymbol{r}_j)$ on ∂V_j [24].

On the other hand, the reflected flow influences the motion of particle i. The corrected velocities are given by Faxén's law

$$\begin{aligned} \boldsymbol{v}_i^2 &= \mathcal{L}^{\mathrm{t}} \boldsymbol{u}^1(\boldsymbol{r})|_{\boldsymbol{r}=\boldsymbol{r}_i}, \\ \boldsymbol{\omega}_i^2 &= \boldsymbol{\mathcal{L}}^{\mathrm{r}} \boldsymbol{u}^1(\boldsymbol{r})|_{\boldsymbol{r}=\boldsymbol{r}_i}. \end{aligned} \tag{2.57}$$

Note that here the force $\boldsymbol{F}_i$ and the torque $\boldsymbol{T}_i$ are not considered, since we already took them into account in equation (2.55). The fluid flow $\boldsymbol{u}^0(\boldsymbol{r}) + \boldsymbol{u}^1(\boldsymbol{r})$ is now reflected on particle i and we have to consider the further contribution $\boldsymbol{u}^2(\boldsymbol{r})$, which has to satisfy the boundary condition $\boldsymbol{u}^1(\boldsymbol{r}) + \boldsymbol{u}^2(\boldsymbol{r}) = \boldsymbol{v}_i^2 + \boldsymbol{\omega}_i^2 \times (\boldsymbol{r} - \boldsymbol{r}_i)$ on ∂V_i. Once, $\boldsymbol{u}^2(\boldsymbol{r})$ is obtained, we can calculate it's influence on particle j using Faxén's theorem for $\boldsymbol{F}_j = 0$ and $\boldsymbol{T}_j = 0$. Continuing this procedure, we obtain the series expansion of the exact flow field

$$\boldsymbol{u}(\boldsymbol{r}) = \boldsymbol{u}^0(\boldsymbol{r}) + \boldsymbol{u}^1(\boldsymbol{r}) + \boldsymbol{u}^2(\boldsymbol{r}) + \cdots . \tag{2.58}$$

The corresponding expansion for the velocities of the particles are given by

$$\begin{aligned} \boldsymbol{v}_i &= \boldsymbol{v}_i^0 + \boldsymbol{v}_i^2 + \cdots \quad \text{and} \quad \boldsymbol{v}_j = \boldsymbol{v}_i^1 + \boldsymbol{v}_i^3 + \cdots , \\ \boldsymbol{\omega}_i &= \boldsymbol{\omega}_i^0 + \boldsymbol{\omega}_i^2 + \cdots \quad \text{and} \quad \boldsymbol{\omega}_j = \boldsymbol{\omega}_i^1 + \boldsymbol{\omega}_i^3 + \cdots . \end{aligned} \tag{2.59}$$

Note that, strictly speaking, the above representation of the hydrodynamic interactions are restricted to two particles only. For more than two particles, we additionally have to take into account that the flow field reflected by particle j does not only influences the motion of the original particle i, but also the motion of all other particles. Nevertheless, these results can be used to describe suspension, where the simultaneous hydrodynamic interaction of three or more particles is improbable as compared to pair interactions, which is the case for dilute solutions [24].

The first iteration step (2.56) yields expressions for the particles velocity up to the order of $(a/r_{ij})^3$ [24], which is often referred to as the *Rotne-Prager approxiamtion*[1]. At this level, only pair interactions play a role. Here, the induced flow due to the motion of particle i caused by external forces and torques acting on it is calculated according to equations (2.35) and (2.40). The influence of this flow field on the motion of the other spheres is then simply determined using Faxén's theorem (see section 2.3.3). Therefore, we can write down the N-particle velocities in terms of mobilities

$$\begin{pmatrix} \boldsymbol{v}_1 \\ \vdots \\ \boldsymbol{v}_N \\ \boldsymbol{\omega}_1 \\ \vdots \\ \boldsymbol{\omega}_N \end{pmatrix} = \begin{pmatrix} \boldsymbol{\mu}_{11}^{\mathrm{tt}} & \cdots & \boldsymbol{\mu}_{1N}^{\mathrm{tt}} & \boldsymbol{\mu}_{11}^{\mathrm{tr}} & \cdots & \boldsymbol{\mu}_{1N}^{\mathrm{tr}} \\ \vdots & \ddots & \vdots & \vdots & \ddots & \vdots \\ \boldsymbol{\mu}_{N1}^{\mathrm{tt}} & \cdots & \boldsymbol{\mu}_{NN}^{\mathrm{tt}} & \boldsymbol{\mu}_{N1}^{\mathrm{tr}} & \cdots & \boldsymbol{\mu}_{NN}^{\mathrm{tr}} \\ \boldsymbol{\mu}_{11}^{\mathrm{rt}} & \cdots & \boldsymbol{\mu}_{1N}^{\mathrm{rt}} & \boldsymbol{\mu}_{11}^{\mathrm{rr}} & \cdots & \boldsymbol{\mu}_{1N}^{\mathrm{rr}} \\ \vdots & \ddots & \vdots & \vdots & \ddots & \vdots \\ \boldsymbol{\mu}_{N1}^{\mathrm{rt}} & \cdots & \boldsymbol{\mu}_{NN}^{\mathrm{rt}} & \boldsymbol{\mu}_{N1}^{\mathrm{rr}} & \cdots & \boldsymbol{\mu}_{NN}^{\mathrm{rr}} \end{pmatrix} \begin{pmatrix} \boldsymbol{F}_1 \\ \vdots \\ \boldsymbol{F}_N \\ \boldsymbol{T}_1 \\ \vdots \\ \boldsymbol{T}_N \end{pmatrix} \tag{2.60}$$

with

$$\begin{aligned} \boldsymbol{\mu}_{ii}^{\mathrm{tt}} &= \mu^{\mathrm{t}}\mathbf{1}, \\ \boldsymbol{\mu}_{ii}^{\mathrm{rr}} &= \mu^{\mathrm{r}}\mathbf{1}, \\ \boldsymbol{\mu}_{ii}^{\mathrm{rt}} &= \boldsymbol{\mu}_{ii}^{\mathrm{tr}} = \mathbf{0}, \\ \boldsymbol{\mu}_{ij}^{\mathrm{tt}} &= \mathcal{L}_{\bar{\boldsymbol{r}}'}^{\mathrm{t}}\mathcal{L}_{\bar{\boldsymbol{r}}}^{\mathrm{t}}\boldsymbol{T}^{\mathrm{O}}(\bar{\boldsymbol{r}}' - \bar{\boldsymbol{r}})\Big|_{\bar{\boldsymbol{r}}'=\boldsymbol{r}_i,\bar{\boldsymbol{r}}=\boldsymbol{r}_j}, \\ \boldsymbol{\mu}_{ij}^{\mathrm{rt}} &= (\boldsymbol{\mu}_{ji}^{\mathrm{tr}})^{\mathrm{T}} = \mathcal{L}_{\bar{\boldsymbol{r}}'}^{\mathrm{r}}\mathcal{L}_{\bar{\boldsymbol{r}}}^{\mathrm{t}}\boldsymbol{T}^{\mathrm{O}}(\bar{\boldsymbol{r}}' - \bar{\boldsymbol{r}})\Big|_{\bar{\boldsymbol{r}}'=\boldsymbol{r}_i,\bar{\boldsymbol{r}}=\boldsymbol{r}_j}. \end{aligned} \tag{2.61}$$

An alternative approach to obtain expressions for the many particle mobility matrix $\boldsymbol{\mu}$ is by a multipole expansion, which we will discuss in section 2.5.3.

[1]Usually only the translational part $\boldsymbol{\mu}^{\mathrm{tt}}$ is referred to as the Rotne-Prager tensor [71, 72] (also known as *Yamakawa tensor* [73]). However, in the following we mean the mobility tensor $\boldsymbol{\mu}$ as a whole (equation (2.4.2)), when we consider the Rotne-Prager approximation.

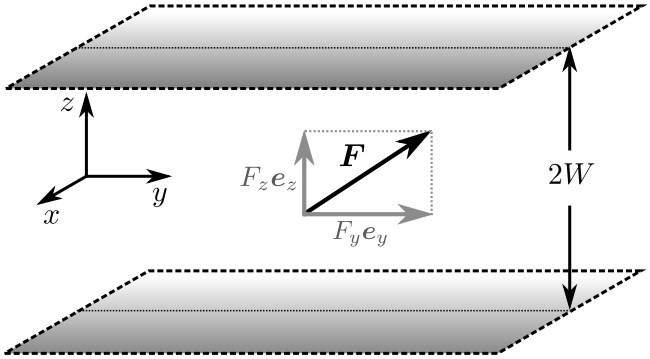

Figure 2.4: Two infinity extended parallel plates with the distance $2W$ are localized at $z = -W$ and $z = W$. The coordinate system is chosen such that an arbitrary force acting on the fluid can be decomposed in components parallel and perpendicular to the walls: $\boldsymbol{F} = \boldsymbol{F}_{\parallel} + \boldsymbol{F}_{\perp} = F_y \boldsymbol{e}_y + F_z \boldsymbol{e}_z$.

2.5 Hydrodynamic interactions between two parallel planar walls in Poiseuille flow

So far we described the hydrodynamic interactions of colloidal particles suspended in an infinite and otherwise quiescent fluid. But in general, the situation differs. Biological and experimental systems are often confined between boundaries and are driven out of equilibrium by an imposed flow. Examples are single actin filaments confined by the dense cytoskeleton network inside cells [5, 74], red blood cells in vessels [75, 76] or colloidal particles in microchannels [77, 78, 79].

In this section we describe the hydrodynamic interactions for a system confined between two parallel planar walls under the influence of an imposed Poiseuille flow. We first briefly derive the corresponding Green's function for this situation and then describe the interactions on the level of point-particles and for extended particles.

2.5.1 The two-wall Green tensor

Let us consider a fluid which is confined between two infinity extended parallel plates with the distance $2W$ (see figure 2.4). The plates are laying in the x-y plane and the origin is located at the center between both plates, so that the walls are localized at $z = -W$ and $z = W$. Consider now a point force acting on the fluid between the two plates at the position $\boldsymbol{r}'$. According to equation (2.21)

the flow field around this point force is given by

$$\boldsymbol{u}(\boldsymbol{r}) \;=\; \boldsymbol{T}^{\mathrm{2W}}(\boldsymbol{r},\boldsymbol{r}')\boldsymbol{F}. \tag{2.62}$$

Here, the superset 2W denotes the Green's tensor of the Stokes equations (2.19) for the bounded geometry. To determine $\boldsymbol{T}^{\mathrm{2W}}(\boldsymbol{r},\boldsymbol{r}')$, we decompose the point force in components parallel and perpendicular to the walls $\boldsymbol{F} = \boldsymbol{F}_{\parallel} + \boldsymbol{F}_{\perp}$ and choose the coordinate system such that $\boldsymbol{F}_{\parallel} = F_y\boldsymbol{e}_y$ (see figure 2.4). Here, $\boldsymbol{e}_y$ is the unit vector along the y-axis. So, we can write down the Stokes equations for the parallel component

$$\begin{aligned} \eta\nabla^2\boldsymbol{u}_{\parallel}(\boldsymbol{r}) - \nabla p_{\parallel}(\boldsymbol{r}) &= -F_y\boldsymbol{e}_y\delta(\boldsymbol{r}-\boldsymbol{r}'), \\ \nabla\cdot\boldsymbol{u}_{\parallel} &= 0. \end{aligned} \tag{2.63}$$

Compared to an unbounded fluid (see section 2.2.2), the presence of the walls violates the translational symmetry along the z direction. Therefore, we expect the two-wall Green's tensor to depend only on the differences $x-x'$ and $y-y'$. Introducing the two dimensional space vector $\boldsymbol{s} = (x-x')\boldsymbol{e}_x + (y-y')\boldsymbol{e}_y$ and the wave vector $\boldsymbol{q} = q_x\boldsymbol{e}_x + q_y\boldsymbol{e}_y$, we perform a Fourier transform in the in the x-y plane [55]

$$\begin{aligned} \boldsymbol{T}^{\mathrm{2W}}(\boldsymbol{s},z,z') &= \int e^{i\boldsymbol{q}\cdot\boldsymbol{s}}\hat{\boldsymbol{T}}^{\mathrm{2W}}(\boldsymbol{q},z,z')\,\mathrm{d}q^2, \\ \boldsymbol{u}_{\parallel}(\boldsymbol{s},z) &= \int e^{i\boldsymbol{q}\cdot\boldsymbol{s}}\hat{\boldsymbol{u}}_{\parallel}(\boldsymbol{q},z)\,\mathrm{d}q^2, \\ p_{\parallel}(\boldsymbol{s},z) &= \int e^{i\boldsymbol{q}\cdot\boldsymbol{s}}\hat{p}_{\parallel}(\boldsymbol{q},z)\,\mathrm{d}q^2, \\ \delta(\boldsymbol{r}-\boldsymbol{r}') &= \frac{1}{(2\pi)^2}\delta(z-z')\int e^{i\boldsymbol{q}\cdot\boldsymbol{s}}\,\mathrm{d}q^2. \end{aligned} \tag{2.64}$$

Inserting these terms into the Stokes equations (2.63), we obtain a coupled system of differential equations for the parallel component [55]

$$\begin{aligned} \eta\left(\frac{\partial^2}{\partial z^2} - q^2\right)\hat{u}_{\parallel x}(\boldsymbol{q},z) - iq_x\hat{p}_{\parallel}(\boldsymbol{q},z) &= 0, \\ \eta\left(\frac{\partial^2}{\partial z^2} - q^2\right)\hat{u}_{\parallel y}(\boldsymbol{q},z) - iq_y\hat{p}_{\parallel}(\boldsymbol{q},z) &= -\frac{F_y}{(2\pi)^2}\delta(z-z'), \\ \eta\left(\frac{\partial^2}{\partial z^2} - q^2\right)\hat{u}_{\parallel z}(\boldsymbol{q},z) - \frac{\partial}{\partial z}\hat{p}_{\parallel}(\boldsymbol{q},z) &= 0, \\ iq_x\hat{u}_{\parallel x}(\boldsymbol{q},z) + iq_y\hat{u}_{\parallel y}(\boldsymbol{q},z) + \frac{\partial}{\partial z}\hat{u}_{\parallel z}(\boldsymbol{q},z) &= 0, \end{aligned} \tag{2.65}$$

where $q^2 = \boldsymbol{q}\cdot\boldsymbol{q}$. Note that the last equation represents the incompressibility condition. The stick boundary condition has to be satisfied at both walls such that all

velocity components $\hat{\boldsymbol{u}}_{\parallel}(\boldsymbol{s}, z)$ have to vanish at $z = \pm W$. From the incompressibility condition we see that in addition $\partial_z \hat{u}_{\parallel z}(\boldsymbol{s}, z)$ must also vanish at $z = \pm W$. Together with these conditions equation (2.65) can be solved completely [55]. Once $\hat{\boldsymbol{u}}_{\parallel z}$ is determined, we can directly read off the components $\hat{T}^{2\mathrm{W}}_{xy}$, $\hat{T}^{2\mathrm{W}}_{yy}$ and $\hat{T}^{2\mathrm{W}}_{zy}$ from equation (2.62). Using reciprocity $\hat{T}^{2\mathrm{W}}_{ij}(\boldsymbol{r}_1, \boldsymbol{r}_2) = \hat{T}^{2\mathrm{W}}_{ji}(\boldsymbol{r}_2, \boldsymbol{r}_1)$ [55, 64] and rotational symmetry about the z-axis, we additional obtain the components $\hat{T}^{2\mathrm{W}}_{yx}$, $\hat{T}^{2\mathrm{W}}_{xx}$, $\hat{T}^{2\mathrm{W}}_{zx}$, $\hat{T}^{2\mathrm{W}}_{xz}$ and $\hat{T}^{2\mathrm{W}}_{yz}$. To obtain $\hat{T}^{2\mathrm{W}}_{zz}$ the whole procedure has to be repeated for the perpendicular force component ($\boldsymbol{F}_{\perp} = F_z \boldsymbol{e}_z$) [55]. Since all components are now known, we can write the two-wall Green tensor in Fourier space as [55]

$$\begin{aligned}\hat{\boldsymbol{T}}^{2\mathrm{W}}(\boldsymbol{q}, z, z') &= \frac{1}{16\pi^2 \eta q}\left(t_{nn}(q,z,z')\boldsymbol{e}_z\boldsymbol{e}_z + i t_{np}(q,z,z')\boldsymbol{e}_z\hat{\boldsymbol{q}} + i t_{pn}(q,z,z')\hat{\boldsymbol{q}}\boldsymbol{e}_z\right. \\ &\quad \left. - t_{pp}(q,z,z')\hat{\boldsymbol{q}}\hat{\boldsymbol{q}} + r_{pp}(q,z,z')(\mathbf{1} - \boldsymbol{e}_z\boldsymbol{e}_z)\right), \end{aligned} \tag{2.66}$$

with $\hat{\boldsymbol{q}} = \boldsymbol{q}/q$ and the scalar functions $t_{nn}, \ldots, r_{pp}$ which are explicitly given in Ref. [55] and Appendix A. Similar to the Blake tensor[1] [80], this solution splits up naturally into the Oseen tensor and a reflectional part

$$\boldsymbol{T}^{2\mathrm{W}}(\boldsymbol{r}, \boldsymbol{r}') = \boldsymbol{T}^{\mathrm{O}}(\boldsymbol{r} - \boldsymbol{r}') + \boldsymbol{T}^{\mathrm{R}}(\boldsymbol{r}, \boldsymbol{r}'). \tag{2.67}$$

Using the polar coordinates $q_x = q\cos\phi$ and $q_y = q\sin\phi$, we transform the two-wall Green tensor back into real space. So, we finally obtain for the reflectional part[2] [55]

$$\begin{aligned} T^{\mathrm{R}}_{xx} &= -\frac{1}{16\pi\eta}\int_0^\infty \left(J_0(qs) + \frac{(y-y')^2 - (x-x')^2}{s^2} J_2(qs)\right) t_{1pp}(q,z,z')\ \mathrm{d}q, \\ &\quad + \frac{1}{8\pi\eta}\int_0^\infty J_0(qs) r_{1pp}(q,z,z')\ \mathrm{d}q, \\ T^{\mathrm{R}}_{zz} &= \frac{1}{8\pi\eta}\int_0^\infty J_0(qs) t_{1nn}(q,z,z')\ \mathrm{d}q, \end{aligned}$$

[1] The Blake tensor is Green's function of the Stokes equations for the fluid flow in the presence of one bounding wall

[2] Note, expressions for the two-wall Green tensor were first derived by Liron and Mochon in 1976 [81]. In analogy to electrostatics, they set up an infinite series of images in order to obey the no-slip boundary condition at the two bounding walls. Since the above integral representation derived by Jones [55] is more symmetric and easier to handle than the original form, we use this representation.

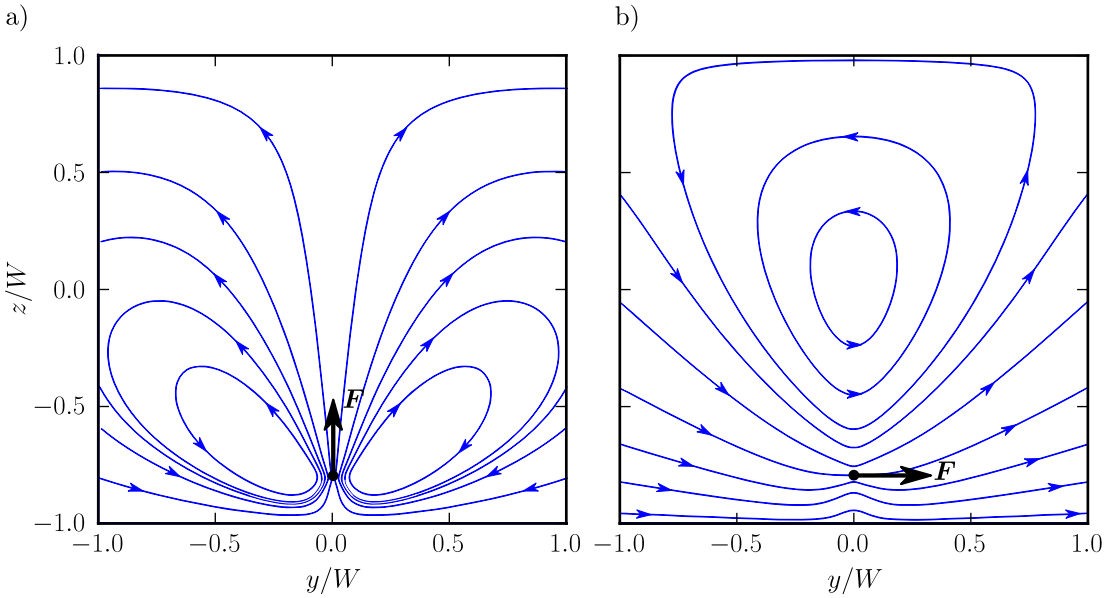

Figure 2.5: Flow field around a point force acting a) perpendicular and b) parallel to the walls. The y and z-axis are rescaled by the distance from the channel center to the walls W.

$$
\begin{aligned}
T^{\mathrm{R}}_{xy} &= \frac{1}{8\pi\eta}\frac{(x-x')(y-y')}{s^2}\int_0^\infty J_2(qs)t_{1pp}(q,z,z')\,\mathrm{d}q,\\
T^{\mathrm{R}}_{xz} &= \frac{1}{8\pi\eta}\frac{x-x'}{s}\int_0^\infty J_1(qs)t_{1pn}(q,z,z')\,\mathrm{d}q.
\end{aligned}
\tag{2.68}
$$

Here, J_n denotes the Bessel function and $s=\sqrt{(x-x')^2+(y-y')^2}$ the distance in the $x-y$ plane. Due to the rotational symmetry abot the z-axis the component T^{R}_{yy} is the same as T^{R}_{xx} with the change $(x-x')\to(y-y')$ and $(y-y')\to(x-x')$, T^{R}_{yz} is the same as T^{R}_{xz} with the change $(x-x')\to(y-y')$. The other components follow from the reciprocal theorem [55, 64]

$$
T^{\mathrm{2W}}_{ij}(\boldsymbol{r},\boldsymbol{r}') = T^{\mathrm{2W}}_{ji}(\boldsymbol{r}',\boldsymbol{r}).
\tag{2.69}
$$

Figure 2.5 shows the flow field around a point force acting on the fluid between the bounding walls.

2.5.2 Hydrodynamic interactions of point-like particles

Let us consider now N spherical particles suspended in a fluid which is confined between two parallel planar walls and undergoing a pressure driven Poiseuille flow

$$\boldsymbol{u}_0(\boldsymbol{r}) = v_0 \left[1 - \left(\frac{z}{W}\right)^2\right] \boldsymbol{e}_y, \tag{2.70}$$

where v_0 is the maximum velocity at the centerline. As we already discussed in section 2.3.3, the resulting flow field is given by the superposition of the imposed flow $\boldsymbol{u}_0(\boldsymbol{r})$ in the absence of the particles and the disturbance flow due to the present of the spheres

$$\boldsymbol{u}(\boldsymbol{r}) = \boldsymbol{u}_0(\boldsymbol{r}) + \sum_{j=1}^{N} \oint_{\partial V_j} \boldsymbol{T}^{2\mathrm{W}}(\boldsymbol{r}, \boldsymbol{r}') \boldsymbol{f}_j(\boldsymbol{r}') \, \mathrm{d}r'^2. \tag{2.71}$$

Since we are here interested only in the hydrodynamic interactions of point-like particles, we neglect again the rotational motion. So, the stick boundary condition on each particle reads

$$\begin{aligned} \boldsymbol{v}_i &= \boldsymbol{u}_0(\boldsymbol{r}) + \oint_{\partial V_i} \boldsymbol{T}^{\mathrm{O}}(\boldsymbol{r}, \boldsymbol{r}') \boldsymbol{f}_i(\boldsymbol{r}') \, \mathrm{d}r'^2 + \oint_{\partial V_i} \boldsymbol{T}^{\mathrm{R}}(\boldsymbol{r}, \boldsymbol{r}') \boldsymbol{f}_i(\boldsymbol{r}') \, \mathrm{d}r'^2 \\ &\quad + \sum_{j \neq i}^{N} \oint_{\partial V_j} \boldsymbol{T}^{2\mathrm{W}}(\boldsymbol{r}, \boldsymbol{r}') \boldsymbol{f}_j(\boldsymbol{r}') \, \mathrm{d}r'^2, \quad \boldsymbol{r} \in \partial V_i. \end{aligned} \tag{2.72}$$

Here, we explicitly split the two-wall Green tensor into the Oseen and reflectional part (2.67). Multiplying this equation by $1/(4\pi a^2)$ and integrating both sides over the surface of particle i, we obtain

$$\begin{aligned} \boldsymbol{v}_i &= \mathcal{L}^{\mathrm{t}} \boldsymbol{u}_0(\boldsymbol{r}) + \mu^{\mathrm{t}} \boldsymbol{F}_i + \frac{1}{4\pi a^2} \oint_{\partial V_i} \oint_{\partial V_i} \boldsymbol{T}^{\mathrm{R}}(\boldsymbol{r}, \boldsymbol{r}') \boldsymbol{f}_i(\boldsymbol{r}') \, \mathrm{d}r'^2 \mathrm{d}r^2 \\ &\quad + \frac{1}{4\pi a^2} \oint_{\partial V_i} \sum_{j \neq i}^{N} \oint_{\partial V_j} \boldsymbol{T}^{2\mathrm{W}}(\boldsymbol{r}, \boldsymbol{r}') \boldsymbol{f}_j(\boldsymbol{r}') \, \mathrm{d}r'^2 \mathrm{d}r^2, \quad \boldsymbol{r} \in \partial V_i, \end{aligned} \tag{2.73}$$

where we used Faxén's formula for the translational motion of a sphere (2.46). Assuming now point particles ($a \to 0$), so that the diameter of the spheres is much smaller than the particles separation, we can approximate $\boldsymbol{T}^{\mathrm{R}}(\boldsymbol{r}, \boldsymbol{r}')$ for $\boldsymbol{r}, \boldsymbol{r}' \in \partial V_i$ and $\boldsymbol{T}^{2\mathrm{W}}(\boldsymbol{r}, \boldsymbol{r}')$ for $\boldsymbol{r} \in \partial V_i$, $\boldsymbol{r}' \in \partial V_j$ by $\boldsymbol{T}^{\mathrm{R}}(\boldsymbol{r}_i, \boldsymbol{r}_i)$ and $\boldsymbol{T}^{2\mathrm{W}}(\boldsymbol{r}_i, \boldsymbol{r}_j)$, respectively. So, we finally obtain

$$\boldsymbol{v}_i = \boldsymbol{u}_0(\boldsymbol{r}_i) + \left[\mu^{\mathrm{t}} \mathbf{1} + \boldsymbol{T}^{\mathrm{R}}(\boldsymbol{r}_i, \boldsymbol{r}_i)\right] \boldsymbol{F}_i + \sum_{j \neq i}^{N} \boldsymbol{T}^{2\mathrm{W}}(\boldsymbol{r}_i, \boldsymbol{r}_j) \boldsymbol{F}_j. \tag{2.74}$$

We can write down this equation in terms of mobilities $\boldsymbol{\mu}_{ij}^{\mathrm{tt}}$, where the self- and cross mobilities for this situation are given by

$$\begin{aligned} \boldsymbol{\mu}_{ii}^{\mathrm{tt}} &= \mu^{\mathrm{t}}\mathbf{1} + \boldsymbol{T}^{\mathrm{R}}(\boldsymbol{r}_i, \boldsymbol{r}_i), \\ \boldsymbol{\mu}_{ij}^{\mathrm{tt}} &= \boldsymbol{T}^{\mathrm{2W}}(\boldsymbol{r}_i, \boldsymbol{r}_j). \end{aligned} \tag{2.75}$$

Therefore, the many particle interaction is completely described by the mobility tensor

$$\begin{pmatrix} \boldsymbol{v}_1 \\ \vdots \\ \boldsymbol{v}_N \end{pmatrix} = \begin{pmatrix} \boldsymbol{u}_0(\boldsymbol{r}_1) \\ \vdots \\ \boldsymbol{u}_0(\boldsymbol{r}_N) \end{pmatrix} + \begin{pmatrix} \boldsymbol{\mu}_{11}^{\mathrm{tt}} & \cdots & \boldsymbol{\mu}_{1N}^{\mathrm{tt}} \\ \vdots & \ddots & \vdots \\ \boldsymbol{\mu}_{N1}^{\mathrm{tt}} & \cdots & \boldsymbol{\mu}_{NN}^{\mathrm{tt}} \end{pmatrix} \begin{pmatrix} \boldsymbol{F}_1 \\ \vdots \\ \boldsymbol{F}_N \end{pmatrix}. \tag{2.76}$$

Note that this expression for the hydrodynamic interactions are only valid for point like particles, which means in this case that not only the separation of the N particles has to be much larger than the particle's diameter but also the channel width $d = 2W$ has to be much larger. The reflectional part of the two-wall Green tensor can be interpreted as an infinite set of mirror images on both walls supplemented by other singularities of the stokes equation to fulfill the stick boundary condition [81]. Therefore, the distance to these mirror particles has to be larger than the particle's size.

In order to describe the hydrodynamic interactions for finite particle sizes, we could use the methods of reflections (see section 2.4.2) and replace the Oseen tensor by the two-wall Green tensor. But since the flow past a moving sphere cannot be exactly calculated for this geometry and the imposed Poiseuille flow has to be taken into account in this framework, we are using an alternative method to obtain expressions for the mobility matrix.

2.5.3 Multipole expansion

An alternative way to calculate the mobility tensor for spherical particles is given by a multipole expansion [55, 82, 83, 84, 85]. Let us consider again N spherical particles confined between two parallel planar walls under the influence of a pressure driven Poiseuille flow $\boldsymbol{u}_0(\boldsymbol{r})$. The presence of the particles disturb this flow, such that the resulting flow field $\boldsymbol{u}(\boldsymbol{r})$ is given by[1]

$$\boldsymbol{u}(\boldsymbol{r}) = \boldsymbol{u}_0(\boldsymbol{r}) + \sum_{j=1}^{N} \int \boldsymbol{T}^{\mathrm{2W}}(\boldsymbol{r}, \boldsymbol{r}') \boldsymbol{f}_j(\boldsymbol{r}') \, \mathrm{d}^3 r'. \tag{2.77}$$

[1]Note that here $\boldsymbol{f}_i(\boldsymbol{r})$ is the force density per unit volume that the particle i exerts on the fluid.

Again, we assume stick boundary conditions, such that the flow velocity $\boldsymbol{u}(\boldsymbol{r})$ is equal to the surface velocity of particle i

$$\boldsymbol{v}_i + \boldsymbol{\omega}_i \times (\boldsymbol{r} - \boldsymbol{r}_i) = \boldsymbol{u}_0(\boldsymbol{r}) + \sum_{j=1}^{N} \int \boldsymbol{T}^{\mathrm{2W}}(\boldsymbol{r}, \boldsymbol{r}') \boldsymbol{f}_j(\boldsymbol{r}') \, \mathrm{d}^3 r', \ \boldsymbol{r} \in \partial V_i. \quad (2.78)$$

We project this integral equation on an appropriate set of complex basis functions to obtain a system of linear algebraic equations, which connects velocity to force multipoles [55, 56]. The basis functions are solutions of the *homogeneous* Stokes equations (equation (2.19) with $\boldsymbol{f} = 0$) [55, 56, 86], for which two sets exist: $\boldsymbol{v}^{+}_{lm\sigma}(\boldsymbol{r})$, which is regular at $\boldsymbol{r} = 0$ and grow at infinity, and $\boldsymbol{v}^{-}_{lm\sigma}(\boldsymbol{r})$, which is singular at $\boldsymbol{r} = \boldsymbol{0}$ and vanish at infinity. They are equivalent to those due to Lamb [87] and explicitly given in Ref. [56]. The indices l, m and σ take the respective values $l = 1, 2, 3, \ldots$, $m = -l, -l+1, \ldots, l-1, l$ and $\sigma = 0, 1, 2$. In terms of these functions we expand the Oseen tensor (2.25) about an arbitrary point $\boldsymbol{R}$ [88]

$$\boldsymbol{T}^{\mathrm{O}}(\boldsymbol{r} - \boldsymbol{r}') = \frac{1}{\eta} \sum_{lm\sigma} \boldsymbol{v}^{-}_{lm\sigma}(\boldsymbol{r}_>) \otimes \boldsymbol{v}^{+*}_{lm\sigma}(\boldsymbol{r}_<), \quad (2.79)$$

where $\boldsymbol{r}_>$, $\boldsymbol{r}_<$ refer, respectively, to the larger and smaller of the relative position vectors $\boldsymbol{r} - \boldsymbol{R}$ and $\boldsymbol{r}' - \boldsymbol{R}$, and the superscript * denotes the complex conjugate. The reflectional part $\boldsymbol{T}^{\mathrm{R}}(\boldsymbol{r}, \boldsymbol{r}')$ can be expanded similarly, but using only the regular functions [55]

$$\boldsymbol{T}^{\mathrm{R}}(\boldsymbol{r}, \boldsymbol{r}') = \sum_{lm\sigma} \sum_{l'm'\sigma'} T^{\mathrm{R}}(lm\sigma, l'm'\sigma') \boldsymbol{v}^{+}_{lm\sigma}(\boldsymbol{r} - \boldsymbol{R}) \otimes \boldsymbol{v}^{+*}_{l'm'\sigma'}(\boldsymbol{r}' - \boldsymbol{R}), \quad (2.80)$$

where $T^{\mathrm{R}}(lm\sigma, l'm'\sigma')$ denotes the expansion coefficients. Expanding now the difference field $\boldsymbol{u}(\boldsymbol{r}) - \boldsymbol{u}_0(\boldsymbol{r})$ in terms of regular solutions centered on the arbitrary point $\boldsymbol{R}$, we obtain

$$\boldsymbol{u}(\boldsymbol{r}) - \boldsymbol{u}_0(\boldsymbol{r}) = \sum_{lm\sigma} c(lm\sigma) \boldsymbol{v}^{+}_{lm\sigma}(\boldsymbol{r} - \boldsymbol{R}). \quad (2.81)$$

Here, $c(lm\sigma)$ denotes the expansion coefficients for the difference field. In order to calculate the expansion coefficients in equation (2.80) and equation (2.81) one needs an adjoint set of functions $\boldsymbol{w}^{\pm}_{lm\sigma}$ [56, 89] which are bi-orthonormal with respect to $\boldsymbol{v}^{\pm}_{lm\sigma}$ on the surface of a sphere of arbitrary radius a in the sense that

$$\left\langle \boldsymbol{w}^{\pm}_{lm\sigma}(\boldsymbol{r}) a^{-1} \delta(r - a) \middle| \, \boldsymbol{v}^{\pm}_{l'm'\sigma'}(\boldsymbol{r}) \right\rangle = \delta_{ll'} \delta_{mm'} \delta_{\sigma\sigma'}. \quad (2.82)$$

Explicit expressions for this adjoint set of functions are given in Ref. [56] and in Appendix A. In analogy to quantum mechanics, we have introduced the scalar product $\langle \boldsymbol{g}(\boldsymbol{r})|\boldsymbol{h}(\boldsymbol{r})\rangle$ between two complex functions $\boldsymbol{g}(\boldsymbol{r})$ and $\boldsymbol{h}(\boldsymbol{r})$ as

$$\langle \boldsymbol{g}(\boldsymbol{r})|\boldsymbol{h}(\boldsymbol{r})\rangle = \int \boldsymbol{g}^*(\boldsymbol{r}) \cdot \boldsymbol{h}(\boldsymbol{r}) \, \mathrm{d}r^3. \tag{2.83}$$

Therefore, we can calculate the expansion coefficients for the difference field $\boldsymbol{u}(\boldsymbol{r}) - \boldsymbol{u}_0(\boldsymbol{r})$ expanded around the center of particle i

$$\begin{aligned} c(ilm\sigma) &= \left\langle \boldsymbol{w}^+_{lm\sigma}(i)\delta_i \middle| \, \boldsymbol{u}(\boldsymbol{r}) - \boldsymbol{u}_0(\boldsymbol{r}) \right\rangle \\ &\overset{(2.77,2.78)}{=} \left\langle \boldsymbol{w}^+_{lm\sigma}(i)\delta_i \middle| \, \boldsymbol{v}_i + \boldsymbol{\omega}_i \times (\boldsymbol{r} - \boldsymbol{r}_i) - \boldsymbol{u}_0(\boldsymbol{r}) \right\rangle . \end{aligned} \tag{2.84}$$

where $c(ilm\sigma)$ denotes the expansion coefficient expanded around the center of particle i, $\boldsymbol{w}^+_{lm\sigma}(i)$ is short for $\boldsymbol{w}^+_{lm\sigma}(\boldsymbol{r} - \boldsymbol{r}_i)$, δ_i is short for $a^{-1}\delta(|\boldsymbol{r} - \boldsymbol{r}_i| - a)$ and a denotes the radius of the spheres. Using the right hand side of equation (2.78) and inserting the two-wall Green tensor expanded around the center of particle j yields the linear relation [56]

$$\begin{aligned} c(ilm\sigma) &= \sum_{j=1}^{N} \left\langle \boldsymbol{w}^+_{lm\sigma}(i)\delta_i \middle| \, \boldsymbol{T}^{2\mathrm{W}}(\boldsymbol{r}, \boldsymbol{r}') \middle| \, \boldsymbol{f}_j(\boldsymbol{r}') \right\rangle \\ &= \sum_{jl'm'\sigma'} M(ilm\sigma, jl'm'\sigma') f(jl'm'\sigma') \end{aligned} \tag{2.85}$$

between the coefficients $c(ilm\sigma)$, also called the velocity multipole moments and the force multipole moments $f(jl'm'\sigma')$, which are defined as

$$f(jl'm'\sigma') = \left\langle \boldsymbol{v}^+_{l'm'\sigma'}(j) | \boldsymbol{f}_j \right\rangle . \tag{2.86}$$

The infinite-dimensional matrix

$$M(ilm\sigma, jl'm'\sigma') = \left\langle \boldsymbol{w}^+_{lm\sigma}(i)\delta_i | \boldsymbol{T}^{2\mathrm{W}} | \boldsymbol{w}^+_{l'm'\sigma'}(j)\delta_j \right\rangle \tag{2.87}$$

represents the two-wall Green function. One writes equation (2.85) in a symbolic notation,

$$\mathrm{c} = \mathrm{Mf}. \tag{2.88}$$

where c and f are infinite dimensional vectors with respective components $c(ilm\sigma)$ and $f(ilm\sigma)$ and matrix M contains the elements $M(ilm\sigma, jl'm'\sigma')$, which is composed of $\mathrm{M} = \mathrm{M}_0 + \mathrm{T}_0^{\mathrm{R}} + \mathrm{M}_1 + \mathrm{T}_1^{\mathrm{R}}$. Here, $\mathrm{M}_0, \mathrm{M}_1$ arise from the Oseen tensor and $\mathrm{T}_0^{\mathrm{R}}, \mathrm{T}_1^{\mathrm{R}}$ from the reflectional part, M_1 and $\mathrm{T}_1^{\mathrm{R}}$ are off diagonal in particle labels ($i \neq j$), while M_0 and $\mathrm{T}_0^{\mathrm{R}}$ are diagonal and contain the single particle contribution ($i = j$). Inverting equation (2.88) gives

$$\mathrm{f} = \mathrm{Zc}, \quad \mathrm{Z} = \mathrm{M}^{-1}, \tag{2.89}$$

where Z denotes the friction matrix for this situation. Note that the equations (2.88) and (2.89) are exact and compared to equation (2.4.2) the knowledge and construction of the flow field $\boldsymbol{u}(\boldsymbol{r})$ is not needed. The complex quantities in equation (2.88) and (2.89) can be transformed to a real basis, where for example the velocities $\boldsymbol{v}_i$ and $\boldsymbol{\omega}_i$ of particle i are linear combinations of the first multipole orders $c(i1m0)$ and $c(i1m1)$. Likewise the forces $\boldsymbol{F}_i$ and torques $\boldsymbol{T}_i$ correspond to the first order multipoles $f(i1m0)$ and $f(i1m1)$ [55]. So, we can rewrite equation (2.89) in an equivalent real Cartesian representation (details are given in Ref. [56])

$$\begin{pmatrix} \boldsymbol{F} \\ \boldsymbol{T} \\ \boldsymbol{E} \\ \boldsymbol{H}^k \\ \vdots \end{pmatrix} = \begin{pmatrix} \boldsymbol{\zeta}^{\mathrm{tt}} & \boldsymbol{\zeta}^{\mathrm{tr}} & \boldsymbol{\zeta}^{\mathrm{td}} & \boldsymbol{\zeta}_k^{\mathrm{th}} & \cdots \\ \boldsymbol{\zeta}^{\mathrm{rt}} & \boldsymbol{\zeta}^{\mathrm{rr}} & \boldsymbol{\zeta}^{\mathrm{rd}} & \boldsymbol{\zeta}_k^{\mathrm{rh}} & \cdots \\ \boldsymbol{\zeta}^{\mathrm{dt}} & \boldsymbol{\zeta}^{\mathrm{dr}} & \boldsymbol{\zeta}^{\mathrm{dd}} & \boldsymbol{\zeta}_k^{\mathrm{dh}} & \cdots \\ \boldsymbol{\zeta}^{\mathrm{ht}} & \boldsymbol{\zeta}^{\mathrm{hr}} & \boldsymbol{\zeta}^{\mathrm{hd}} & \boldsymbol{\zeta}_k^{\mathrm{hh}} & \cdots \\ \vdots & \vdots & \vdots & \vdots & \ddots \end{pmatrix} \begin{pmatrix} \boldsymbol{v} - \boldsymbol{u}_0 \\ \boldsymbol{\omega} - \boldsymbol{\omega}_0 \\ -\boldsymbol{g}_0 \\ -\boldsymbol{h}_0^k \\ \vdots \end{pmatrix}. \tag{2.90}$$

The column vector on the left-hand side contains the known force multipoles acting on the particles. Here, $\boldsymbol{F} = (\boldsymbol{F}_1, \ldots, \boldsymbol{F}_N)$ is a N-particle column vector of forces; similarly, one has torques $\boldsymbol{T}$, stresslets $\boldsymbol{E}$, and higher force multipoles $\boldsymbol{H}^k$. The column vector on the right-hand side consists of the velocity multipoles of $\boldsymbol{v}_i - \boldsymbol{u}_0$, where $\boldsymbol{v} - \boldsymbol{u}_0 = (\boldsymbol{v}_1 - \boldsymbol{u}_0(\boldsymbol{r}_1), \ldots, \boldsymbol{v}_N - \boldsymbol{u}_0(\boldsymbol{r}_N))$ contains the relative translational velocities and $\boldsymbol{\omega} - \boldsymbol{\omega}_0$ the relative angular velocities with the vorticity $\boldsymbol{\omega}_0 = \frac{1}{2}\nabla \times \boldsymbol{u}_0$ of the imposed flow. Since the motion of rigid bodies is completely described by $\boldsymbol{U}$ and $\boldsymbol{\Omega}$, one only has the strain rate tensor $\boldsymbol{g}_0 = \frac{1}{2}(\nabla \otimes \boldsymbol{u}_0 + (\nabla \otimes \boldsymbol{u}_0)^T)$ and higher multipoles of the imposed flow. In case of the Poiseuille flow, the third-rank Cartesian tensor $h_{0\alpha\beta\gamma} = \frac{1}{2}\partial_\beta \partial_\gamma v_{0\alpha}(\boldsymbol{r})$ decomposed in its three irreducible moments $\boldsymbol{h}_0^k$ $(k = 1, 2, 3)$ is also relevant [55]. Finally, the grand resistance matrix contains the $N \times N$ matrices $\boldsymbol{\zeta}^{\mathrm{ab}}$, the elements of which are Cartesian tensors $\boldsymbol{\zeta}_{ij}^{\mathrm{ab}}$.

Typically, one controls forces and torques acting on particles as well as the imposed flow, while translational and rotational particle velocities are unknown. So, a partial inversion of the grand resistance matrix introduces the grand mobility matrix [64, 90],

$$\begin{pmatrix} \boldsymbol{v} - \boldsymbol{u}_0 \\ \boldsymbol{\omega} - \boldsymbol{\omega}_0 \\ -\boldsymbol{E} \\ -\boldsymbol{H}^k \\ \vdots \end{pmatrix} = \begin{pmatrix} \boldsymbol{\mu}^{\mathrm{tt}} & \boldsymbol{\mu}^{\mathrm{tr}} & \boldsymbol{\mu}^{\mathrm{td}} & \boldsymbol{\mu}_k^{\mathrm{th}} & \cdots \\ \boldsymbol{\mu}^{\mathrm{rt}} & \boldsymbol{\mu}^{\mathrm{rr}} & \boldsymbol{\mu}^{\mathrm{rd}} & \boldsymbol{\mu}_k^{\mathrm{rh}} & \cdots \\ \boldsymbol{\mu}^{\mathrm{dt}} & \boldsymbol{\mu}^{\mathrm{dr}} & \boldsymbol{\mu}^{\mathrm{dd}} & \boldsymbol{\mu}_k^{\mathrm{dh}} & \cdots \\ \boldsymbol{\mu}^{\mathrm{ht}} & \boldsymbol{\mu}^{\mathrm{hr}} & \boldsymbol{\mu}^{\mathrm{hd}} & \boldsymbol{\mu}_k^{\mathrm{hh}} & \cdots \\ \vdots & \vdots & \vdots & \vdots & \ddots \end{pmatrix} \begin{pmatrix} \boldsymbol{F} \\ \boldsymbol{T} \\ \boldsymbol{g}_0 \\ \boldsymbol{h}_0^k \\ \vdots \end{pmatrix}, \tag{2.91}$$

with

$$\begin{pmatrix} \boldsymbol{\mu}^{\mathrm{tt}} & \boldsymbol{\mu}^{\mathrm{tr}} \\ \boldsymbol{\mu}^{\mathrm{rt}} & \boldsymbol{\mu}^{\mathrm{rr}} \end{pmatrix} = \begin{pmatrix} \boldsymbol{\zeta}^{\mathrm{tt}} & \boldsymbol{\zeta}^{\mathrm{tr}} \\ \boldsymbol{\zeta}^{\mathrm{rt}} & \boldsymbol{\zeta}^{\mathrm{rr}} \end{pmatrix}^{-1} \tag{2.92}$$

and the remaining mobilities are related to the resistant matrices $\boldsymbol{\zeta}^{\mathrm{ab}}$. We use them to explicitely give the translational and rotational velocities of N spherical colloids subject to external forces, torques, and an imposed Poiseuille flow,

$$\begin{aligned}\boldsymbol{v} &= \boldsymbol{u}_0 + \boldsymbol{\mu}^{\mathrm{tt}}\boldsymbol{F} + \boldsymbol{\mu}^{\mathrm{tr}}\boldsymbol{T} + (\boldsymbol{\mu}^{\mathrm{tt}}\boldsymbol{\zeta}^{\mathrm{td}} + \boldsymbol{\mu}^{\mathrm{tr}}\boldsymbol{\zeta}^{\mathrm{rd}})\boldsymbol{g}_0 \\ &\quad + \sum_{k=1}^{3}(\boldsymbol{\mu}^{\mathrm{tt}}\boldsymbol{\zeta}_k^{\mathrm{th}} + \boldsymbol{\mu}^{\mathrm{tr}}\boldsymbol{\zeta}_k^{\mathrm{rh}})\boldsymbol{h}_0^k, \\ \boldsymbol{\omega} &= \boldsymbol{\omega}_0 + \boldsymbol{\mu}^{\mathrm{rt}}\boldsymbol{F} + \boldsymbol{\mu}^{\mathrm{rr}}\boldsymbol{T} + (\boldsymbol{\mu}^{\mathrm{rt}}\boldsymbol{\zeta}^{\mathrm{td}} + \boldsymbol{\mu}^{\mathrm{rr}}\boldsymbol{\zeta}^{\mathrm{rd}})\boldsymbol{g}_0 \\ &\quad + \sum_{k=1}^{3}(\boldsymbol{\mu}^{\mathrm{rt}}\boldsymbol{\zeta}_k^{\mathrm{th}} + \boldsymbol{\mu}^{\mathrm{rr}}\boldsymbol{\zeta}_k^{\mathrm{rh}})\boldsymbol{h}_0^k.\end{aligned} \tag{2.93}$$

2.5.4 L-multipole approximation and Lubrication correction

In principle, all the elements of the matrices M and Z can be calculated, and therefore the exact Stokes velocities of the spheres can be obtained. However, in practice the infinite-dimensional equations (2.88) and (2.89) need to be approximated to use them in simulations. In the *L-multipole approximation* the matrices $M(ilm\sigma, j'l'm'\sigma')$, $Z(ilm\sigma, j'l'm'\sigma')$ and vectors $c(ilm\sigma)$, $f(ilm\sigma)$ are truncated such that only elements with $l, l' \leq L$ are taken into account [56, 85]. This defines approximations for the involved matrices and vectors

$$\mathrm{c}_L = \mathrm{M}_L\mathrm{f}_L, \quad \mathrm{f}_L = \mathrm{Z}_L\mathrm{c}_L, \tag{2.94}$$

and gives rise to approximated grand resistance and mobility matrices, $\boldsymbol{\zeta}_L$ and $\boldsymbol{\mu}_L$, respectively. As long as the particles are sufficiently far from each other, the L-multipole approximation converges rapidly to the exact mobility matrix with increasing L [56]. However, for nearby particles the convergence is very slow and an alternative method is needed. To account for the lubrication regime, we apply a lubrication correction on the level of the friction matrix [56, 85, 91].

Consider two identical spherical particles in an unbounded fluid at positions $\boldsymbol{r}_1$ and $\boldsymbol{r}_2$, whose distance is very small. The lubrication forces between the spheres are then very strong. For this situation the exact two particle friction matrix $\boldsymbol{\zeta}(1,2)$ can be evaluated using the Jeffrey-Onishi asymptotic formulas supplemented by a series expansion in the inverse particle distance [92, 93]. Here,

$$\boldsymbol{\zeta}(1,2) = \begin{pmatrix} \boldsymbol{\zeta}^{\mathrm{tt}}(1,2) & \boldsymbol{\zeta}^{\mathrm{tr}}(1,2) & \cdots \\ \boldsymbol{\zeta}^{\mathrm{rt}}(1,2) & \boldsymbol{\zeta}^{\mathrm{rr}}(1,2) & \cdots \\ \vdots & \vdots & \ddots \end{pmatrix} \tag{2.95}$$

denotes the exact two particle friction matrix between particle 1 and 2. In order to describe the lubrication regime for a system of N spheres, we introduce the

lubrication correction in a pairwise additive correction [94]. For each element of the N-particle friction matrix $\boldsymbol{\zeta}_L$ we know the exact two-sphere resistance interaction of the particles i and j alone in an unbounded fluid, given by the two-particle friction matrix $\boldsymbol{\zeta}(i,j)$, which we simply add to $\boldsymbol{\zeta}_L$. This defines a N-particle resistance matrix

$$\tilde{\boldsymbol{\zeta}}_L = \boldsymbol{\zeta}_L + \boldsymbol{\zeta}^{\text{pair}}, \tag{2.96}$$

where $\boldsymbol{\zeta}_L^{\text{pair}}$ denotes the superposition of the exact two-particle friction matrix $\boldsymbol{\zeta}(i,j)$. However, part of the two-sphere resistance interactions, the far-field part, has already been included by the friction matrix $\boldsymbol{\zeta}_L$. To avoid double counting of the far-field part, we subtract the two-body interactions already contained in $\boldsymbol{\zeta}_L$. To do so, we subtract from each element of $\tilde{\boldsymbol{\zeta}}_L$ the two-particle friction matrix in unbounded fluid $\boldsymbol{\zeta}_L(i,j)$ which one determines in the L-multipole approximation:

$$\bar{\boldsymbol{\zeta}}_L = \boldsymbol{\zeta}_L + \Delta_L^{\text{pair}}. \tag{2.97}$$

Here, the remainder is given by $\Delta_L^{\text{pair}} = \boldsymbol{\zeta}^{\text{pair}} - \boldsymbol{\zeta}_L^{\text{pair}}$, where $\boldsymbol{\zeta}_L^{\text{pair}}$ denotes the superposition of the approximated two-body friction matrices $\boldsymbol{\zeta}_L(i,j)$. Note that for $L \to \infty$, Δ_L^{pair} becomes zero and $\boldsymbol{\zeta}_L$ converges to the exact friction matrix.

The standard lubrication correction (2.97) affects not only the relative, but also the the collective motions. In particular, it changes the total force and the total torque exerted by a pair of particles on the fluid [91]. As a result, equation (2.97) gives the incorrect large-distance asymptotic behavior for more than two particles, for example, when nearby particles move together and interact with a distant particle [91]. Since the lubrication phenomena arises due to the relative motion of the particles only, one has to project out the forces due to the collective motion. It was shown, that it is sufficient to project out the collective translational motion only [91] such that we have to replace the two-particle friction matrices by

$$\boldsymbol{s}(i,j) = \boldsymbol{q}^{\mathrm{T}}\boldsymbol{\zeta}(i,j)\boldsymbol{q}, \quad \boldsymbol{s}_L(i,j) = \boldsymbol{q}^{\mathrm{T}}\boldsymbol{\zeta}_L(i,j)\boldsymbol{q}, \tag{2.98}$$

where projector $\boldsymbol{q}$ is given by [91]

$$\boldsymbol{q}_{ij}^{\text{tt}} = \frac{1}{2}(-1)^{i+j}\mathbf{1}, \quad \boldsymbol{q}_{ij}^{\text{a=b}} = \delta_{ij}\mathbf{1}, \quad \boldsymbol{q}_{ij}^{\text{a}\neq\text{b}} = \mathbf{0}. \tag{2.99}$$

In full analogy to the friction matrix $\boldsymbol{\zeta}^{\text{pair}}$ composed of the exact two-body friction matrices, we construct a matrix $\boldsymbol{\zeta}^{\text{wall}}$ from the exact one-particle friction matrices in the presence of the lower $\boldsymbol{\zeta}^{\text{low}}(i)$ and upper wall $\boldsymbol{\zeta}^{\text{up}}(i)$. They can be calculated from the Jeffrey-Onishi asymptotic formulas supplemented by a series expansion in the inverse particle distance in the limit that one particle is fixed in space and becomes infinitely large [95]. Finally, the complete L-multipole

approximation for the friction matrix corrected by lubrication forces between two particles as well as between a particle and the bounding walls, is given by

$$\bar{\boldsymbol{\zeta}}_L = \boldsymbol{\zeta}_L + \Delta_L^{\text{pair}} + \Delta_L^{\text{wall}}. \tag{2.100}$$

In analogy to above, we have introduced $\Delta_L^{\text{wall}} = \boldsymbol{\zeta}^{\text{wall}} - \boldsymbol{\zeta}_L^{\text{wall}}$, where $\boldsymbol{\zeta}_L^{\text{wall}}$ is composed from the L-multipole approximation for the one-particle friction matrix in the presence of the lower and the upper wall $\boldsymbol{\zeta}_L^{\text{low}}(i) + \boldsymbol{\zeta}_L^{\text{up}}(i)$. Once $\bar{\boldsymbol{\zeta}}_L$ in equation (2.100) is calculated, one determines the lubrication-corrected L-multipole approximation for the grand mobility matrix $\bar{\boldsymbol{\mu}}_L$ by partial inversion.

2.6 Stokesian dynamics simulations

In the previous sections we derived the equations of motions for N spherical particles suspended in a Newtonian fluid, where in the most general case we considered, the particles are confined between two planar parallel walls and are subjected to external forces, torques and an imposed Poiseuille flow (see section 2.5.3). As we showed, the particle velocities are linearly related to these forces, torques and the imposed flow via the grand mobility matrix (2.91). Since the dependence of the grand mobility matrix on the particle coordinates is highly nonlinear, we describe in this section the integration scheme for the numerical solution of the equations of motion.

2.6.1 Equations of motion

According to equation (2.91), the translational and angular velocities of the spheres are given by

$$\begin{aligned} \boldsymbol{v} &= \boldsymbol{u}_0 + \bar{\boldsymbol{\mu}}_L^{\text{tt}}\boldsymbol{F} + \bar{\boldsymbol{\mu}}_L^{\text{tr}}\boldsymbol{T} + \bar{\boldsymbol{\mu}}_L^{\text{td}}\boldsymbol{g}_0 + \sum_{k=1}^{3} \bar{\boldsymbol{\mu}}_{L,k}^{\text{th}}\boldsymbol{h}_0^k, \\ \boldsymbol{\omega} &= \boldsymbol{\omega}_0 + \bar{\boldsymbol{\mu}}_L^{\text{rt}}\boldsymbol{F} + \bar{\boldsymbol{\mu}}_L^{\text{rr}}\boldsymbol{T} + \bar{\boldsymbol{\mu}}_L^{\text{rd}}\boldsymbol{g}_0 + \sum_{k=1}^{3} \bar{\boldsymbol{\mu}}_{L,k}^{\text{rh}}\boldsymbol{h}_0^k. \end{aligned} \tag{2.101}$$

Note that, in the case of point-particles, the rotational motion is neglected and equation (2.101) reduces to (2.76). This evolution equation that we use in the Stokesian-dynamics simulations can then be written in compact differential form as

$$\mathrm{d}\mathbf{x} = \mathbf{v}\mathrm{d}t, \quad \mathbf{v} = \mathbf{u}_0(\boldsymbol{x}) + \mathbf{m}(\boldsymbol{x})\mathbf{h}(\boldsymbol{x}) + \boldsymbol{\mu}(\boldsymbol{x})\mathbf{F}(\boldsymbol{x}). \tag{2.102}$$

Here, we have introduced the $6N$-dimensional differential $\mathrm{d}\mathbf{x} = (\mathrm{d}\boldsymbol{x}, \mathrm{d}\boldsymbol{\phi}) = (\mathrm{d}\boldsymbol{r}_1, \ldots, \mathrm{d}\boldsymbol{r}_N, \mathrm{d}\boldsymbol{\phi}_1, \ldots, \mathrm{d}\boldsymbol{\phi}_N)$, where the vector $\mathrm{d}\boldsymbol{\phi}_i$ defines an infinitesimal rotation of particle i, the generalized N-particle velocities $\mathbf{v} = (\boldsymbol{v}, \boldsymbol{\omega})$ and $\mathbf{u}_0 = (\boldsymbol{u}_0, \boldsymbol{\omega}_0)$, the generalized forces $\mathbf{F} = (\boldsymbol{F}, \boldsymbol{T})$, the higher order velocity multipole moments $\mathbf{h} = (\boldsymbol{g}_0, \boldsymbol{h}_0^1, \boldsymbol{h}_0^2, \boldsymbol{h}_0^3)$, the mobility matrix

$$\boldsymbol{\mu} = \begin{pmatrix} \bar{\boldsymbol{\mu}}_L^{\mathrm{tt}} & \bar{\boldsymbol{\mu}}_L^{\mathrm{tr}} \\ \bar{\boldsymbol{\mu}}_L^{\mathrm{rt}} & \bar{\boldsymbol{\mu}}_L^{\mathrm{rr}} \end{pmatrix}, \tag{2.103}$$

and the matrix $\mathbf{m}$ containing the other elements of the grand mobility matrix

$$\mathbf{m} = \begin{pmatrix} \bar{\boldsymbol{\mu}}_L^{\mathrm{td}} & \bar{\boldsymbol{\mu}}_{L,1}^{\mathrm{th}} & \bar{\boldsymbol{\mu}}_{L,2}^{\mathrm{th}} & \bar{\boldsymbol{\mu}}_{L,3}^{\mathrm{th}} \\ \bar{\boldsymbol{\mu}}_L^{\mathrm{rd}} & \bar{\boldsymbol{\mu}}_{L,1}^{\mathrm{rh}} & \bar{\boldsymbol{\mu}}_{L,2}^{\mathrm{rh}} & \bar{\boldsymbol{\mu}}_{L,3}^{\mathrm{rh}} \end{pmatrix}. \tag{2.104}$$

As we already mentioned in the introduction to this section, the matrices $\boldsymbol{m}$ and $\boldsymbol{\mu}$ are highly nonlinear in the particle coordinates. Therefore, we use a higher-order integration scheme for the numerical solution of this equation, which is presented in the following.

2.6.2 Numerical integration scheme

The simplest method to obtain an numerical solution of equation (2.102) is the well known *Euler method* [96]. Here, the equation of motion is discretized with respect to time t

$$\Delta\mathbf{x}_t = \mathbf{v}(\boldsymbol{x}_t)\Delta t, \tag{2.105}$$

and then the configuration update $\mathbf{x}_{t+\Delta t} = \mathbf{x}_t + \Delta\mathbf{x}_t$ is calculated. However, this procedure is not recommended for practical use, because it is less accurate in comparison to other methods and it is not very stable [97]. Therefore, one should use integration schemes of higher order in the time step Δt to avoid the accumulation of numerical errors. Higher order algorithm typically combine the informations of several Euler-steps such that they match the Taylor expansion of this function up to the order of Δt^n. By far the most often used integration scheme is the so called *fourth-order Runge-Kutta algorithm* (also referred to as the *classical Runge-Kutta method*) [98, 99]. This algorithm consists of the following intermediate Euler steps

$$\begin{aligned} \Delta\mathbf{x}_1 &= \mathbf{v}(\boldsymbol{x}_t), \\ \Delta\mathbf{x}_2 &= \mathbf{v}(\boldsymbol{x}_t + \frac{1}{2}\boldsymbol{x}_1), \\ \Delta\mathbf{x}_3 &= \mathbf{v}(\boldsymbol{x}_t + \frac{1}{2}\boldsymbol{x}_2), \\ \Delta\mathbf{x}_4 &= \mathbf{v}(\boldsymbol{x}_t + \boldsymbol{x}_3). \end{aligned} \tag{2.106}$$

Finally, the new configuration $\mathbf{x}_{t+\Delta t} = \mathbf{x}_t + \Delta\mathbf{x}_t$ is obtained from the combined step [99]

$$\Delta\mathbf{x}_t = \frac{1}{6}(\Delta\mathbf{x}_1 + 2\Delta\mathbf{x}_2 + 2\Delta\mathbf{x}_3 + \Delta\mathbf{x}_4)\Delta t. \tag{2.107}$$

3 Brownian motion

«Je planmäßiger die Menschen vorgehen, desto wirksamer vermag sie der Zufall zu treffen.»

Friedrich Dürrenmatt

In the previous chapter we derived the equations of motion for N spherical objects suspended in a Newtonian fluid, where the hydrodynamic interactions are completely described by the mobility matrix. The components of this matrix are highly nonlinear in the particle coordinates and can be calculated for different geometries (compare unbounded fluid [see section 2.4] with bounded fluid [see section 2.5]). Next to this deterministic motion (*Stokesian dynamics*) the particles also undergo erratic movements, the well known *Brownian motion*. The origin of this motion arise due to collisions with the surrounding fluid molecules [24, 100].

On the molecular level the dynamics of the collisions are completely deterministic. However, even if we would know all initial conditions, it is impossible to predict the future of the system, since the computational effort is exorbitant (around 10^{22} water molecules per cm^3). Moreover, chaos theory shows that even if we had all informations on the interactions and thus the complete equations of motions, any slight error in the initial conditions would be magnified exponentially [101]. So, in fact, there is practically no predictability.

Instead of including all degrees of freedom of the water molecules, we describe the influence of the collision between them and the suspended objects by a statistical theory. In this description the fluid is first considered to be continuous, which corresponds to averaging over a huge number of collisions of the suspended particles with the fluid molecules. This averaging leads to the *deterministic* hydrodynamic forces and torques acting on the suspended particles as described in detail in the previous chapter. Secondly, the solvent can be treated as a source of noise that causes a random motion due to the continuous collisions with the suspended particles.

This picture can be formulated by two different but equivalent concepts of theoretical mechanics. In the first approach the deterministic equations of motion are supplemented by random forces and torques acting on the particles. This results in differential stochastic equation (*SDE*), which is referred to as the *Langevin equation*. In the second approach, one is not interested in the single particle trajectories but instead, in ensemble averages. These can be calculated by the probability distribution of the system in phase space, where the time evolution is governed by a diffusion-type differential equation, the so called *Smoluchowski equation*.

3.1 The Langevin equation

As discussed in section 2.6.1, the equations of motion for N spherical particles suspended in a solvent can be expressed in the following compact equation

$$\mathbf{v} = \mathbf{u}_0(\boldsymbol{x}) + \mathbf{m}(\boldsymbol{x})\mathbf{h}(\boldsymbol{x}) + \boldsymbol{\mu}(\boldsymbol{x})\mathbf{F}(\boldsymbol{x}), \tag{3.1}$$

where $\mathbf{v} = (\boldsymbol{v}, \boldsymbol{\omega})$ and $\mathbf{u}_0 = (\boldsymbol{u}_0, \boldsymbol{\omega}_0)$ are the generalized N-particle velocities, $\mathbf{F} = (\boldsymbol{F}, \boldsymbol{T})$ the generalized forces, $\mathbf{h} = (\boldsymbol{g}_0, \boldsymbol{h}_0^1, \boldsymbol{h}_0^2, \boldsymbol{h}_0^3)$ the higher order velocity multipole moments, $\boldsymbol{\mu}$ the mobility matrix and the matrix $\mathbf{m}$ contains the other elements of the grand mobility matrix. Note that in the absence of the imposed flow $\boldsymbol{u}_0$, the first two terms on the right hand side of this equation vanish and the components of the mobility matrix $\boldsymbol{\mu}$ depend on the chosen system geometry (see section 2.4 and section 2.5). In addition to this deterministic motion, every particle experiences a rapidly fluctuating random force and torque $\boldsymbol{\Gamma}(t)$, which arises from collisions with the surrounding fluid particles [24, 100]. These forces fluctuate on a timescale of about 10^{-14}s, which is the typical relaxation time of the surrounding fluid. Considering these stochastic forces the equation of motion reads

$$\mathbf{v} = \mathbf{u}_0(\boldsymbol{x}) + \mathbf{m}(\boldsymbol{x})\mathbf{h}(\boldsymbol{x}) + \boldsymbol{\mu}(\boldsymbol{x})(\mathbf{F}(\boldsymbol{x}) + \boldsymbol{\Gamma}(t)). \tag{3.2}$$

This equation is a first order stochastic differential equation, the so called Langevin equation. In 1908, Paul Langevin was able to describe the diffusional process of the Brownian motion with the help of such an equation [102]. In general the Langevin equation reads

$$\frac{\mathrm{d}}{\mathrm{d}t}x(t) = h(x(t), t) + g\Gamma(t), \tag{3.3}$$

where the last term on the right hand side is the so called noise term. If the quantity g is constant then the last term is referred to as *additive noise*. If $g = g(x(t))$ is a function of the variable $x(t)$ then the last term is referred to as *multiplicative noise*, which leads to the *Ito-Stratonovich dilemma* (see section 3.1.2).

Since the stochastic force $\boldsymbol{\Gamma}(t)$ is a random number, the rules of ordinary differential equations can no longer be applied to equation 3.3. Therefore this equation is meaningless in a strict mathematical sense. With the help of the stochastic calculus of *Wiener process* we will be able to treat the trajectories of this random motion analytically. But before, we want to discuss the properties of the random force $\boldsymbol{\Gamma}(t)$.

3.1.1 Fluctuation-dissipation theorem

In order to treat equation (3.2) analytically, we need more informations about the random force $\mathbf{\Gamma}(t)$. For simplicity, we consider one particle in one dimension with mass m and friction coefficient ζ

$$m\dot{v} + \zeta v = \Gamma(t). \tag{3.4}$$

Since the systematic interactions with the solvent molecules are made explicit, all interactions which will not vanish in the ensemble average belong to the deterministic part. Therefore, the ensemble average of the fluctuating force is zero

$$\langle \Gamma(t) \rangle = 0. \tag{3.5}$$

Here, the brackets $\langle \dots \rangle$ denote the ensemble average. As mentioned above, the random forces fluctuate on a timescale of about 10^{-14}s, whereas the relaxation time of the suspended particle is in the order of a few nanoseconds. Due to a large separation in the time scales, it is sufficient to assume a delta correlated random force in time [24]

$$\langle \Gamma(t)\Gamma(t') \rangle = q\delta(t - t'). \tag{3.6}$$

Here, δ denotes the delta distribution and q is a constant which is referred to as *fluctuation strength* and has to be determined. In equilibrium the equipartition theorem must hold, which implies (in one dimension)

$$\frac{1}{2}m \left\langle v^2 \right\rangle = \frac{1}{2}k_{\mathrm{B}}T, \tag{3.7}$$

where k_{B} is the *Boltzman constant* and T the absolute temperature. Together with equations (3.4),(3.5) and (3.6) we find [24]

$$\begin{aligned} \frac{1}{2}m \left\langle v^2 \right\rangle &= \frac{1}{2}mv^2(0)e^{-\frac{2t}{\tau_{\mathrm{r}}}} + \frac{1}{2m}\int_0^t \int_0^t e^{-\frac{(2t-t'-t'')}{\tau_{\mathrm{r}}}} \langle \Gamma(t')\Gamma(t'') \rangle \, \mathrm{d}t'\mathrm{d}t'' \\ &\overset{t \gg \tau_{\mathrm{r}}}{=} \frac{1}{4}\frac{\tau_{\mathrm{r}}}{m}q, \end{aligned} \tag{3.8}$$

where $\tau_{\mathrm{r}} = m/\zeta$ is the relaxation time of the suspended particle. If we compare this result with the equipartition theorem (3.7), we find $q = 2k_{\mathrm{B}}T\zeta$. This leads to

$$\langle \Gamma(t)\Gamma(t') \rangle = 2k_{\mathrm{B}}T\zeta\delta(t - t'). \tag{3.9}$$

This relation is referred to as the *fluctuation dissipation theorem*. It connects the fluctuation strength with the friction coefficient, which determines the dissipation

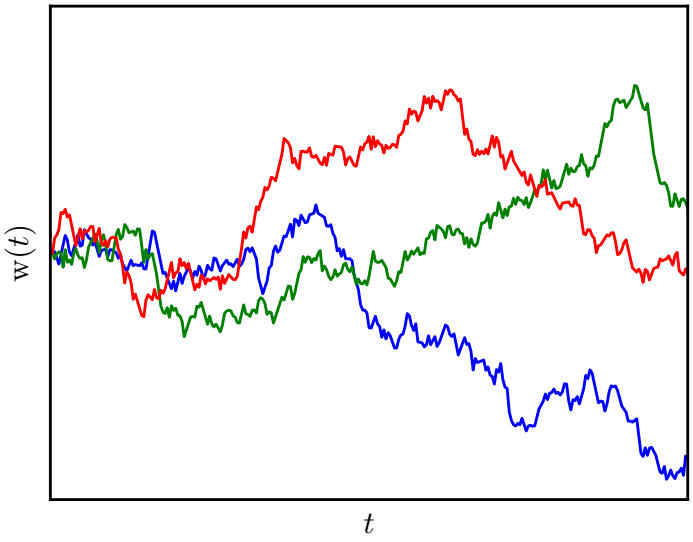

Figure 3.1: Three simulated sample paths of the one-dimensional Wiener process, illustrating their great variability.

into heat. In three dimensions and for N particles equations (3.5) and (3.9) read [103, 104]

$$\begin{aligned} \langle \mathbf{\Gamma}(t) \rangle &= \mathbf{0} \\ \langle \mathbf{\Gamma}(t) \otimes \mathbf{\Gamma}(t') \rangle &= 2k_{\mathrm{B}}T\boldsymbol{\zeta}\delta(t-t'), \end{aligned} \tag{3.10}$$

where $\boldsymbol{\zeta} = \boldsymbol{\mu}^{-1}$ is the $6N \times 6N$ friction matrix (2.92).

3.1.2 The Wiener process

In the previous section we discussed the properties of the random force $\mathbf{\Gamma}(t)$. In this section we want to evaluate the Langevin equation (3.2). Therefore we first rewrite this equation as

$$\mathsf{v} = \mathsf{f}(\boldsymbol{x}) + \boldsymbol{\mu}(\boldsymbol{x})\mathbf{\Gamma}(t), \tag{3.11}$$

where $\mathsf{f}(\boldsymbol{x}) = \mathsf{u}_0(\boldsymbol{x}) + \mathsf{m}(\boldsymbol{x})\mathsf{h}(\boldsymbol{x}) + \boldsymbol{\mu}(\boldsymbol{x})\mathsf{F}(\boldsymbol{x}))$. This equation can be formally solved by integration, which leads to

$$\mathsf{x}(t) - \mathsf{x}(0) = \int_0^t \mathsf{f}(\boldsymbol{x}(t'))\ \mathrm{d}t' + \int_0^t \boldsymbol{\mu}(\boldsymbol{x}(t'))\mathbf{\Gamma}(t')\ \mathrm{d}t'. \tag{3.12}$$

The second integral on the right hand side of equation (3.12) cannot be solved in the sense of a Riemann sum. In order to analyze this term we need the stochastic calculus of Wiener processes [105, 106, 107, 108]. The integral equation for the increment $\Delta\mathbf{x}(t) = \mathbf{x}(t+\Delta t) - \mathbf{x}(t)$ is given by

$$\Delta\mathbf{x}(t) = \int_t^{t+\Delta t} \mathbf{f}(\boldsymbol{x}(t'))\ \mathrm{d}t' + \int_t^{t+\Delta t} \boldsymbol{\mu}(\boldsymbol{x}(t'))\mathrm{d}\mathbf{w}(t'), \tag{3.13}$$

where $\mathrm{d}\mathbf{w}(t) = \mathbf{w}(t+\mathrm{d}t) - \mathbf{w}(t)$ is the increment of a Wiener process

$$\mathbf{w}(t) = \int_0^t \boldsymbol{\Gamma}(t')\ \mathrm{d}t', \tag{3.14}$$

which is a Gaussian variable with zero mean $\langle \mathbf{w}(t) \rangle = 0$ and time correlation

$$\langle \mathbf{w}(t) \otimes \mathbf{w}(t') \rangle = 2k_{\mathrm{B}}T\boldsymbol{\zeta}\min(t,t'). \tag{3.15}$$

The increments $\mathrm{d}\mathbf{w}(t)$ are then Gaussian variables too, with the following properties

$$\begin{aligned} \langle \mathrm{d}\mathbf{w}(t) \rangle &= 0, \\ \langle \mathrm{d}\mathbf{w}(t) \otimes \mathrm{d}\mathbf{w}(t) \rangle &= 2k_{\mathrm{B}}T\boldsymbol{\zeta}\mathrm{d}t, \end{aligned} \tag{3.16}$$

which one can easily validate by the definition (3.14) and equation (3.10). The increments at different times are independent of each other. Also, one easily sees from equation (3.16) that $\mathrm{d}\mathbf{w}(t)$ is proportional to $\sqrt{\mathrm{d}t}$.

The second integral on the right hand side of equation (3.13) has the form of a *Stieltjes-integral*. This integral is defined on the interval $[t, t+\Delta t]$ subdivided into the equidistant parts $t = t_0 < t_1 <, \cdots <, t_n = t + \Delta t$ as the limes of the partial sums [109]

$$\int_t^{t+\Delta t} \boldsymbol{\mu}(\boldsymbol{x}(t'))\mathrm{d}\mathbf{w}(t') = \underset{n\to\infty}{\text{ms-lim}} \sum_{i=1}^{n} \boldsymbol{\mu}(\boldsymbol{x}(\tau_i))[\mathbf{w}(t_i) - \mathbf{w}(t_{i-1})], \tag{3.17}$$

where $\tau_i \in [t_{i-1}, t_i)$ and ms-lim denotes the *mean-square limit*[1]. It is quite easy to show, that in contrast to ordinary Riemann integrals this integral (3.17) depends on the particular choice of the intermediate point τ_i [107, 110], which we write as

$$\tau_i = (1-\alpha)t_{i-1} + \alpha t_i. \tag{3.18}$$

[1]Let X_n be a sequence of random variables and let X be a random variable. The sequence X_n is said to converge to X in mean-square (ms-$\lim_{n\to\infty} X_n = X$) if $\lim_{n\to\infty} \left\langle (X_n - X)^2 \right\rangle = 0$.

Here, α can take any value between zero and one. There are mainly two different types of interpretations of the integral (3.17):

$$\begin{aligned} \alpha &= 0 \quad \text{Itô interpretation,} \\ \alpha &= \frac{1}{2} \quad \text{Stratonovich interpretation.} \end{aligned} \tag{3.19}$$

The difference between these interpretations can be clearly seen: Itô evaluates $\boldsymbol{\mu}(\boldsymbol{x}(\tau_i))$ at the beginning of the interval, whereas Stratonovich evaluates this term at the mid-point. If we consider Δt to be very small, $\Delta t \to \mathrm{d}t$, we can write equation (3.13) as the following *Itô stochastic differential equation*

$$\mathrm{d}\mathbf{x} = \mathbf{f}\mathrm{d}t + \boldsymbol{\mu}\mathrm{d}\mathbf{w}, \tag{3.20}$$

where $\boldsymbol{\mu}(\boldsymbol{x}(t))$ is evaluated at the beginning of the interval $[t, t+\mathrm{d}t]$. Respectively, we can write down the following *Stratonovich stochastic differential equation*

$$\mathrm{d}\mathbf{x} = \mathbf{f}\mathrm{d}t + \boldsymbol{\mu} \circ \mathrm{d}\mathbf{w}, \tag{3.21}$$

where the symbol "$\circ$" denotes that $\boldsymbol{\mu}(\boldsymbol{x}(t+\frac{1}{2}\mathrm{d}t))$ is evaluated at the intermediate point $t + \frac{1}{2}\mathrm{d}t$. Now, the question arises, which one of these two interpretations one has to choose. In principle, the answer depends on the chosen system. For physically systems one usually tends to choose the Stratonovich interpretation. This is the natural choice for an interpretation which assumes $\boldsymbol{\Gamma}$ is real noise in equation (3.10) (not a white noise) with finite correlation time, which is then allowed to become infinitesimally small after calculating measurable quantities [107]. Whereas in a system which is intrinsically discontinuous, e.g., in the stock exchange or in the evolution of biological populations the Itô interpretation is usually applied [109]. Another advantage of the Stratonovich interpretation is that it allows the use of the ordinary rules of differential calculus, whereas Itôs formula shows that rule of changing variables is not given by ordinary calculus [107, 110]. On the other hand, Stratonovich stochastic differential equations are usually translated to equivalent Itô stochastic differential equations for mathematical analysis of their properties. To do so, we expand $\boldsymbol{\mu}(\boldsymbol{x})$ in terms of t in equation (3.21)

$$\mathrm{d}\mathbf{x} = \mathbf{f}\mathrm{d}t + \boldsymbol{\mu}(\boldsymbol{x} + \frac{1}{2}\mathrm{d}\boldsymbol{x} + \dots)\mathrm{d}\mathbf{w}, \tag{3.22}$$

with $\boldsymbol{x}(t+\frac{1}{2}\mathrm{d}t) = \boldsymbol{x}(t) + \frac{1}{2}\mathrm{d}\boldsymbol{x}(t) + \dots$. Considering only terms up to the order of $\mathrm{d}t$ yields[1] [111, 112]

$$\begin{aligned} \mathrm{d}\mathbf{x} &= \mathbf{f}\mathrm{d}t + \left[\boldsymbol{\mu} + \frac{1}{2}(\mathrm{d}\boldsymbol{x}\cdot\nabla)\boldsymbol{\mu} + \mathfrak{O}(\mathrm{d}t)\right]\mathrm{d}\mathbf{w} \\ &= \mathbf{f}\mathrm{d}t + \frac{1}{2}\left([(\mathrm{d}\mathbf{w}\otimes\mathrm{d}\mathbf{w})\boldsymbol{\mu}]\,\nabla\right)\boldsymbol{\mu} + \boldsymbol{\mu}\mathrm{d}\mathbf{w} + \mathfrak{O}(\mathrm{d}t)^{\frac{3}{2}}. \end{aligned} \tag{3.23}$$

[1] Note that here $\nabla = (\nabla_1, \dots, \nabla_N)$ denotes the generalized $3N$-dimensional Nabla operator.

Note that d$\mathbf{w}$ is proportional to $\sqrt{\mathrm{t}}$ (3.16) and that d$\boldsymbol{x}$ also consists of a term proportional to d$\mathbf{w}$ (3.22). To eliminate the stochastic variable d$\mathbf{w}$ we take the mean of equation (3.23). Together with the properties of the Wiener increment (3.16), we obtain

$$\begin{aligned} \langle \mathrm{d}\mathbf{x} \rangle &= [\mathbf{f} + k_\mathrm{B}T\,(\boldsymbol{\mu}\boldsymbol{\zeta})\,\nabla\boldsymbol{\mu}]\,\mathrm{d}t \\ &= [\mathbf{f} + \nabla\boldsymbol{D}]\,\mathrm{d}t, \\ \langle \mathrm{d}\mathbf{x} \otimes \mathrm{d}\mathbf{x} \rangle &= 2k_\mathrm{B}T\,(\boldsymbol{\mu}\boldsymbol{\zeta})\,\boldsymbol{\mu} \\ &= 2\boldsymbol{D}\mathrm{d}t. \end{aligned} \tag{3.24}$$

Here, we used equation (2.92) and the generalized *Einstein relation* $\boldsymbol{D} = k_\mathrm{B}T\boldsymbol{\mu}$, where $\boldsymbol{D}$ is the diffusivity [113]. So, finally we can write Stratonovichs interpretation as an equivalent Ito stochastic differential equation [107, 110]

$$\mathrm{d}\mathbf{x} = [\mathbf{f} + \nabla\boldsymbol{D}]\,\mathrm{d}t + \boldsymbol{\mu}\mathrm{d}\mathbf{w}. \tag{3.25}$$

The additional term $\nabla\boldsymbol{D}$ in equation (3.25) compared to equation (3.20) is referred to as *spurious drift* [105], which can be interpreted as an additional drift velocity. Since this term is proportional to the temperature T, this effect is *noise induced*.

3.2 The Smoluchowski equation

Instead of calculating the trajectories of a stochastic system explicitly, one can also describe the stochastic dynamics with the help of a probability density $\psi(\boldsymbol{x}, t)$, where $\psi(\boldsymbol{x}, t)\mathrm{d}\boldsymbol{x}$ is the probability to find the system in $[\boldsymbol{x}, \boldsymbol{x}+\mathrm{d}\boldsymbol{x}]$ at time t. The evolution of this probability density is governed by the so called *Fokker-Planck equation*. It can be shown that one can assign a unique Fokker-Planck equation to each Langevin equation [110]. Therefore, different Langevin equations that possess the same Fokker-Planck equation are stochastically equivalent. The Fokker-Planck equation can be obtained by the *Kramer-Moayl expansion* [110]

$$\frac{\partial}{\partial t}\psi(\boldsymbol{x}, t) = \sum_{n=1}^{\infty} \sum_{i_1,\ldots,i_n}^{3N} (-1)^n \frac{\partial^n}{\partial x_{i_1} \cdots \partial x_{i_n}} \mathrm{D}^{(n)}_{i_1 \ldots i_n}, \tag{3.26}$$

where the *Kramer-Moyal coefficients* $\mathbf{D}^{(n)}$ are given by the following moments [110]

$$\mathbf{D}^{(n)} = \frac{1}{n!} \lim_{\tau \to 0} \frac{1}{\tau} \left\langle [\boldsymbol{x}(t+\tau) - \boldsymbol{x}(t)]^{\otimes n} \right\rangle. \tag{3.27}$$

Here, the subscript $\otimes n$ denotes the n-th dyadic product. In the over-damped regime, we can read off the first two Kramer-Moyal coefficients directly from equations (3.24) and (3.25) together with the properties of the Wiener increment (3.16):

$$\begin{aligned} \mathbf{D}^{(1)} &= \mathbf{f} + \nabla \boldsymbol{D}, \\ \mathbf{D}^{(2)} &= k_{\mathrm{B}} T \boldsymbol{M} = \boldsymbol{D}. \end{aligned} \tag{3.28}$$

It can be shown that for the Langevin equations with Gaussian white noise (3.11), higher Kramer-Moyal coefficients are identical zero [110]

$$\mathbf{D}^{(n)} = \mathbf{0}, \quad n > 2. \tag{3.29}$$

Therefore, together with these coefficients (3.28) and (3.29), we obtain the following Fokker-Planck equation

$$\frac{\partial}{\partial t}\psi(\boldsymbol{x}, t) = -\nabla \cdot \left[\mathbf{f}\psi - \boldsymbol{D}\nabla\psi\right]. \tag{3.30}$$

Note, in the over-damped limit, the Fokker-Planck equation is applied to particle position distributions $\psi(\boldsymbol{x}, t)$, which is better known as the *Smoluchowski equation* [110]. We can write down the Smoluchowski equation (3.30) in the form of a continuity equation

$$\begin{aligned} \frac{\partial}{\partial t}\psi &= -\nabla \cdot \boldsymbol{j}, \\ &= -\nabla \cdot (\boldsymbol{j}^{\mathrm{drift}} + \boldsymbol{j}^{\mathrm{diff}}), \end{aligned} \tag{3.31}$$

where $\boldsymbol{j}$ is probability density current, which consists of a deterministic part $\boldsymbol{j}^{\mathrm{det}} = \mathbf{f}\psi$ and a diffusional part $\boldsymbol{j}^{\mathrm{diff}} = -\boldsymbol{D}\nabla\psi$.

3.3 Brownian dynamics simulation

In section 3.1.2, we derived the stochastic differential equations (3.20) and (3.21). With their help we are able to describe the fluctuating forces due to collisions between the molecules and the suspended particles mathematically. In this section we will describe how we solve this kind of equations numerically using the method of *Brownian dynamics simulation*.

3.3.1 Numerical integration scheme

The simplest discretization scheme of the Langevin equation in the Itô form (3.25) is the Euler step (see also section 2.6.2)

$$\Delta \mathbf{x}_t = [\mathbf{f}(\boldsymbol{x}_t) + \nabla \boldsymbol{D}(\boldsymbol{x}_t)]\,\Delta t + \boldsymbol{H}(\boldsymbol{x}_t)\Delta \bar{\mathbf{w}}_t. \tag{3.32}$$

Here, we have introduced the matrix $\boldsymbol{H}(\boldsymbol{x})$, which is the solution of the following relation:

$$2\boldsymbol{D}(\boldsymbol{x}) = \boldsymbol{H}(\boldsymbol{x})\boldsymbol{H}^{\mathrm{T}}(\boldsymbol{x}). \tag{3.33}$$

This relation indicates, to say it with sloppy words, that the matrix $\boldsymbol{H}(\boldsymbol{x})$ is somehow the square root of $2\boldsymbol{D}(\boldsymbol{x})$. We can determine this quantity by *Cholesky decomposition*, which we will describe in section 3.3.2. The first two moments of the the Wiener increment $\Delta\bar{\mathbf{w}}$ are given by

$$\begin{aligned} \langle \Delta \bar{\mathbf{w}}_t \rangle &= 0, \\ \langle \Delta \bar{\mathbf{w}}_t \otimes \Delta \bar{\mathbf{w}}_t \rangle &= \mathbf{1}\Delta t, \end{aligned} \tag{3.34}$$

which are independent of each other at different times. To obtain the correct Wiener increments, we generate a new set of $6N$ independent random numbers n_i at each time step, obeying the Gaussian distribution

$$p(n) = \frac{1}{2\pi} e^{-n^2/2} \tag{3.35}$$

with zero mean and unit variance and multiply these numbers with $\sqrt{\Delta t}$

$$\Delta \bar{\boldsymbol{w}}_t = \begin{pmatrix} n_1 \\ \vdots \\ n_{6N} \end{pmatrix} \sqrt{\Delta t}. \tag{3.36}$$

The algorithm we use to calculate these Gaussian random numbers is presented in section 3.3.3. The representation (3.32) of stochastic differential equation is equivalent to equation (3.25) for $\Delta t \to \mathrm{d}t$, which one can easily verify by calculating the first two moments:

$$\begin{aligned} \langle \mathrm{d}\mathbf{x} \rangle &= [\mathbf{f} + \nabla \boldsymbol{D}]\,\mathrm{d}t + \boldsymbol{H}\,\langle \mathrm{d}\bar{\mathbf{w}} \rangle \\ &\overset{(3.34)}{=} [\mathbf{f} + \nabla \boldsymbol{D}]\,\mathrm{d}t, \\ \langle \mathrm{d}\mathbf{x} \otimes \mathrm{d}\mathbf{x} \rangle &= \langle (\boldsymbol{H}\mathrm{d}\bar{\mathbf{w}}) \otimes (\boldsymbol{H}\mathrm{d}\bar{\mathbf{w}}) \rangle \overset{(3.34)}{=} \boldsymbol{H}\boldsymbol{H}^{\mathrm{T}}\mathrm{d}t \\ &\overset{(3.33)}{=} 2\boldsymbol{D}\mathrm{d}t. \end{aligned} \tag{3.37}$$

After performing the Euler step (3.32), we can calculate the configurational update $\mathbf{x}_{t+\Delta t} = \mathbf{x}_t + \Delta\mathbf{x}_t$. The main problem of this direct implementation is the calculation of the divergence of the diffusion tensor $\nabla \boldsymbol{D}$ at each time step, which requires enormous computational time. To avoid the explicit calculation of this term, we write down the discretized Itô stochastic differential equation (3.32) in the corresponding equivalent Stratonovich form (see section 3.1.2)

$$\Delta\mathbf{x}_t = \mathbf{f}(\boldsymbol{x}_t)\Delta t + \boldsymbol{H}(\boldsymbol{x}_t) \circ \Delta\bar{\mathbf{w}}_t. \tag{3.38}$$

The advantage of this form is that the explicit calculation of the spurious drift is not necessary. On the other hand, the quantities in equation (3.38) are evaluated at the intermediate time step $t + \frac{1}{2}\Delta t$. Unfortunately, this requires the knowledge of the configurational update $\boldsymbol{x}_t + \frac{1}{2}\Delta\boldsymbol{x}_t$, which is not available. To overcome this problem, we use a *predictor-corrector scheme* [114, 115, 116, 117]. First, we perform an Euler step without spurious drift

$$\Delta\bar{\mathbf{x}}_t = \mathbf{f}(\boldsymbol{x}_t)\Delta t + \boldsymbol{H}(\boldsymbol{x}_t)\Delta\bar{\mathbf{w}}_t. \tag{3.39}$$

Then we use the intermediate configuration $\mathbf{x}_t + \Delta\bar{\mathbf{x}}$ to calculate the corrector step

$$\begin{aligned} \Delta\boldsymbol{x}_t &= \frac{1}{2}\left[\mathbf{f}(\boldsymbol{x}_t) + \mathbf{f}(\boldsymbol{x}_t + \Delta\bar{\boldsymbol{x}}_t)\right]\Delta t \\ &\quad + \frac{1}{2}\left[\mathbf{1} + \boldsymbol{D}(\boldsymbol{x}_t + \Delta\bar{\boldsymbol{x}}_t)\boldsymbol{D}^{-1}(\boldsymbol{x}_t)\right]\boldsymbol{H}(\boldsymbol{x}_t)\Delta\bar{\mathbf{w}}_t. \end{aligned} \tag{3.40}$$

Now, we can compute the final configuration $\mathbf{x}_{t+\Delta t} = \mathbf{x}_t + \Delta\mathbf{x}_t$. Note that the expression $\boldsymbol{H}(\boldsymbol{x}_t)\Delta\bar{\mathbf{w}}_t$ in the corrector step (3.40) is the same as in the predictor step (3.39), thus computation time can be saved by calculating this term only once. Note that the above scheme is actually correct to order Δt^2 for a constant diffusion matrix. There are also higher order integration schemes of Runge-Kutta type available for stochastic differential equations [118]. However, these methods require the explicit calculation of the spurious drift $\nabla \boldsymbol{D}$.

3.3.2 The Cholesky decomposition

In section 3.3.1, we have introduced the matrix $\boldsymbol{H}$, which is the solution of $2\boldsymbol{D} = \boldsymbol{H}\boldsymbol{H}^{\mathrm{T}}$. In general every symmetric and positive defined matrix $\boldsymbol{A}$ (as the diffusion matrix $\boldsymbol{D}$ is) can be decomposed in

$$\boldsymbol{A} = \boldsymbol{L}\boldsymbol{L}^{\mathrm{T}}, \tag{3.41}$$

where $\boldsymbol{L}$ is a lower triangular matrix. The single elements of this matrix can be determined recursively by [119, 120]

$$\begin{aligned} L_{ii} &= \left(a_{ii} - \sum_{k=1}^{i-1} L_{ik}^2 \right)^{\frac{1}{2}}, \\ L_{ij} &= \frac{1}{L_{jj}} \left(A_{ij} - \sum_{k=1}^{j-1} L_{ik} L_{jk} \right) \quad \text{for} \quad i > j, \end{aligned} \tag{3.42}$$

which is called Cholesky decomposition.

3.3.3 Gaussian random numbers: the Box-Muller transform

In this section we will describe how we compute Gaussian random numbers. Consider a random number x with a given probability distribution $p(x)$. The distribution for a transformed variable $y = y(x)$ is then easily given by

$$p(y) = p(x) \left| \frac{\mathrm{d}x}{\mathrm{d}y} \right|. \tag{3.43}$$

More generally, let us consider the random numbers $x_1, x_2, \dots$ with the joint probability distribution $p(x_1, x_2, \dots)$. If each of the transformed variables $y_1, y_2, \dots$ is a function of all the x_i , then the joint probability distribution of the y_i is given by [97, 114]

$$p(y_1, y_2, \dots) = p(x_1, x_2, \dots) \left| \frac{\partial(x_1, x_2, \dots)}{\partial(y_1, y_2, \dots)} \right|, \tag{3.44}$$

where $|\partial(x_1, x_2, \dots)/\partial(y_1, y_2, \dots)|$ denotes the Jacobian determinant of x_i with respect to y_i. Let us now consider two independent random numbers x_1 and x_2, which are uniformly distributed in the interval $[0, 1]$. The transformation [121]

$$\begin{aligned} y_1 &= \sqrt{-2 \ln x_1} \cos 2\pi x_2, \\ y_2 &= \sqrt{-2 \ln x_1} \sin 2\pi x_2, \end{aligned} \tag{3.45}$$

with the inversion

$$\begin{aligned} x_1 &= \exp\left(-\frac{1}{2}(y_1^2 + y_2^2) \right), \\ x_2 &= \frac{1}{2\pi} \arctan \frac{y_2}{y_1}, \end{aligned} \tag{3.46}$$

yields the following probability distribution [121]

$$p(y_1, y_2) = \frac{1}{\sqrt{2\pi}} e^{-\frac{1}{2}(y_1^2 + y_2^2)}. \tag{3.47}$$

The transformation (3.45) is referred to as the *Box-Muller transform*, which generates two independent random numbers satisfying a Gaussian distribution with zero mean and unit variance.

In order to make this algorithm more efficient, one usually picks two random numbers $\bar{x}_1$ and $\bar{x}_2$, which are homogeneously distributed on the unit circle ($\bar{x}_1^2 + \bar{x}_2^2 < 1$) instead of the unit square [122]. The probability to find the radial coordinate $r = \sqrt{\bar{x}_1^2 + \bar{x}_2^2}$ in the interval $(r, r + \mathrm{d}r)$ is then given by $2r\mathrm{d}r$. Therefore, r obeys the distribution $p(r) = 2r$. Then, the variable r is transformed to $s = r^2$. Satisfying the condition $p(r)\mathrm{d}r = p(s)\mathrm{d}s$, where $\mathrm{d}s = \mathrm{d}(r^2) = 2r\mathrm{d}r$ yields $p(s) = 1$. Therefore, $s = \bar{x}_1^2 + \bar{x}_2^2$ is uniformly distributed in the interval $(0, 1)$ and can be used instead of x_1. Equally so, the angle $\phi = \arctan \bar{x}_2/\bar{x}_1$ divided by 2π is uniformly distributed in the interval $(0, 1)$ and independent of s. So, we can replace x_2 by $\phi/(2\pi)$. Together with the relations $\cos\phi = \bar{x}_1/\sqrt{s}$ and $\sin\phi = \bar{x}_2/\sqrt{s}$ we can write equation (3.45) as

$$\begin{aligned} y_1 &= \sqrt{-2\ln s/s}\bar{x}_1, \\ y_2 &= \sqrt{-2\ln s/s}\bar{x}_2. \end{aligned} \tag{3.48}$$

The advantage is that calculating the trigonometric functions directly can be avoided. Following this polar form, the Box-Muller method then reads: First, we pick two random numbers $\bar{x}_1$ and $\bar{x}_2$, which are uniformly distributed in the interval $(-1, 1)$. Then, we calculate $s = \bar{x}_1^2 + \bar{x}_2^2$ and accept $(\bar{x}_1, \bar{x}_2)$ only if $s < 1$ (otherwise, we pick new numbers). Finally, we obtain two independent Gaussian random numbers y_1 and y_2 by $y_i = \sqrt{-2\ln s/s}\bar{x}_i$.

4 Semiflexible polymer in confined Poiseuille flow

«Everyone is sure of this (that errors are normally distributed), Mr. Lippman told me one day, since the experimentalists believe that it is a mathematical theorem, and the mathematicians that it is an experimentally determined fact.»

Henri Poincaré

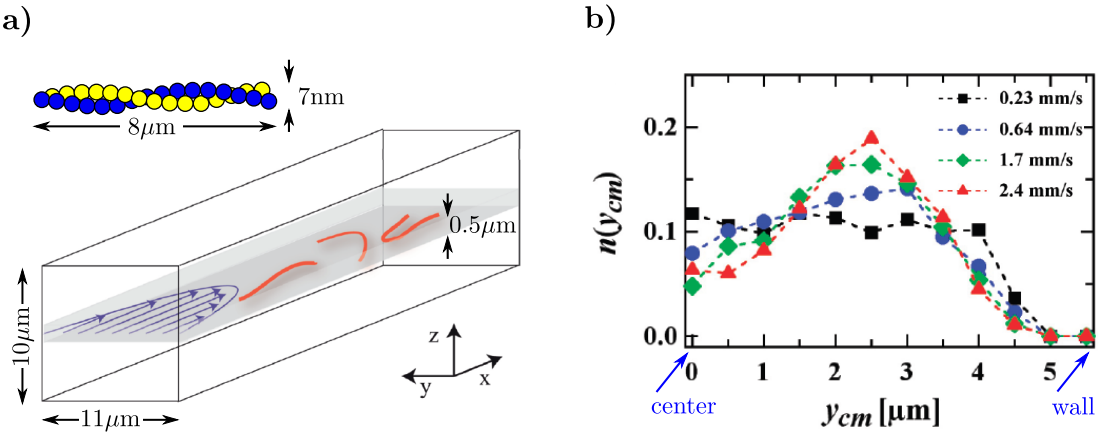

Figure 4.1: Adapted with permission from Ref. [37]. Copyright 2012 American Chemical Society. (a) Schematic sketch of the actin filament and of the experimental setup of Ref. [37]. The filaments are under the influence of a pressure driven Poiseuille flow and they are only considered within the focal plane. (b) Center-of-mass probability distributions of Ref. [37] for different flow velocities. The plot shows the distributions of filaments along the channel cross-section for a half channel with the channel center at $y_{cm} = 0\mu$m and the channel wall at $y_{cm} = 5.5\mu$m.

4.1 Introduction

Polymers are molecules made from repeating units of identical or nearly identical compounds called monomers that are linked together by a series of covalent bonds [123]. They are essential and omnipresent in everyday life, from plastics and elastomers on the one hand to natural biopolymers on the other. Biopolymers such as proteins and nucleic acids play fundamental roles in biological processes. For example, the specific sequence of the four nucleotide bases adenine, guanine, cytosine and thymine in a DNA molecule makes each of us unique. Besides the building block of life, the DNA, actin is also an important component of cells, which is part of the cytoskeleton and play an important role in cellular motility and mechanical stability. Typically, actin filaments have a diameter of a few nanometer, an averaged length of about $5 - 10\mu$m and a persistence length of about 13μm [5]. Due to this properties actin filaments can be used as model systems for semiflexible polymers and, therefore, are central in recent experimental studies [5, 37]. In the experiments in Ref. [37] single α actin filaments with an averaged length of about 8μm are investigated in a squared

microchannel [see figure 4.1(a)]. The channel has a width of 11μm, a height of 10μm and only filaments within the focal plane ($\approx 0.5\mu$m) are considered. The filaments are driven out of equilibrium using a pressure driven Poiseuille flow and analyzed at the end of the microchannel. Besides the conformation and orientation dynamics of the filament the steady state center-of-mass probability distribution was measured, which shows an interesting behavior for different flow velocities [see figure 4.1(a)].

In this chapter we address the flow induced migration of a semiflexible polymer across streamlines by Brownian dynamics simulations. This effect is commonly called cross-streamline migration. We explain it by analyzing the Smoluchowski equation (3.30) for the probability distribution of the polymer's center-of-mass.

In the regime of low Reynolds numbers flexible polymers show cross-streamline migration, which has been intensively studied. A depletion of polymers near walls in planar shear flow as well as in Poiseuille flow was observed in computer simulations [44, 45, 46, 47, 48, 124, 125, 126] and experiments [49, 50, 51]. Since a polymer interacts hydrodynamically with bounding walls, migration towards the centerline occurs, where the thickness of the depletion layer increases with the strength of the flow. This explanation was confirmed by analytical arguments [53, 54] and it describes well repulsion from bounding walls. In addition, simulations reported migration away from the channel's centerline [45, 46, 125, 126], especially under strong confinement [46]. As a result, the maximum concentration of the polymer occurs at a finite distance from the centerline and the depletion in the center increases with flow strength [46, 125, 126]. The spatially varying shear rate of a Poiseuille flow changes orientation and conformation of a polymer within the channel. Close to the walls polymers are stretched and at the center they are coiled [44, 44, 45, 46, 47, 125]. This gives rise to a position-dependent diffusivity and thereby a diffusion current away from the center [45, 46, 53, 125, 126], which generates the observed bimodal concentration profile.

Cross-streamline migration of semiflexible polymers, such as α-actin filaments, is much less studied. Since their bending rigidity significantly determines flow-induced conformations in the Poiseuille flow, we also expect an influence on cross-streamline migration. Indeed, recent experimental [37] and simulation [38, 52] studies report a much more pronounced bimodal concentration profile across the channel when compared to flexible polymers. This effect occurs even under less strong confinement. As for flexible polymers, the concentration profile is also explained by the competition between hydrodynamic polymer-wall interactions and enhanced diffusion away from the centerline.

In this chapter we reexamine the problem and perform Brownian dynamics simulations for a bead-spring chain with bending elasticity. Hydrodynamic interactions between the point-like beads are taken into account by the two-wall Green tensor of the Stokes equations. We indeed observe the bimodal distribu-

tion for the center-of-mass and present results on the orientational order of the end-to-end vector. Generalizing the approach of Ma and Graham [53], we formulate and interpret our findings with the help of a Smoluchowski equation for the center-of-mass probability distribution by carefully analyzing all contributions to the probability current. In contrast to flexible polymers, we show that the deterministic drift current, where hydrodynamic interactions along the polymer are essential, mainly determines the bimodal distribution across the channel, whereas diffusional currents become less important with increasing polymer stiffness. This section is based on publication [A].

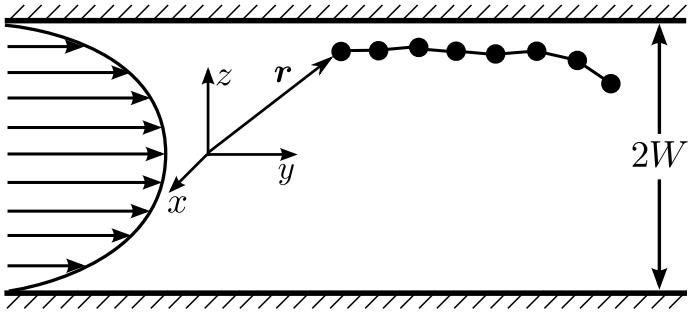

Figure 4.2: A semiflexible polymer modeled by a bead-spring chain with bending rigidity is confined between two parallel planar plates with distance $2W$. The space vector $\boldsymbol{r}_i$ points from the centerline at $z = 0$ to bead i.

4.2 Modeling

In this section we describe how we model a semiflexible polymer in a pressure driven Poiseuille flow. We first introduce the semiflexible polymer as a bead-spring chain with bending elasticity, explain how it couples to the Poiseuille flow, and finally summarize details of our Brownian dynamics simulations. The semiflexible polymer is confined between two parallel planar walls at positions $z = -W$ and $z = W$, which are infinitely extended in the $x - y$ plane (see figure 4.2). For simplicity, we assume that all parts of the chain only move in the $y - z$ plane at $x = 0$. This corresponds to the experiments reported in Ref. [37], where only filaments were recorded and analyzed whose motion occurred in a narrow region ($\pm 0.5 \mu m$) around the focal plane of the microscope. Furthermore, this also reduces our computational efforts considerably. Between the walls a pressure driven Poiseuille flow is created, which we express as

$$\boldsymbol{u}_0(\boldsymbol{r}) = v_0 \left[1 - \left(\frac{z}{W} \right)^2 \right] \boldsymbol{e}_y, \tag{4.1}$$

where v_0 denotes the maximum velocity at the centerline $z = 0$, $\boldsymbol{e}_y$ is the unit vector along the y axis, and W the distance between the centerline and the walls.

4.2.1 The worm-like chain model

A very popular model to describe a polymer is the so called *worm-like chain model*, which was introduced by Kratky and Porod in 1949 [127]. In this model the polymer is described by the curve $\boldsymbol{r}(s)$, where s is the arc length in the interval $[0, L]$ and L the contour length of the polymer (see figure 4.3). It can be shown,

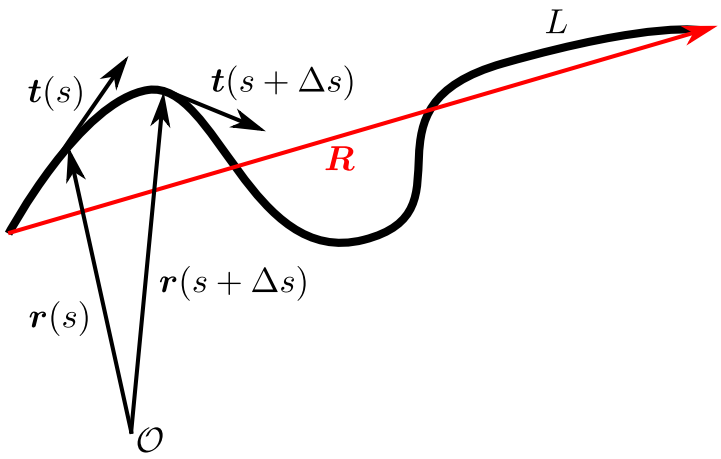

Figure 4.3: Worm-like chain model: the polymer is described by the curve $\boldsymbol{r}(s)$ parametrized by the arc length s. $\boldsymbol{t}(s)$ denotes the tangential vector, L the total contour length and $\boldsymbol{R}$ the *end-to-end vector*

that the correlation of the tangent vector $\boldsymbol{t}(s) = \partial \boldsymbol{r}(s)/\partial s$, $|\boldsymbol{t}(s)| = 1$ is given by [127]

$$\langle \boldsymbol{t}(s) \cdot \boldsymbol{t}(s+\Delta s) \rangle = e^{-\Delta s/L_\mathrm{p}}. \tag{4.2}$$

Here, L_p is the persistence length of the polymer, which quantifies its stiffness. In principle, the mechanical properties of the polymer can be divided into three classes [128]. Is the contour length much larger than the persistence length ($L \gg L_\mathrm{p}$), then the polymer is considered to be flexible, is the contour length much smaller than the persistence length ($L \ll L_\mathrm{b}$) the polymer is considered to be stiff and is the contour length on the same order as the persistence length ($L \approx L_\mathrm{p}$) the polymer is considered to be semiflexible. To illustrate this, we have a look at the correlation of the tangent vectors at the beginning and at the end of the filament

$$\langle \boldsymbol{t}(0) \cdot \boldsymbol{t}(L) \rangle = e^{-L/L_\mathrm{p}}. \tag{4.3}$$

One immediately sees that for flexible polymers ($L \gg L_\mathrm{p}$) the correlation is zero and, therefore, the configuration at the end does not depend on the configuration at the beginning. For semiflexible polymers ($L \approx L_\mathrm{p}$) the correlation is in the order of e^{-1}. In this case the configuration at the end depends on the configuration at the beginning, but the contour does not has to be straight. For stiff polymers ($L \ll L_\mathrm{b}$) the correlation is equal to one and the contour of the polymer is completely straight.

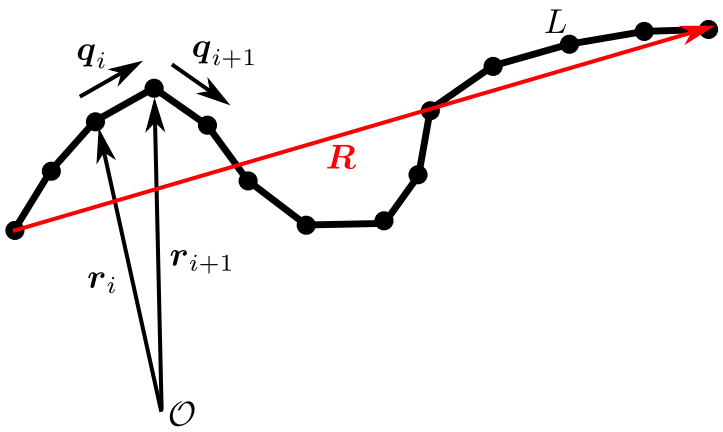

Figure 4.4: Bead-spring model: the polymer is described by N beads, which are connect by $(N-1)$ frictionless springs. Here, $\boldsymbol{q}_n = \boldsymbol{r}_{n+1} - \boldsymbol{r}_n$ denotes the n-th chain segment.

Any deformation of a short segment ds of the filament has an energy cost associated with it. By analogy to Hooke's law, the relationship should be quadratic for small deformations. If we neglect a torsional deformation, the free energy (associated with bending the chain) is given by [129]

$$\mathcal{H} = U^{\mathrm{B}} = \frac{1}{2} \int_0^L \kappa \left(\frac{\partial \boldsymbol{t}(s)}{\partial s} \right)^2 \, \mathrm{d}s. \tag{4.4}$$

Here, $\kappa = L_{\mathrm{p}} k_{\mathrm{B}} T$ denotes the bending rigidity and $\partial \boldsymbol{t} / \partial s$ the change of the tangential vector along the segment ds.

4.2.2 The bead-spring model

Since the hydrodynamic interactions are well described for spherical or point-like particles (see section 2.4), we are using a discretized representation of the worm-like chain model, the so called *bead-spring model*. In this coarse grained model the filament is composed of N beads, which are connected by $(N-1)$ springs (see figure 4.4). We consider that the connecting springs are very thin, so that we can neglect their friction with the surrounding fluid. For this situation, we only have to take the hydrodynamic interactions of the beads into account, for which we know the friction coefficients. The main idea behind this discretisation is to describe the stretching and bending forces such that they act on finite discrete points on the filament, such that we can apply the methods we derived in section 2.5.2.

To account for the constant contour length of the polymer, we apply Hooke's law on each chain segment. So, the total energy stored in stretching the polymer is determined by the sum over the squared deviations of each segment from its equilibrium length $l = \langle q_n \rangle$

$$U^{\mathrm{S}} = \frac{1}{2} H \sum_{n=1}^{N-1} (q_n - l)^2, \tag{4.5}$$

where $q_n = |\boldsymbol{q}_n|$ is the length of the n-th chain segment

$$\boldsymbol{q}_n = \boldsymbol{r}_{n+1} - \boldsymbol{r}_n. \tag{4.6}$$

A single chain segment cannot be bended, but neighbouring segments may be inclined to each other. To obtain an expression for the discretized bending energy, we simply substitute $\mathrm{d}\boldsymbol{t}$ with $(\boldsymbol{q}_{n+1}/q_{n+1} - \boldsymbol{q}_n/q_n)$ and $\mathrm{d}s$ with l in equation (4.4). Therefore, we obtain [130]

$$U^{\mathrm{B}} = \frac{\kappa}{l} \sum_{n=1}^{N-2} \left(1 - \frac{\boldsymbol{q}_{n+1}}{q_{n+1}} \cdot \frac{\boldsymbol{q}_n}{q_n} \right). \tag{4.7}$$

Finally, the force acting on bead n due to bending and stretching the bead-spring chain follows from

$$\boldsymbol{F}_n = -\nabla_n (U^{\mathrm{B}} + U^{\mathrm{S}}), \tag{4.8}$$

where ∇_n is the nabla operator with respect to the position vector $\boldsymbol{r}_n$.

4.2.3 Equations of motion

The beads in the model polymer also experience stochastic forces due to collisions with fluid molecules from the surrounding solvent. As usual, we take them into account as Gaussian white noise that obeys the fluctuation-dissipation theorem (see section 3.1). Using a compact notation, the resulting Langevin equation in differential form reads [114, 131]

$$\mathrm{d}\boldsymbol{x} = \left[\boldsymbol{u}_0 + \frac{1}{k_B T} \boldsymbol{D}\boldsymbol{F} + \nabla \boldsymbol{D} \right] \mathrm{d}t + \boldsymbol{H}\boldsymbol{n}\sqrt{\Delta t}\ , \tag{4.9}$$

$$\text{with } \boldsymbol{D} = k_B T \boldsymbol{\mu} = \frac{1}{2} \boldsymbol{H}\boldsymbol{H}^T. \tag{4.10}$$

Here we have introduced $3N$ dimensional vectors to collect the positions of the beads, $\boldsymbol{x} = (\boldsymbol{r}_1, ..., \boldsymbol{r}_N)$, the forces acting on them, $\boldsymbol{F} = (\boldsymbol{F}_1, ..., \boldsymbol{F}_N)$, and the velocities from the external flow field at the positions of the beads, $\boldsymbol{u}_0 = (\boldsymbol{u}_0(\boldsymbol{r}_1), ..., \boldsymbol{u}_0(\boldsymbol{r}_N))$. The mobilities $\boldsymbol{\mu}_{ij}^{\mathrm{tt}}$ form the mobility tensor $\boldsymbol{\mu}$ and $\boldsymbol{D}$ stands

for the generalized diffusion tensor, where k_B is Boltzmann's constant and T the absolute temperature. The tensor $\boldsymbol{H}$ is determined such that it fulfills equation (4.10) (see section 3.3.2). Finally, $\boldsymbol{n}$ denotes a random vector with expectation values for the mean and the second moment,

$$\langle \boldsymbol{n} \rangle = 0 \quad \text{and} \quad \langle \boldsymbol{n} \otimes \boldsymbol{n} \rangle = \mathbf{1}. \tag{4.11}$$

The first term on the right hand side in equation (4.9) describes the drift motion of the beads, including the noise-induced spurious drift ($\nabla \boldsymbol{D}$), and the second term their Brownian motion [131]. To numerically integrate Eqs. (4.9), we use a predictor-corrector scheme summarized in section 3.3.1 to avoid the explicit calculation of $\nabla \boldsymbol{D}$. An Euler step without the spurious drift generates an intermediate configuration $\bar{\boldsymbol{x}}(t + \Delta t) = \boldsymbol{x}(t) + \Delta \bar{\boldsymbol{x}}$ with

$$\Delta \bar{\boldsymbol{x}} = \left[\boldsymbol{u}_0 + \frac{1}{k_B T} \boldsymbol{D} \boldsymbol{F} \right] \Delta t + \boldsymbol{H} \boldsymbol{n} \sqrt{\Delta t}. \tag{4.12}$$

Then the corrector step calculates the final configuration $\boldsymbol{x}(t + \Delta t) = \boldsymbol{x}(t) + \Delta \boldsymbol{x}$ with

$$\begin{aligned} \Delta \boldsymbol{x} \;=\; & \frac{1}{2} \left[\boldsymbol{u}_0 + \bar{\boldsymbol{u}}_0 + \frac{1}{k_B T} \left(\boldsymbol{D} \boldsymbol{F} + \bar{\boldsymbol{D}} \bar{\boldsymbol{F}} \right) \right] \Delta t \\ & + \frac{1}{2} \left[\mathbf{1} + \bar{\boldsymbol{D}} \boldsymbol{D}^{-1} \right] \boldsymbol{H} \boldsymbol{n} \sqrt{\Delta t}. \end{aligned} \tag{4.13}$$

Here the symbol "$\bar{}$" means that these quantities are calculated for the intermediate configuration $\bar{\boldsymbol{x}}$.

4.2.4 System parameters

In the experiments in Ref. [37], α-actin filaments with a contour length of about $L = 8\mu$m were analyzed in a microchannel with a square cross section of width $2W = 10\mu$m. The actin filament is a thin semiflexible biopolymer with a diameter of 8nm and a persistence length of $L_p = 13\mu$m. This gives the experimental value $L_p/L = 1.6$. The velocity of the imposed Poiseuille flow at the centerline varied from $v_0 = 0$mm/s to $v_0 = 2.4$mm/s. To be close to the experimental values, we choose the following parameters for our simulations. We set the width of the channel to the experimental value, $2W = 10\mu$m, and refer all our lengths to W. The polymer consists of $N = 16$ monomers and the equilibrium bond length to the nearest neighbor is $l/W = 0.1$ so that the total contour length amounts to $L/(2W) = 0.75$. The bead radius is set to $a/W = 0.005$ meaning $l/a = 20$ which allows to treat the beads as point particles when hydrodynamic interactions are calculated. The spring constant is set to $H = 1.2 \cdot 10^4 (k_B T/W^2)$ and we will

explore how the model polymer behaves when the persistence length varies from $L_p/L = 1$ to $L_p/L = 16$. We use the viscosity of water, $\eta_{H_2O} = 0.01$P, and perform the Brownian dynamics simulations at a temperature $T = 300$K. The imposed flow velocity at the centerline varies from $v_0 = 0$mm/s to $v_0 = 2.5$mm/s. The configurational update of the polymer is calculated after a time step of $\Delta t = 10^{-5}$s. Since the evaluation of the two-wall Green tensor at each time step is very time consuming, we stored its values on a grid with 200×200 grid points and with a mesh size of $0.01W$. Tensor values at intermediate locations are determined from the grid points by linear interpolation. The probability distribution and all averages presented in the following sections are calculated after the polymer reached its steady state for various independent initial conditions.

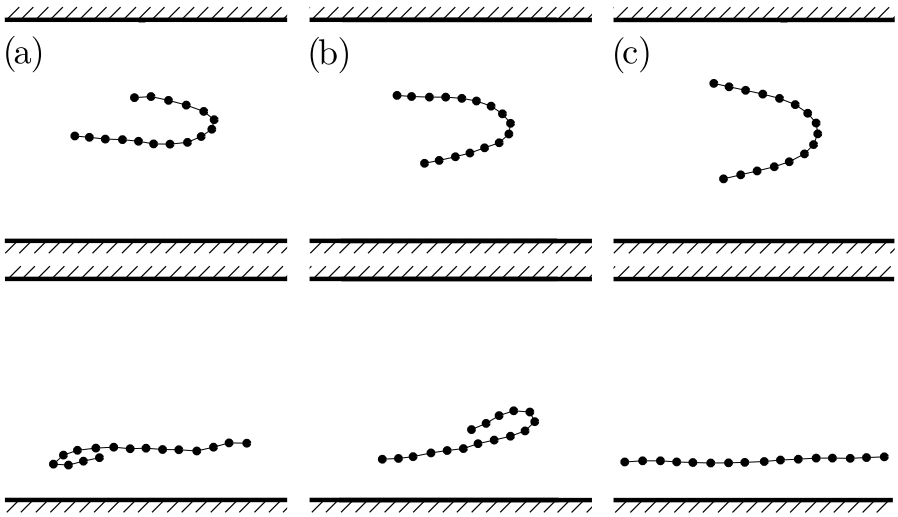

Figure 4.5: Snapshots of the bead-spring chain for different persistence lengths at the centerline (top) and near the wall (bottom) at $v_0 = 2.5$mm/s. (a) $L_p/L = 1$, (b) $L_p/L = 4$, and (c) $L_p/L = 16$.

4.3 Results

The imposed parabolic Poiseuille flow of equation (4.1) drives the filament out of equilibrium and determines its steady state, which we quantify, e.g., by the center-of-mass probability distribution $n(z_C)$. In this section we will investigate how flow strength, hydrodynamic interactions, polymer stiffness, and the ratio between bond length and bead radius, l/a, influence the polymer conformation, the center-of-mass distribution $n(z_C)$, and the orientational order of the filament's end-to-end vector.

Figure 4.5 shows different snapshots of the filament near the centerline and near a bounding wall. The filament constantly moves up and down along the lateral direction. Most of the time, it is aligned parallel to the flow direction although it is not perfectly straight. At the centerline, we also observe that the filament bends to a typical U shape that traces the Poiseuille flow profile (see figure 4.5, top). This configuration is not stable when the filament moves away from the centerline. Outside the center, the filament also tumbles when the front end moves closer to the walls where it experiences a smaller flow velocity (see figure 4.5, bottom). After one tumbling event, the filament aligns along the flow field until thermal motion moves the front end again closer to the wall. Increasing

v_0 also increases the local shear rates and thereby the tumbling frequency.

4.3.1 Polymer conformation and orientation

To study how the Poiseuille flow influences the filament shape and orientation within the channel, we calculate the end-to-end vector $\boldsymbol{R}$ and determine its orientational order around the channel axis by the order parameter S

$$S(z_C) = \langle \cos(2\theta) \rangle \,. \tag{4.14}$$

Here θ is the angle between $\boldsymbol{R}$ and the y axis and S describes the orientational order in a two-dimensional system [132]. A polymer with randomly oriented end-to-end vector gives $S = 0$, whereas $S = 1$ means that the polymer is perfectly aligned along the flow direction and $S = -1$ indicates perfect orientation perpendicular to the flow direction.

Figures 4.6 (a) and (b) show, respectively, the orientational order parameter and the average end-to-end distance $\langle R \rangle$ for different flow strengths. Without flow, S is nearly zero within the region $|z_C|/W \leq 0.25$, where the filament can freely rotate and where it assumes all orientations with equal probability. Outside this region, the filament's orientation is more and more restricted due to the steric polymer-wall interaction and S grows monotonically until it reaches $S = 1$ at the walls. For a rigid rod, one readily derives the order parameter as a function of $|z_C|/W$:

$$S(z_C) = \begin{cases} 1, & |z_C|/W \leq 1 - L/2W \\ \dfrac{u\sqrt{1-u^2}}{\arcsin u}, & 1 - L/2W < |z_C|/W \leq 1, \end{cases} \tag{4.15}$$

where u is given in equation (4.17). The inset of figure 4.6(a) shows very good agreement with our simulations. Deviations result from thermal fluctuations of the filament. They also explain that the end-to-end distance in figure 4.6(b) deviates slightly from one. In the presence of external flow both the order parameter and the end-to-end distance have a minimum in the center of the channel which we attribute to the U-shaped conformations illustrated at the bottom of figure 4.5. S and $\langle R \rangle$ then increase monotonically until a nearly constant value or plateau is reached around $|z|/W = 0.2$. Here the filament is aligned along the flow ($S > 0.7$) and tumbling events cause the end-to-end distance to be smaller than for zero flow field. The end-to-end distance shows a weak minimum near the wall which we attribute to an increasing number of tumbling events since the shear stress on the filament within the channel becomes largest. Finally, very close to the wall, when tumbling events can no longer occur, the filament is perfectly aligned with the flow. The order parameter S reaches its maximum

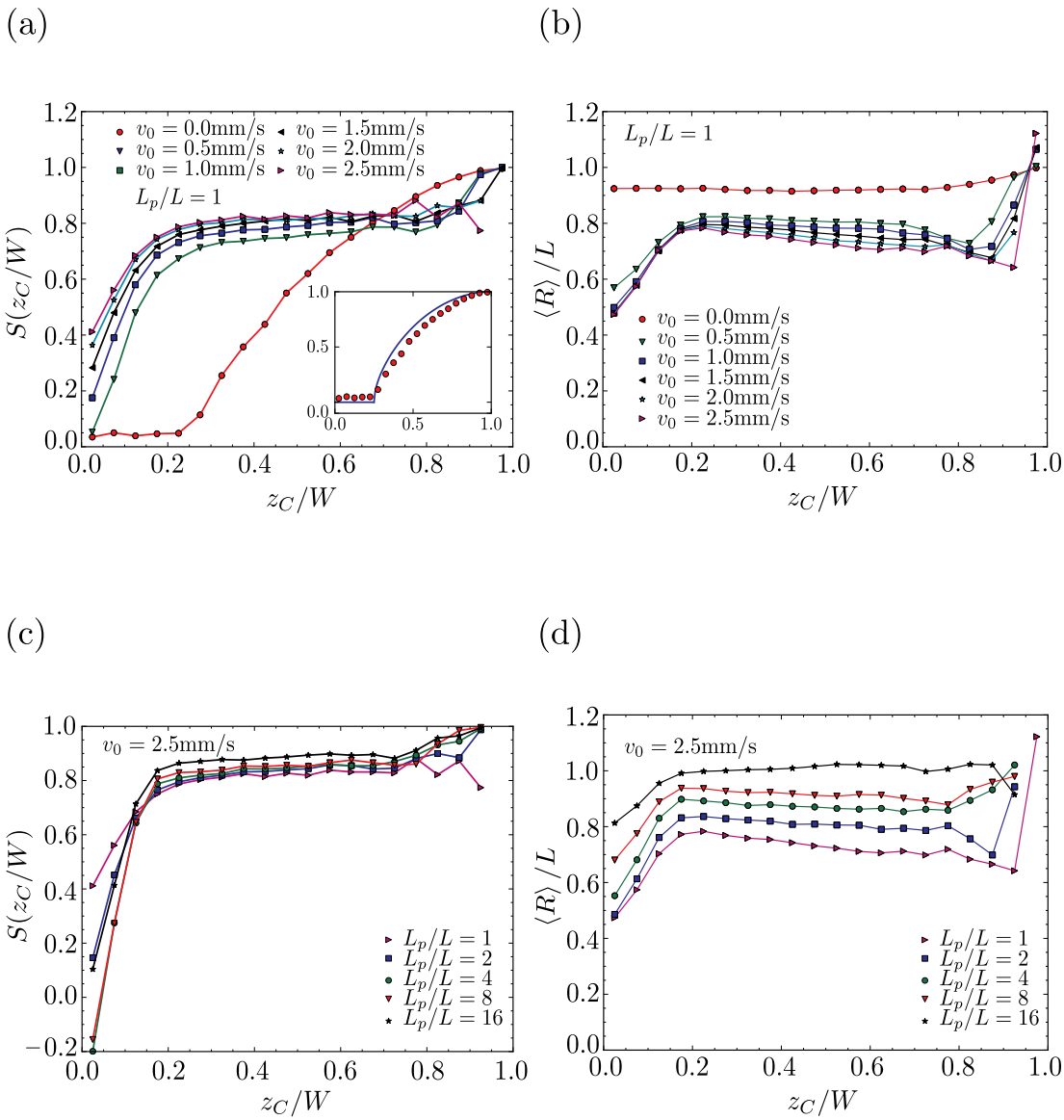

Figure 4.6: Order parameter S and average end-to-end distance $\langle R\rangle$ plotted versus the lateral center-of-mass position z_C/W: (a),(b) for a fixed stiffness $L_p/L = 1$ and different flow velocities; (c),(d) for a fixed flow velocity $v_0 = 2.5$mm/s and different stiffnesses L_p/L. Inset in (a): For $v_0 = 0$mm/s, the simulated order parameter S is compared to the analytic result of equation (4.15).

value one and the end-to-end distance even shows values above L for large flow strengths. Interestingly, the plateau value of S increases with the flow strength while $\langle R \rangle$ decreases. Higher shear rates align the filament better along the flow direction but they also initiate more tumbling events which reduce $\langle R \rangle$ but not S. We repeated our simulations without hydrodynamic interactions acting across the filament and from the wall. The results agree well with the behavior discussed in Figs. 4.6 (a) and (b). The same behavior occurs when we reduce the ratio l/a of bond length to bead radius from the value $l/a = 20$ used in most of our simulations to $l/a = 5$, where hydrodynamic interactions between the beads are stronger. This indicates that overall shape and orientation of the filament is determined by its overall friction with the solvent and in particular by the applied Poiseuille flow.

For stiffer filaments the end-to-end distance $\langle R \rangle$ increases as indicated in figure 4.6(d). The plateau value of the order parameter in figure 4.6(c) does not change strongly when the stiffness increases. Interestingly, the minimum value for S at the centerline first decreases to even negative values and then increases again. The negative values are caused by the U-shaped conformation where the end-to-end vector is perpendicular to the centerline. A persistence length L_P/L between 4 and 8 seems to be the best choice for realizing the U-shaped conformation.

4.3.2 Steady state center-of-mass distribution

One quantity to characterize the filament within the microchannel is the steady-state probability distribution $n(z_C)$ for its center-of-mass across the channel. We always normalize it to one, $\int_{-W}^{W} n(z)\mathrm{d}z = 1$. The experiments of Ref. [37] clearly revealed that the distribution depends on how strongly the filament is driven out of equilibrium. In figure 4.7 we plot the distribution for different flow strengths v_0 from the centerline to the bounding wall. Without flow the center-of-mass location z_C is equally distributed within the interval $|z_C|/W \leq 1 - L/2W = 0.25$. In thermal equilibrium, such a behavior is expected for the freely moving filament with arbitrary orientation. For locations z_C closer to the walls, the orientation of the stiff filament is more and more restricted due to the steric interaction with the wall and the distribution decreases to zero at the walls. For a rigid rod, one readily derives the distribution

$$n(z_C) = \begin{cases} \dfrac{\pi}{2(\pi - L/W)}, & |z_C|/W \leq 1 - L/2W \\ \dfrac{\arcsin u}{\pi - L/W}, & 1 - L/2W < |z_C|/W \leq 1 \end{cases} \tag{4.16}$$

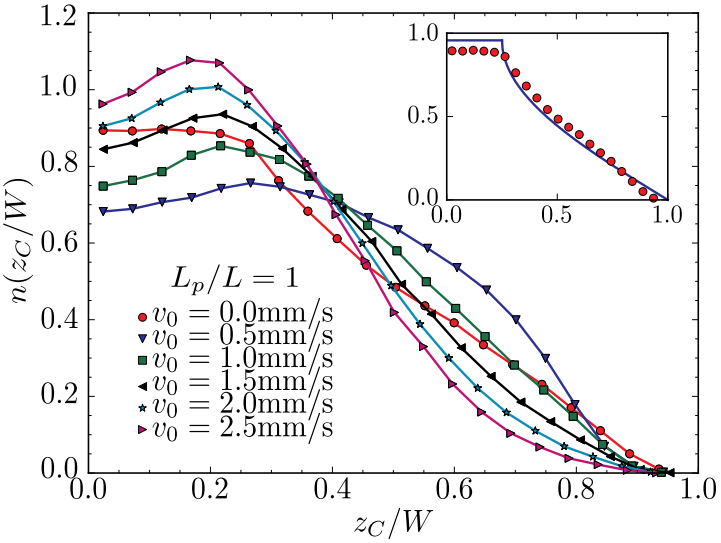

Figure 4.7: Center-of-mass probability distribution plotted from the centerline ($z_C = 0$) to the wall ($z_C = W$) for different flow velocities v_0 and a persistence length of $L_P/L = 1$. The inset compares the simulation results for zero flow velocity v_0 to the hard-needle distribution of equation (4.16).

with

$$u = \frac{1 - |z_C|/W}{L/2W}, \tag{4.17}$$

which is compared to the simulated profile in the inset of figure 4.7. Deviations result from thermal fluctuations of the filament. When we turn on the Poiseuille flow (see figure 4.7, $v_0 = 0.5$mm/s), the probability distribution close to the wall first increases. We understand this behavior. The tumbling events illustrated in figure 4.5 (bottom) and initiated by the Poiseuille flow allow the filament to move closer to the wall. Increasing the flow velocity further, the filament is depleted more and more at both walls. This is initiated by the hydrodynamic repulsion of the filament from the wall, which pushes it away from the wall [45, 53, 54]. The repulsion becomes clear with the help of figure 2.5 on the left. Due to the strong shear flow close to the wall, the filament is under tension which initiates a flow field that drives the model polymer away from the wall [45, 53]. In particular, at both ends of the rod tensional forces point into the rod. Each of these forces initiates a flow field similar to the one of figure 2.5(a) which drives the other end of the rod away from the wall. This phenomenon is different from the orientational lift forces reported in Ref. [54]. The most pronounced behavior

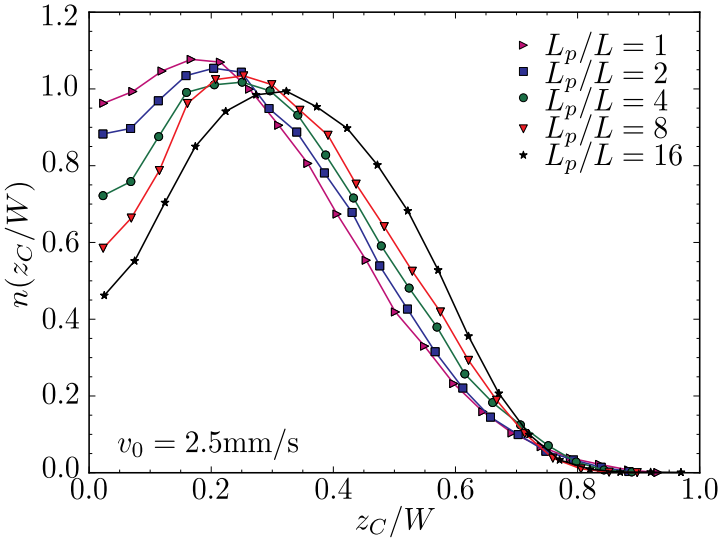

Figure 4.8: Center-of-mass probability distributions for different persistence lengths L_P/L at a fixed center flow velocity $v_0 = 2.5\text{mm/s}$.

of the system is the depletion of the distribution at the centerline. It leads to a bimodal probability density with a maximum at a finite distance from the center. The maximum increases with the flow strength. At the maximum, the migration towards the centerline induced by the hydrodynamic filament-wall interaction has to be cancelled by a probability current away from the centerline. Based on literature [45, 48, 53], Refs. [37, 38, 52] attribute such a current to the spatially varying diffusivity of the filament across the channel: the U-shaped conformation at the centerline has a larger diffusivity than the straight filament outside the center. In section 4.4 we will demonstrate that the current away from the center is mainly due to deterministic drift motion which becomes dominant over the diffusional current when the rigidity of the filament increases. Figure 4.8 shows the center-of-mass distributions at a fixed flow velocity $v_0 = 2.5\text{mm/s}$ for different persistence lengths L_P. Here, the depletion layer at the walls decreases slightly with increasing bending rigidity, whereas the bimodal distribution becomes more pronounced. For larger rigidity, the migration away from the centerline increases. As a result, the depletion at $z_C = 0$ becomes stronger and the position of the maximum is shifted towards the walls which causes the decreasing depletion layer. We will explain this behavior in section 4.4. For $L_P/L = 16$, the local minimum and the maximum of the distribution differ by a factor of two, which is comparable to the results of Ref. [37].

Most of our simulations are done for a bead distance to radius of $l/a = 20$.

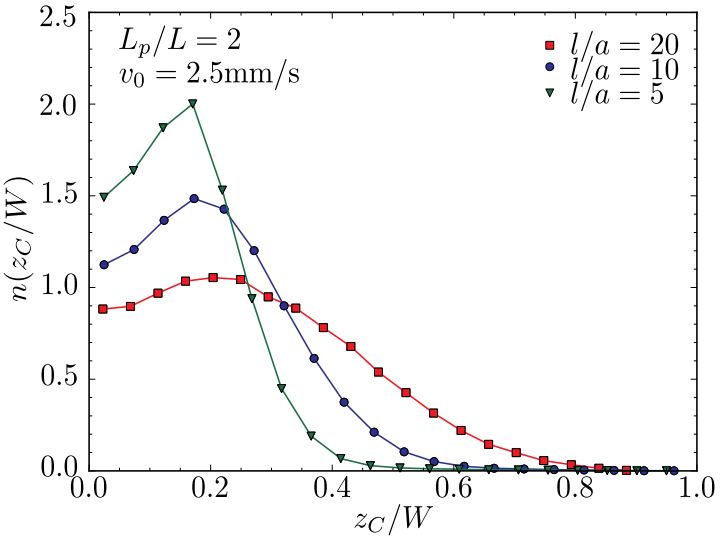

Figure 4.9: Center-of-mass probability density for different ratios l/a at a fixed persistence length $L_P/L = 2$ and a fixed flow velocity $v_0 = 2.5\text{mm/s}$. In order to change the ratio l/a, we keep the length L and the number of beads N constant and vary the radius a of the beads. This corresponds to increasing the thickness of our model polymer.

This might mimic the thin actin filament. However, it also underestimates the overall friction between the filament and the solvent. In figure 4.9 the center-of-mass distributions for different bead sizes a at a fixed flow velocity $v_0 = 2.5\text{mm/s}$ are shown. Increasing the overall friction of the model polymer with a enhances tensional forces within the polymer and thereby the drift currents discussed in section 4.4. As a result, the bimodal distribution and the depletion at the walls become more pronounced.

Hydrodynamic interactions between different parts of the model polymer and with the wall are crucial for the observed bimodal distribution and the depletion at the walls. In figure 4.10 we show the resulting center-of-mass distributions at different flow strengths when hydrodynamic interactions are switched off during the simulations. The equilibrium profile at zero flow field is the same as in figure 4.7 since it should not depend on dynamic properties such as hydrodynamic interactions. For nonzero flow velocity, the minimum in the center vanishes compared to figure 4.7 whereas the depletion close to the wall is less pronounced. It even decreases with increasing v_0 since the hydrodynamic repulsion from the wall is missing and the tumbling polymer is stronger confined due to larger viscous shear stresses [37].

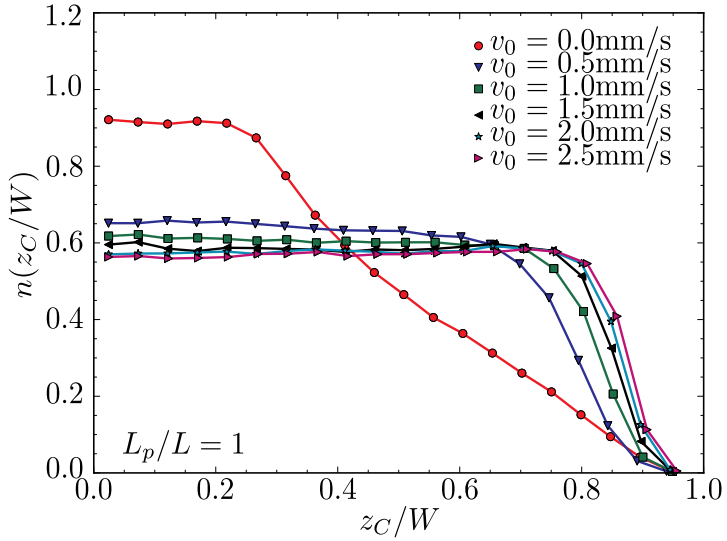

Figure 4.10: Center-of-mass probability distribution simulated without hydrodynamic interactions for different flow velocities v_0 and persistence length $L_P/L = 1$.

4.4 Kinetic theory for a semiflexible polymer

In this section we derive and analyze a Smoluchowski equation for the center-of-mass probability distribution of the bead-spring chain with bending elasticity. We thereby generalize the approach of Ma and Graham who formulated a kinetic theory for a bead-spring dumbbell [53]. We derive the Smoluchowski equation in section 4.4.1 and study and discuss in detail the different contributions to the lateral center-of-mass current in section 4.4.2 in order to identify the cause for cross-streamline migration.

4.4.1 Smoluchowski equation for center-of-mass current

The probability distribution $\psi(\boldsymbol{r}_1, ..., \boldsymbol{r}_N; t)$ for finding the bead-spring chain in a state determined by the bead coordinates $\boldsymbol{r}_1, ..., \boldsymbol{r}_N$ at time t is governed by the Smoluchowski equation

$$\frac{\partial}{\partial t}\psi = -\nabla_i \cdot \boldsymbol{j}_i \ , \tag{4.18}$$

where we have introduced the probability density current of bead i

$$\boldsymbol{j}_i = \dot{\boldsymbol{r}}_i \psi - \boldsymbol{D}_{ij} \nabla_j \psi. \tag{4.19}$$

Here,

$$\dot{\boldsymbol{r}}_i = \boldsymbol{u}_0(\boldsymbol{r}_i) + \boldsymbol{\mu}_{ij}^{\mathrm{tt}} \boldsymbol{F}_j \tag{4.20}$$

denotes the deterministic drift velocity and $\boldsymbol{D}_{ij} = k_B T \boldsymbol{\mu}_{ij}^{\mathrm{tt}}$ is the diffusion tensor connected to the mobility tensor by the Einstein relation. Note that we use the convention where we sum over bead indices that occur twice in an expression. Since we are interested in the center-of-mass probability distribution, we introduce the respective center-of-mass position and bond vectors,

$$\begin{aligned} \boldsymbol{r}_C &= \frac{1}{N} \sum_{i=1}^{N} \boldsymbol{r}_i, \\ \boldsymbol{q}_n &= \boldsymbol{r}_{n+1} - \boldsymbol{r}_n, \qquad n = 1, \ldots, N-1. \end{aligned} \tag{4.21}$$

Using the new coordinates and

$$\nabla_i = \frac{1}{N} \nabla_{r_C} + \nabla_{q_{i-1}} - \nabla_{q_i}, \tag{4.22}$$

we rewrite the Smoluchowski equation (4.18) as

$$\begin{aligned} \frac{\partial \psi}{\partial t} &= -\nabla_{r_C} \cdot (\dot{\boldsymbol{r}}_C \psi - \boldsymbol{D}_{r_C} \nabla_{r_C} \psi - \boldsymbol{D}_{q_i}^{\mathrm{T}} \nabla_{q_i} \psi) \\ &\quad -\nabla_{q_i} \cdot (\dot{\boldsymbol{q}}_i \psi - \boldsymbol{D}_{q_i} \nabla_{r_C} \psi - \bar{\boldsymbol{D}}_{ij} \nabla_{q_j} \psi). \end{aligned} \tag{4.23}$$

We have introduced the respective deterministic velocities for center-of-mass and bond i,

$$\dot{\boldsymbol{r}}_C = \frac{1}{N} \sum_i (\boldsymbol{u}_0(\boldsymbol{r}_i) + \boldsymbol{\mu}_{ij}^{\mathrm{tt}} \boldsymbol{F}_j) \tag{4.24}$$

$$\dot{\boldsymbol{q}}_i = \boldsymbol{u}_0(\boldsymbol{r}_{i+1}) - \boldsymbol{u}_0(\boldsymbol{r}_i) + \boldsymbol{\mu}_{i+1,j}^{\mathrm{tt}} \boldsymbol{F}_j - \boldsymbol{\mu}_{ij}^{\mathrm{tt}} \boldsymbol{F}_j \tag{4.25}$$

$$\tag{4.26}$$

and various diffusivities

$$\boldsymbol{D}_{r_C} = \frac{1}{N^2} \sum_{i,j}^{N} \boldsymbol{D}_{ij}, \tag{4.27}$$

$$\boldsymbol{D}_{q_i} = \frac{1}{N} \sum_{j}^{N} \boldsymbol{D}_{i+1,j} - \boldsymbol{D}_{ij}, \tag{4.28}$$

$$\bar{\boldsymbol{D}}_{ij} = \boldsymbol{D}_{i+1,j+1} - \boldsymbol{D}_{i,j+1} - \boldsymbol{D}_{i+1,j} + \boldsymbol{D}_{ij}. \tag{4.29}$$

The average over all diffusion tensors $\boldsymbol{D}_{ij}$ is the Kirkwood diffusivity $\boldsymbol{D}_{r_C}$, whereas $\boldsymbol{D}_{q_i}$ and $\bar{\boldsymbol{D}}_{ij}$ are diffusivities related to the bond vectors. We now write the full

probability distribution ψ in the new coordinates $\boldsymbol{r}_C, \boldsymbol{q}_1, \ldots, \boldsymbol{q}_{N-1}$ and introduce the center-of-mass probability distribution

$$n(\boldsymbol{r}_C, t) = \int \ldots \int \psi(\boldsymbol{r}_C, \boldsymbol{q}_1, \ldots, \boldsymbol{q}_{N-1}; t) \mathrm{d}\boldsymbol{q}_1 \ldots \mathrm{d}\boldsymbol{q}_{N-1}. \tag{4.30}$$

Integrating equation (4.23) over all bond vectors $\boldsymbol{q}_i$, one is able to derive a Smoluchowski equation for the center-of-mass,

$$\frac{\partial n}{\partial t} = -\nabla_{r_C} \cdot \boldsymbol{j}_C, \tag{4.31}$$

with the center-of-mass probability current

$$\begin{aligned} \boldsymbol{j}_C &= \Big[\langle \dot{\boldsymbol{r}}_C \rangle_q - \nabla_{r_C} \langle \boldsymbol{D}_{r_C} \rangle_q + \langle \nabla_{r_C} \boldsymbol{D}_{r_C} \rangle_q \\ &\quad + \left\langle \nabla_{q_i} \boldsymbol{D}_{q_i}^{\mathrm{T}} \right\rangle_q \Big] n - \langle \boldsymbol{D}_{r_C} \rangle_q \nabla_{r_C} n. \end{aligned} \tag{4.32}$$

The brackets $\langle \ldots \rangle_q$ denote an ensemble average over all bond vectors $\boldsymbol{q}_i$ or polymer conformations with fixed $\boldsymbol{r}_C$,

$$\langle A \rangle_q = \int \ldots \int A \hat{\psi} \mathrm{d}\boldsymbol{q}_1 \ldots \mathrm{d}\boldsymbol{q}_{N-1}, \tag{4.33}$$

where

$$\hat{\psi}(\boldsymbol{r}_C, \boldsymbol{q}_1, \ldots, \boldsymbol{q}_{N-1}; t) = \frac{\psi(\boldsymbol{r}_C, \boldsymbol{q}_1, \ldots, \boldsymbol{q}_{N-1}; t)}{n(\boldsymbol{r}_C, t)}. \tag{4.34}$$

Note that the second and third terms on the right-hand side of equation (4.32) are not necessarily the same. In integrating equation (4.23) over all bond vectors $\boldsymbol{q}_i$, we use the reasonable assumption that all surface terms vanish. We therefore can immediately skip the terms in the second line of equation (4.23). In the remaining terms, ψ is replaced by $n\hat{\psi}$ from equation (4.34) and partial integrations are performed such that no gradient acts on $\hat{\psi}$ and equation (4.33) can be applied. This procedure finally gives the center-of-mass probability current (4.32).

Equations (4.31) and (4.32) determine the center-of-mass probability distribution. Whereas the last term on the right-hand side of equation (4.32) describes conventional diffusion [53], the remaining terms proportional to the distribution n formally are drift terms. However, only the first term is due to deterministic motion of the center-of-mass. The second to fourth terms result from the diffusional currents in equation (4.19). As we demonstrate explicitly in the following section, all of these terms, in principle, can lead to cross-streamline migration. Here we add some general remarks.

The first term on the right-hand side of equation (4.32) describes migration due to hydrodynamic interactions and the applied external flow. Without hydrodynamic interactions the cross mobilities $\boldsymbol{\mu}_{ij}^{\mathrm{tt}}$ vanish and equation (4.24) reduces to $\dot{\boldsymbol{r}}_C = \sum_i [\boldsymbol{u}_0(\boldsymbol{r}_i)]/N$. The frictional term $\sum_i \boldsymbol{\mu}_{ii}^{\mathrm{tt}} \boldsymbol{F}_i = (\sum_i \boldsymbol{F}_i)/(6\pi\eta a) = \boldsymbol{0}$ does not contribute to the center-of-mass motion since the total force acting on the filament has to be zero. As a result, without hydrodynamic interactions cross-streamline migration cannot occur. The second term on the right-hand side of equation (4.32) is the divergence of the Kirkwood diffusivity and a natural candidate for migration away from the centerline as demonstrated in Refs. [45, 53]. Finally, the third and fourth term vanish whenever the divergence of the diffusion tensors or mobilities is zero. In particular, this is the case in an unbounded fluid when one treats hydrodynamic interactions on the level of the Oseen tensor or in the next higher order via the Rotne-Prager tensor. In our case, the third and fourth term will be non-zero due to wall-induced hydrodynamic interactions.

4.4.2 Analysis of the lateral center-of-mass current

Due to translational symmetry along the channel direction, the center-of-mass distribution does not vary along the y axis and the z component of the center-of-mass current, i.e., the current across the channel is

$$\begin{aligned} j_{C,z} &= \Big[\langle \dot{z}_C \rangle_q - \partial_{z_C} \langle D_{r_C,zz} \rangle_q + \langle \partial_{z_C} D_{r_C,zz} \rangle_q \\ &\quad + \Big\langle \partial_{q_i,y} D^{\mathrm{T}}_{q_i,zy} + \partial_{q_i,z} D^{\mathrm{T}}_{q_i,zz} \Big\rangle_q \Big] n \\ &\quad - \langle D_{r_C,zz} \rangle_q \, \partial_{z_C} n. \end{aligned} \tag{4.35}$$

In steady state the center-of-mass current $\boldsymbol{j}_C$ is constant. Since the current at the walls has to vanish, $j_{C,z}$ is zero everywhere across the channel. In figure 4.11, we plot all contributions of the center-of-mass current $j_{C,z}$ proportional to n for different bending rigidities of the filament. The sum of these currents balances the diffusional current $-\langle D_{r_C,zz} \rangle_q \, \partial_{z_C} n$. Concentrating on $L_P/L = 1$, we recognize that close to the wall the deterministic drift current $\langle \dot{z}_C \rangle_q \, n$ is directed away from the wall, e.g., it is positive at $z_c = -W$, and it dominates all the other currents. Hence, the hydrodynamic repulsion from the walls is responsible for the depletion at the walls. On the other hand, close to the centerline, the current is directed towards the wall and, therefore, causes depletion at the centerline. For $L_P/L = 1$, the diffusional current $-\partial_{z_C} \langle D_{r_C,zz} \rangle_q \, n$ due to the gradient of the conformation-averaged Kirkwood diffusivity also points away from the centerline and contributes to the observed depletion. We understand this since the U-shaped conformation close to the centerline has a larger diffusivity than the straight conformation occuring outside the centerline [45, 53]. However, already at a

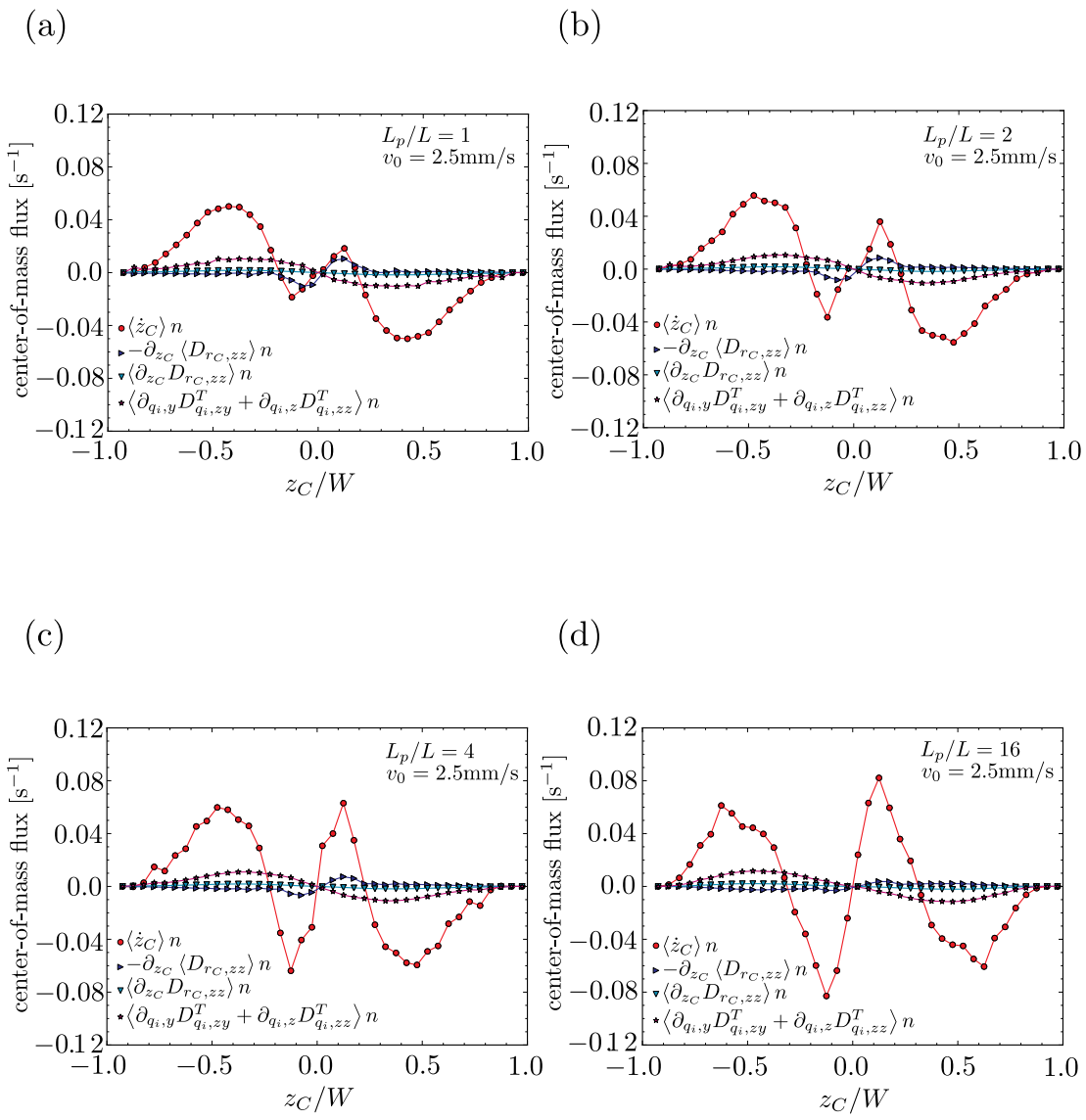

Figure 4.11: Plots of the different contributions of the lateral center-of-mass current across the channel at flow velocity $v_0 = 2.5$mm/s for different bending rigidities: (a) $L_P/L = 1$, (b) $L_P/L = 2$, (c) $L_P/L = 4$, and d) $L_P/L = 16$.

stiffness of $L_P/L = 2$, the deterministic drift current is clearly the dominant part for causing centerline depletion and at $L_P/L = 16$ all the diffusional currents are negligible. The experiments of Ref. [37] were performed for $L_p/L = 1.6$. So, we

conclude that the observed centerline depletion is mainly due to the deterministic drift current. The third term $\langle \partial_{z_C} D_{r_C,zz} \rangle_q \, n$ is approximately zero for each L_p/L and the fourth term $\left\langle \partial_{q_i,y} D^{\mathrm{T}}_{q_i,zy} + \partial_{q_i,z} D^{\mathrm{T}}_{q_i,zz} \right\rangle_q n$ leads to a current towards the centerline due to hydrodynamic repulsion from the wall.

We summarize our results here. Whereas the filament at the centerline displays more compact conformations like the U shape, close to the walls it is mainly aligned along the flow lines due to the large shear rate. Therefore, the friction coefficient for motion across the channel increases from the centerline to the wall and its inverse, the Kirkwood diffusivity, decreases monotonically from the centerline towards both walls. This initiates migration away from the centerline [45, 53, 54], which can cause centerline depletion [45, 53, 125, 126], and was therefore used to interpret the recent experiments of Steinhauser *et al.* [37, 52]. Here we demonstrate that for increasing bending rigidity, centerline depletion is mainly caused by the deterministic drift current. In the U-shaped conformation of figure 4.12(a) the filament experiences bending forces. When it relaxes, different parts of the filament interact hydrodynamically via flow fields initiated along the filament. These hydrodynamic interactions cause the center-of-mass to move away from the centerline. Increasing the rigidity of the filament also increases the bending forces which explains why the deterministic drift currents in figure 4.11 close to the centerline increase with L_P/L.

The shear induced hydrodynamic repulsion of a dumbbell from a wall has been treated in Refs. [45, 53, 54]. Similarly, close to the wall the shear flow stretches the filament and creates tensional forces which initiate flow fields as sketched in figure 2.5 on the left. They drive the filament away from the wall [see figure 4.12(b)]. These tensional forces do not depend on the filament's bending rigidity. Therefore, in figure 4.11 the deterministic drift currents close to the wall do not change with L_P/L.

4.5 Summary and conclusion I

In this chapter we treated a paradigmatic model for studying how the properties of a system change when it is driven out of equilibrium. Motivated by recent experiments [37], we analyzed a single semiflexible polymer confined between two planar walls and under the influence of an imposed Poiseuille flow with special emphasis on the observed cross-streamline migration. We performed Brownian dynamics simulations for a bead-spring chain with bending rigidity and used the two-wall Green tensor of the Stokes equations to take into account hydrodynamic interactions along the polymer and with the wall. We carefully analyzed how polymer conformations, center-of-mass distribution, and orientational order of

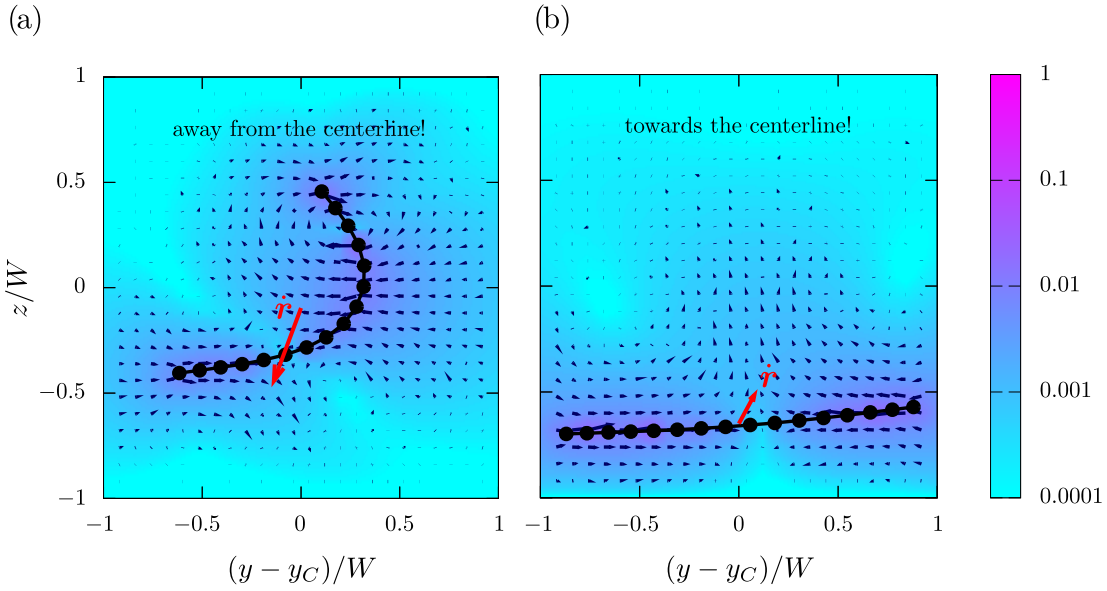

Figure 4.12: (a) At the centerline, the relaxing U-shaped filament initiates flow fields relative to the applied Poiseuille flow. The resulting hydrodynamic interactions drive the filament away from the centerline. The strength of the flow is given by the color code in arbitrary units. (b) Close to the wall the filament is under tension. This initiates flow fields illustrated in figure 2.5 on the left that drive the filament away from the wall.

the end-to-end vector within the channel depend on parameters such as the flow strength and the stiffness of the model polymer. Analytic expressions for hard needles at zero flow reproduce the simulation results and demonstrate how the behavior of the model polymer changes when the Poiseuille flow is turned on. Our results are in agreement with experiments [37] and simulations [38, 52] that employ a different, particle based method to simulate the viscous environment called multi-particle collision dynamics.

In particular, we observed the characteristic bimodal probability distribution for the polymer's center-of-mass and showed that hydrodynamic interactions along the model polymer and with the wall are essential for this distribution to occur, whereas shape and orientation of the filament are mainly determined by the applied Poiseuille flow. Based on a Smoluchowski equation for the center-of-mass probability distribution, we investigated cross-streamline migration and the origin of the bimodal distribution in detail. Whereas the migration away from the wall is due to hydrodynamic interactions with the bounding walls, in agreement with Refs. [37, 38, 52] and work on flexible polymers [44, 44, 45, 46, 47, 49, 50, 125, 126], we clearly identified a deterministic drift current as the major cause for migration

away from the centerline, especially when the bending stiffness of the model polymer increases. The current is set up when bent conformations of the polymer relax towards the straight filament. Diffusional currents due to a position-dependent diffusivity become completely irrelevant with increasing rigidity of the polymers. This demonstrates that bending rigidity leads to a clear difference in the behavior of flexible and semiflexible polymers in Poiseuille flow and in the explanation of the observed cross-streamline migration.

5

Nonlinear dynamics of spherical particles in confined Poiseuille flow

«The scientist does not study nature because it is useful to do so. He studies it because he takes pleasure in it, and he takes pleasure in it because it is beautiful.»

Henri Poincaré

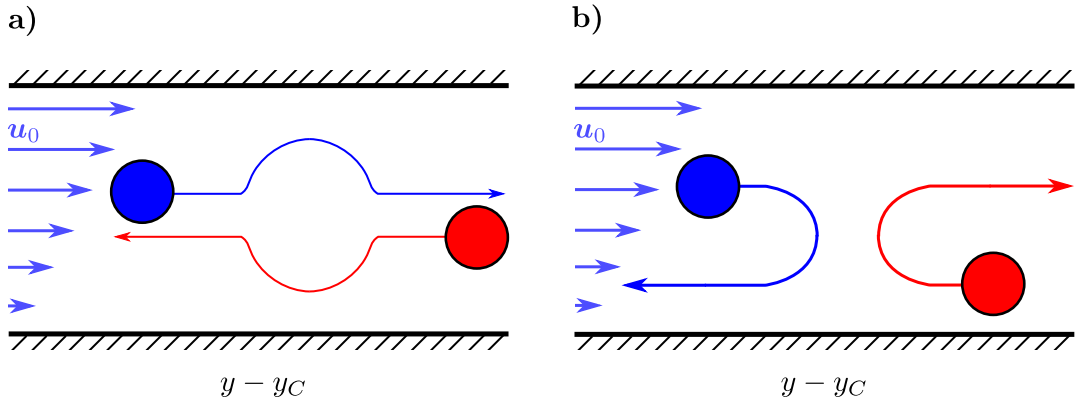

Figure 5.1: Systematic sketch of the classes of pair trajectories already observed in linear shear flow (displayed in the center-of-mass frame). (a) passing trajectory: two spheres pass each other and return to their initial lateral positions after the binary encounter is completed. (b) swapping trajectory: the spheres swap their lateral positions and leave in the same direction from where they came.

5.1 Introduction

An essential aspect for understanding microfluidic devices is the flow induced cross-streamline migration of suspended objects in confined geometries. Therefore, recent investigations have focused on the nonlinear dynamics in such geometries. For example, hydrodynamic coupling under confinement with and without imposed flow has been discussed close to a planar wall[32, 56, 133], close to a planar fluid-fluid interface [134], between two planar walls[55], or in a spherical cell [135]. From a fundamental point of view cross-streamline migration gives rise to interesting dynamical patterns in particulate flow. Examples are the bimodal density distribution in dilute polymer suspensions, as we discussed in chapter 4, characteristic phonon modes of one-dimensional microfluidic crystals in flat microchannels [27, 28, 29] or collective dynamics in two-dimensional arrays [30, 31, 32].

To gain a better understanding for the rheology of such suspensions of rigid particles, their relative motion is central. In 1972 Batchelor and Green [34] showed that two spheres pass each other in unbounded shear flow under creeping-flow condition and return to their initial lateral positions after a binary encounter is completed [34] [see figure 5.1(a)]. This behavior was also observed in experimental studies [19]. In addition, in bounded shear flow a different class of particle

trajectories was observed [35]. Here, wall proximity gives rise to swapping trajectories, where the particles do not pass each other but instead they swap their lateral positions and leave in the same direction from where they came [see figure 5.1(b)]. At non-zero Reynolds numbers these trajectories have also been observed in unconfined shear flow [136, 137, 138].

In this chapter we study the relative motion of two identical spherical colloids in a pressure driven Poiseuille flow. They are confined between two planar parallel walls, whose distance is comparable to the particle diameter. Several methods for evaluating hydrodynamic interactions between colloids, which are confined between two parallel walls, are used [139, 140, 141, 142, 143]. Here, we employ the grand mobility matrix which incorporates the multipole expansion of the hydrodynamic force densities acting on the particle surfaces and the lubrication correction which we introduced in chapter 2. The nonlinear dynamics of the particle pair in bounded Poiseuille flow gives rise to new classes of trajectories. Depending on their initial positions, the particles either move on oscillatory trajectories while staying bound together in the Poiseuille flow or they separate after an encounter. While the bound states have not been identified before, we also observe a new class of trajectories in the unbound state. In addition to the swapping trajectories, we find, what we call, cross-swapping trajectories. Finally, using results for the two-particle systems, we illustrate the stability of particle trains. This chapter is based on publication [B].

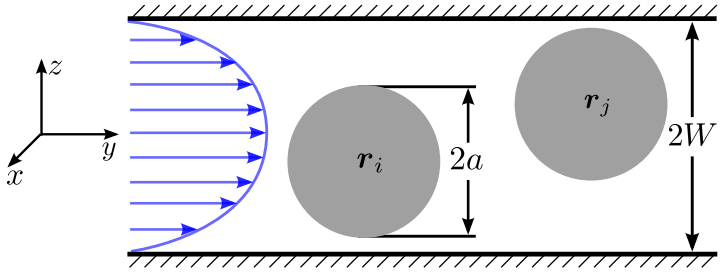

Figure 5.2: Force- and torque-free hard spheres, with radius a and positions $\boldsymbol{r}_i$, are confined between two parallel planar plates with distance $2W$. A Poiseuille flow is applied.

5.2 Modeling

In this section we describe how we treat hydrodynamic interactions between force- and torque-free spherical particles in Poiseuille flow by using the grand mobility matrix for particle configuration bounded by two parallel plates. We first define our system and then we summarize details of our Stokesian dynamics simulations.

5.2.1 System geometry

We consider the dynamics of, in general, N force- and torque-free hard spheres, each with radius a. They are confined between two parallel planar walls at positions $z = -W$ and $z = W$, which are infinitely extended in the $x - y$ plane (see figure 5.2). For simplicity, we assume that the particles only move in the $y - z$ plane at $x = 0$, which we set initially. Since there are no forces and torques acting on the particles and due to the translational symmetry along the x direction the spheres stay in that plane [55]. This reduces our computational efforts considerably. Between the walls a pressure driven Poiseuille flow is created

$$\boldsymbol{u}_0(\boldsymbol{r}) = v_0 \left[1 - \left(\frac{z}{W}\right)^2\right] \boldsymbol{e}_y \ , \tag{5.1}$$

where again v_0 denotes the maximum velocity at the centerline ($z = 0$), $\boldsymbol{e}_y$ is the unit vector along the y axis and W the distance between the centerline and the walls.

5.2.2 Equations of motion

As we already discussed in section 2.5, the translational and rotational velocities of N spherical colloids subject to external forces, torques, and an imposed Poiseuille flow are given by

$$\mathbf{v} = \mathbf{u}_0(\boldsymbol{x}) + \mathbf{m}(\boldsymbol{x})\mathbf{h}(\boldsymbol{x}) + \boldsymbol{\mu}(\boldsymbol{x})\mathbf{F}(\boldsymbol{x}), \tag{5.2}$$

where $\mathbf{v} = (\boldsymbol{v}, \boldsymbol{\omega})$ and $\mathbf{u}_0 = (\boldsymbol{u}_0, \boldsymbol{\omega}_0)$ denote the $6N$-dimensional generalized N-particle velocities, $\mathbf{F} = (\boldsymbol{F}, \boldsymbol{T})$ the generalized forces, $\mathbf{h} = (\boldsymbol{g}_0, \boldsymbol{h}_0^1, \boldsymbol{h}_0^2, \boldsymbol{h}_0^3)$ the higher order velocity multipole moments,

$$\boldsymbol{\mu} = \begin{pmatrix} \bar{\boldsymbol{\mu}}_L^{\mathrm{tt}} & \bar{\boldsymbol{\mu}}_L^{\mathrm{tr}} \\ \bar{\boldsymbol{\mu}}_L^{\mathrm{rt}} & \bar{\boldsymbol{\mu}}_L^{\mathrm{rr}} \end{pmatrix}, \tag{5.3}$$

the mobility matrix and

$$\mathbf{m} = \begin{pmatrix} \bar{\boldsymbol{\mu}}_L^{\mathrm{td}} & \bar{\boldsymbol{\mu}}_{L,1}^{\mathrm{th}} & \bar{\boldsymbol{\mu}}_{L,2}^{\mathrm{th}} & \bar{\boldsymbol{\mu}}_{L,3}^{\mathrm{th}} \\ \bar{\boldsymbol{\mu}}_L^{\mathrm{rd}} & \bar{\boldsymbol{\mu}}_{L,1}^{\mathrm{rh}} & \bar{\boldsymbol{\mu}}_{L,2}^{\mathrm{rh}} & \bar{\boldsymbol{\mu}}_{L,3}^{\mathrm{rh}} \end{pmatrix}. \tag{5.4}$$

the matrix containing the other elements of the grand mobility matrix. The elements $\bar{\boldsymbol{\mu}}_L^{\mathrm{ab}}$ of the grand mobility matrix (2.91) are obtained by a multipole expansion, truncated after the multipolar order L and supplemented by a lubrication correction, as discussed in detail in section 2.5. Since in our case the particles are force- and torque-free ($\boldsymbol{F} = \boldsymbol{T} = \mathbf{0}$), the equation of motion (5.2) simplifies to

$$\mathbf{v} = \mathbf{u}_0(\boldsymbol{x}) + \mathbf{m}(\boldsymbol{x})\mathbf{h}(\boldsymbol{x}), \tag{5.5}$$

which is the basis for our Stokesian dynamics simulation.

5.2.3 System parameters

In order to determine the matrices $M_L(ilm\sigma, jl'm'\sigma)$ and $Z_L(ilm\sigma, jl'm'\sigma')$ (see section 2.5.3), we closely followed the implementation described in Ref. [55], where one particle in Poiseuille flow is treated, and generalized it to N particles by appropriate modifications (see Appendix A). Since the evaluation of $M_L(ilm\sigma, jl'm'\sigma)$ at each time step is very time consuming, we defined in the microchannel a grid with 160×25 grid points and a mesh size of $0.05W$. Then, we stored the values of $M_L(ilm\sigma, jl'm'\sigma)$ on the grid for different configurations $\boldsymbol{r}_i$ and $\boldsymbol{r}_j$, which we define by the axial distance and the two lateral positions of the two particles i, j. Matrix values at intermediate locations on the grid are determined from the grid points by linear interpolation. Matrices and vectors are truncated after the multipolar order $L = 5$.

After transforming to real basis functions and applying the lubrication correction, which we described in section 2.5.4, we obtain the grand mobility matrix (2.91). According to equation (5.5) we compute the angular and translational velocities for a given particle configuration $\boldsymbol{x} = (\boldsymbol{r}_1, \ldots, \boldsymbol{r}_N)$ and, then, update the configuration with a small timestep $\Delta t = 2 \times 10^{-3}$ in units of W/v_0 (see section 2.6.2).

5.3 Results

We first investigate the translational and angular velocity of one suspended particle and compare our results with these of Staben *et al.* [144]. Then we investigate the nonlinear dynamics of a system of two equal-sized particles and, finally, we use our findings to interpret the dynamics of a linear array of colloids.

5.3.1 Translational and angular velocity of a sphere

As we already discussed in section 4.1, at low Reynolds numbers close to zero, single spherical particles just follow the streamlines in a laminar flow as a result of the kinematic reversibility of the Stokes equations. In this section we analyze the translational and angular velocity of one spherical particle with radius $a/W = 0.6$.

Figure 5.3 shows the translational velocity along the y-direction v_y of the sphere at different lateral positions z. For a spherical particle suspended in a Poiseuille flow without bounding walls, the translational velocity is simply given by Faxén's law ($\boldsymbol{F} = \boldsymbol{0}$) (see section 2.3.3)

$$\boldsymbol{v} = \mathcal{L}^{\mathrm{t}} \boldsymbol{u}_0(\boldsymbol{r}) \quad \text{with} \quad \mathcal{L}^{\mathrm{t}} = \mathbf{1} + \frac{a^2}{6}\nabla^2. \tag{5.6}$$

At the centerline ($z = 0$), the velocity of the unconfined particle is nearly identical to the translational velocity of a particle suspended in a confined Poiseuille flow (see figure 5.3). But due to the interaction with the bounding walls, the velocity of the confined particle decreases more towards the walls. We observe, that truncating the multipole expansion after the multipolar order $L = 5$ and applying the lubrication correction, the results are in a very good agreement to those of Staben *et al.* [144].

Figure 5.4 shows the angular velocity of the sphere. Without bounding walls, the velocity grows linear with z, which one can easily verify by inserting (5.1) into Faxén's law for the rotational motion (2.47). In the presence of the walls the angular velocity increases monotonically with z until it reaches a maximum, then the velocity decreases towards the walls due to the hydrodynamic interaction with the walls.

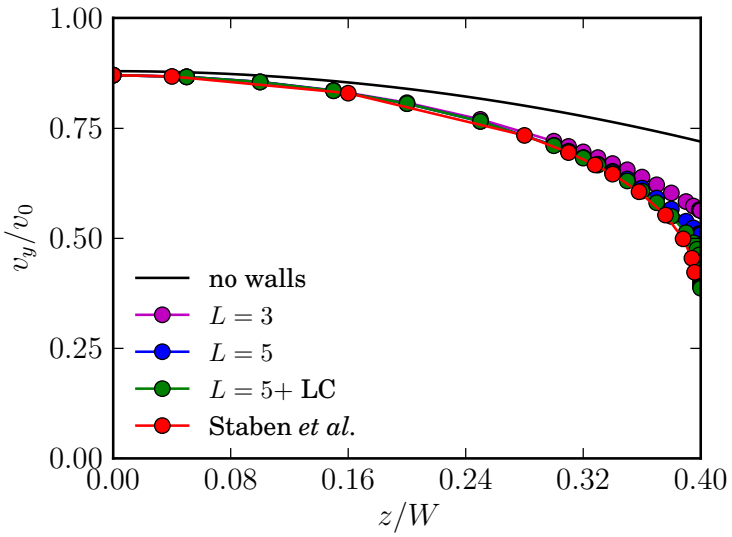

Figure 5.3: Translational velocity along the y-direction at different lateral positions z of the sphere. Our results for the multipolar orders $L = 3$ and $L = 5$ (with and without lubrication correction [LC]), are compared to those of Staben *et al.* [144] and for a particle in Poiseuille flow without bounding walls.

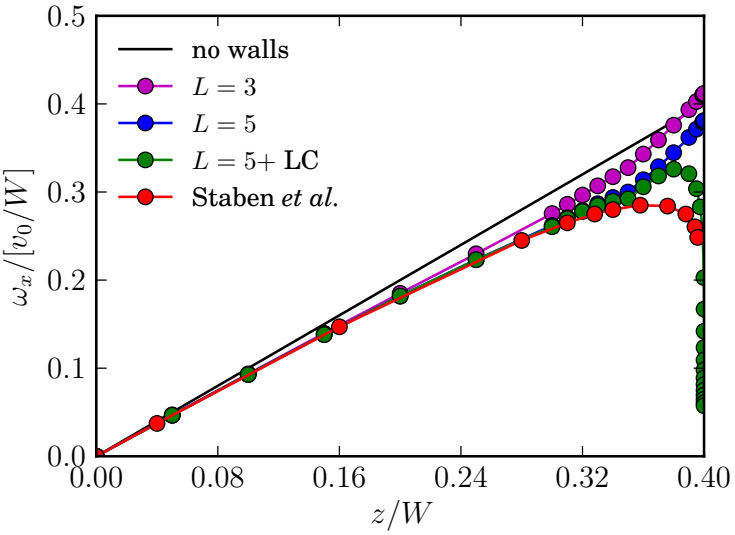

Figure 5.4: Angular velocity at different lateral positions z of the sphere. The results are shown for the multipolar orders $L = 3$ and $L = 5$ (with and without lubrication correction), for a sphere in unbounded Poiseuille flow and from Ref. [144].

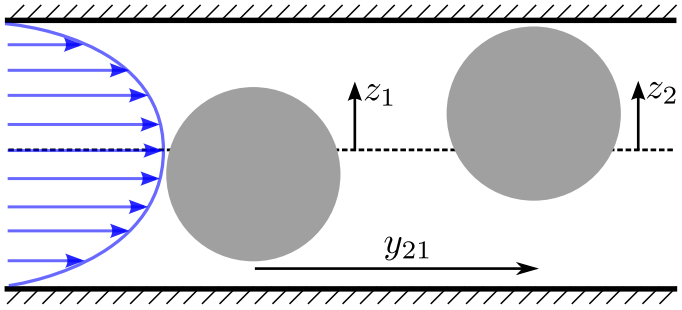

Figure 5.5: Two identical spherical colloids with an initial axial distance $y_{21} = y_2 - y_1$ and initial lateral positions z_1 and z_2.

5.3.2 Relative motion of two identical spherical colloids

We analyze the dynamics of two identical spherical colloids for different initial conditions, namely the axial distance y_{21} and the lateral positions z_1 and z_2, as indicated in figure 5.5. We always assume that the leading sphere 2 initially moves slower than the trailing sphere meaning $|z_1| < |z_2|$. So there will always be a binary encounter of the two colloids. Then, the other case, $|z_1| > |z_2|$, always belongs to trajectories after a binary encounter, as can be directly understood from the kinematic reversibility of the Stokes equations.

5.3.2.1 Unbound and oscillatory bound states

In the case that the two particles cannot pass each other ($2a/W > 1$), we identify different types of trajectories. They are illustrated for $a/W = 0.6$ in figure 5.6 in the center-of-mass frame. Depending on the initial separation (but also the initial lateral positions), we observe two states of particle motion, an unbound state and an oscillatory bound state. In the unbound state the spheres approach each other, turn around, and separate [see figure 5.6 (a) and (b)]. They move either on swapping trajectories (ST) or cross-swapping trajectories (CS). In 1972, Batchelor and Green showed that binary encounters between two spherical particles in unbounded shear flow lead to passing trajectories, where each particle returns to its initial lateral position after a binary encounter is completed [34]. The swapping trajectories were first observed by Zurita-Gotor *et al.* for a pair of spherical colloids in confined shear flow [35]. Here the particles migrate across the streamlines such that they exchange their lateral coordinates at the end of the binary encounter [see figure 5.6(a)]. Hence, such particle collisions displace the spheres across the streamline of the external flow. In addition to this type of trajectories, we also observe particles moving on cross-swapping trajectories [see

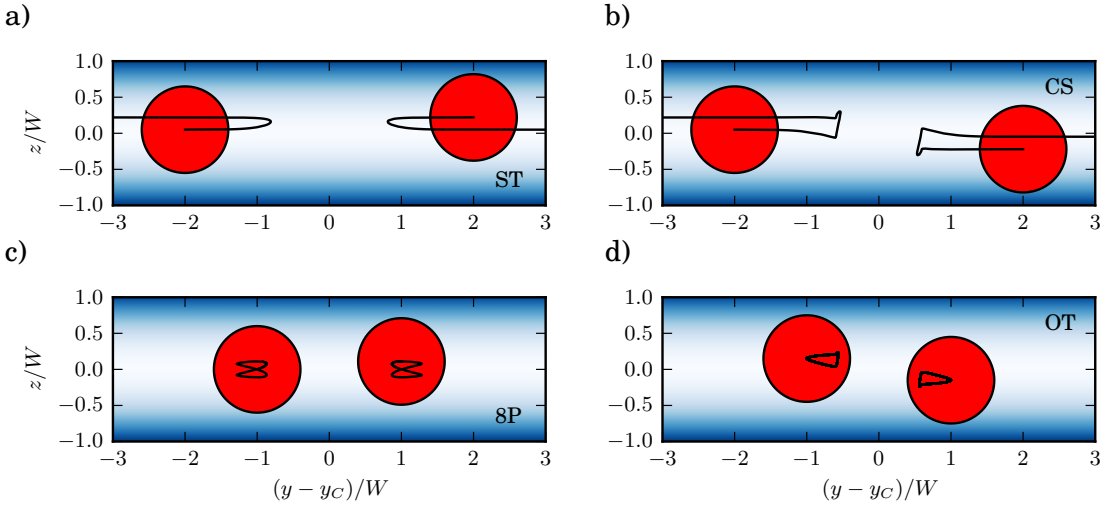

Figure 5.6: Trajectories for different initial conditions plotted in the center-of-mass frame. In the unbound state the spheres move on either (a) swapping trajectories (ST) or (b) cross-swapping trajectories (CS). In the bound state they move on trajectories (c) forming the pattern of an eight (8P) or (d) with an oval shape (OT).)

figure 5.6(b)]. In contrast to swapping motion, the colloids approach closer to each other and they exchange their lateral positions crosswise meaning

$$z_1' = -z_2 \text{ and } z_2' = -z_1, \tag{5.7}$$

where z_1', z_2' are the lateral positions after the binary encounter.

In addition to these unbound trajectories, where the particles separate at long times, we can also observe oscillatory bound states when the initial axial distance y_{21} is decreased. Here the particles oscillate on their trajectories while staying together in the Poiseuille flow [see figure 5.6 (c) and (d)]. The spheres move on trajectories either forming the pattern of an eight (8P) or with an oval shape (OT) when viewed in the center-of-mass frame. Figure 5.7 shows state diagrams for particle trajectories when the initial axial distance y_{21} is fixed. We varied the the initial lateral positions z_1 and z_2 and determined the type of particle trajectories as discussed in figure 5.6. The frequencies of the oscillatory bound states are color-coded and show interesting structural features. The region of bound states concentrates around the diagonal $z_2 = -z_1$. For an initial axial distance of $y_{21}/W = 1.3$, where the spheres with radius $a/W = 0.6$ are nearly touching, we observe a wide region of oscillatory bound states [see figure 5.7(a)]. The oscillatory state of type 8P occurs around $z_1 \approx 0$ and $z_2 \approx 0$ with smaller oscillation

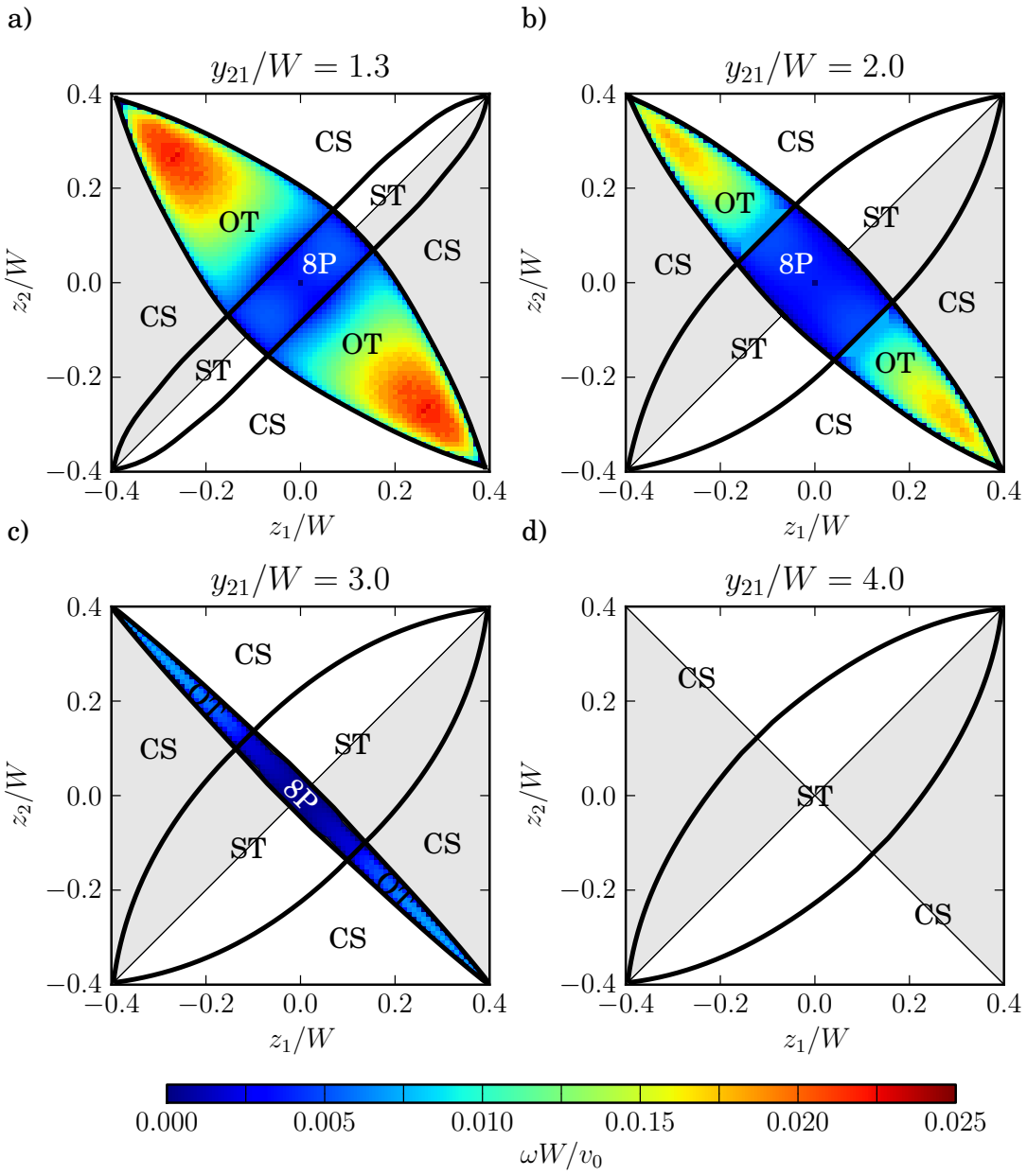

Figure 5.7: State diagram for the different types of trajectories of a two-particle system. It is plotted when the initial lateral positions z_1 and z_2 are varied, while the initial axial distance y_{21} is fixed. The particle radius is $a/W = 0.6$. a) $y_{21}/W = 1.3$, b) $y_{21}/W = 2.0$, c) $y_{21}/W = 3.0$, and d) $y_{21}/W = 4.0$. The frequencies ω of the oscillatory states [oval trajectory (OT) and pattern of eight (8P)] are color-coded. Outside the colored region, unbound states with swapping- (ST) or cross-swapping (CS) trajectories occur. The trajectories in the gray shaded areas show binary encounters of either ST or CS type when they are traced back into the past.

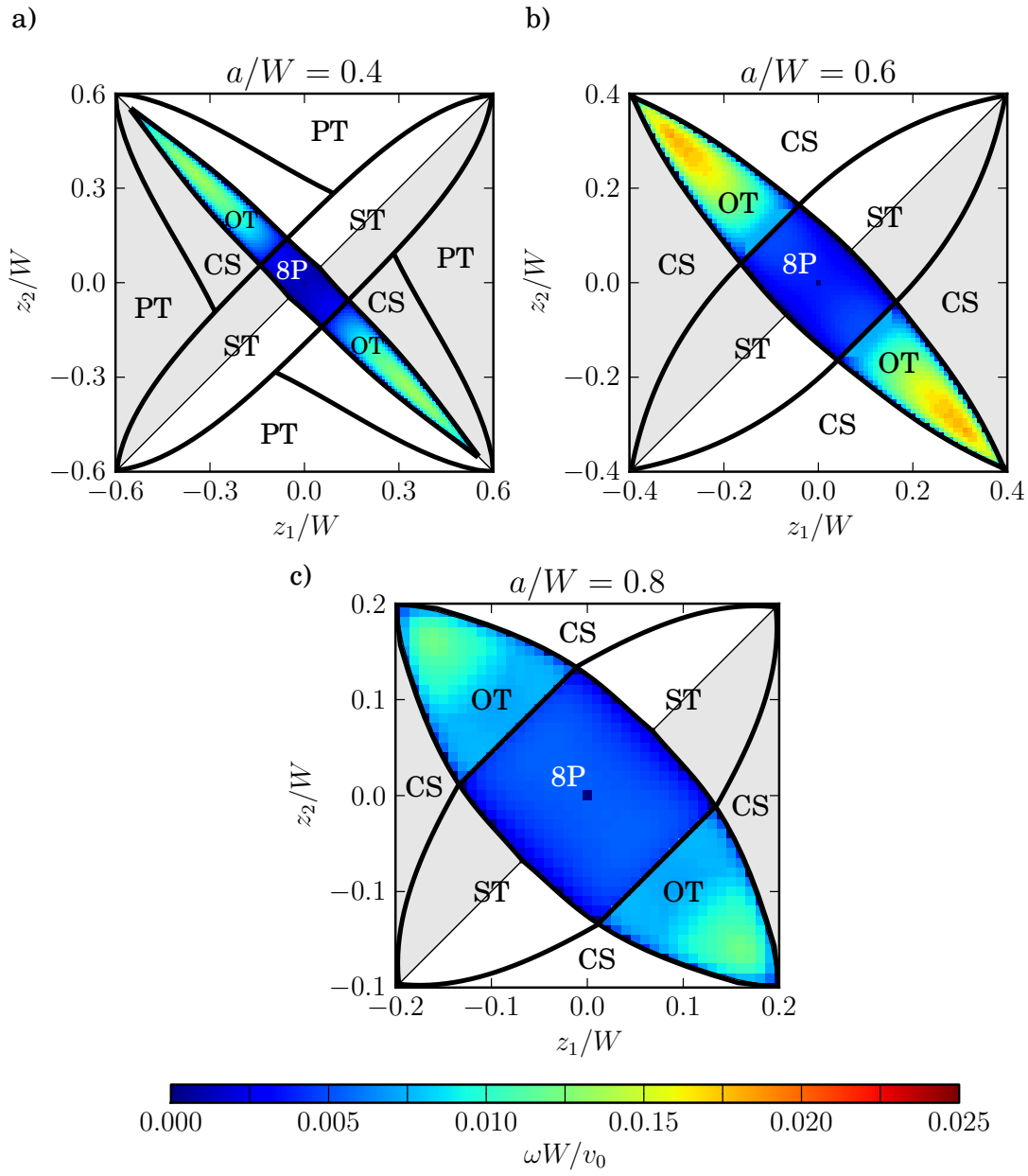

Figure 5.8: State diagrams in z_1, z_2 for an initial axial distance $y_{21}/W = 2.0$ and different particle sizes: a) $a/W = 0.4$, b) $a/W = 0.6$, and c) $a/W = 0.8$.

frequencies than in the OT type. For initial lateral coordinates outside this region, the particles exhibit the unbound state. They either move on swapping trajectories for initial coordinates situated around the diagonal $z_2 = z_1$ or cross-

swapping trajectories. In the gray areas the leading particle 2 in the Poiseuille flow has a larger velocity and a binary encounter and thus particle swapping does not occur. However, tracing the particles into the past, the respective swapping or cross-swapping trajectories are observed. This is clear either from the kinematic reversibility of the Stokes equations or when the direction of the Poiseuille flow is reversed. Then the leading particle 2 becomes the trailing sphere. The boundary between white and gray areas are the diagonals $z_2 = z_1$ and $z_2 = -z_1$. Interestingly, the region of bound 8P trajectories results from intersecting the region with oscillatory motion and the region with swapping trajectories. This makes sense since in the 8P trajectories as well as in the swapping trajectories both particles cover the same z region.

Now, when we increase the initial lateral distance y_{21} of the particles [see figure 5.7 (a)-(d)], the region of bound oscillatory states becomes narrower and the frequencies decrease until ultimately the bound states vanish completely. Obviously, the hydrodynamic coupling between the two particles is no longer strong enough to hold them together. Simultaneously, we also observe that the region of swapping trajectories expands with increasing y_{21}.

5.3.2.2 Dependence on particle size

So far we analyzed particle trajectories at a fixed radius of $a/W = 0.6$ of the two spheres. Figure 5.8 shows state diagrams in z_1, z_2 for different particle sizes at an initial axial distance of $y_{21}/W = 2$. Small particles ($a/W = 0.4$) can pass each other and in the state diagram of figure 5.8(a) we indeed observe passing trajectories (PT) in addition to the trajectories reported so far.

Such passing trajectories were first observed in unbounded [34] and then bounded [35] shear flow. The particles pass each other during approach, separate again, and return to their initial cross-streamline positions. In figure 5.9 we show several particle trajectories. Particle 1 starts at $z_1/W = 0.05$ while the lateral position z_2 of particle 2 is gradually decreased so that the transition from passing to cross-swapping trajectories takes place. In contrast to the trajectories in linear shear-flow [35], the trajectories of both particles are not symmetric since the shear rate in Poiseuille flow varies across the streamlines. In the passing trajectories the trailing sphere 1 has a larger velocity than the leading sphere 2. The transition to cross-swapping takes place when during approach the trailing sphere migrates to a position with smaller flow velocity than the leading sphere, $v_{0y}(z_1) < v_{0y}(z_2)$, as indicated in figure 5.9. As a consequence, the particles separate before the passing trajectories can be completed and they move on cross-swapping trajectories. This behavior is a feature of the Poiseuille flow and cannot be observed in linear shear flow.

For larger particle sizes the passing trajectories vanish and the oscillatory

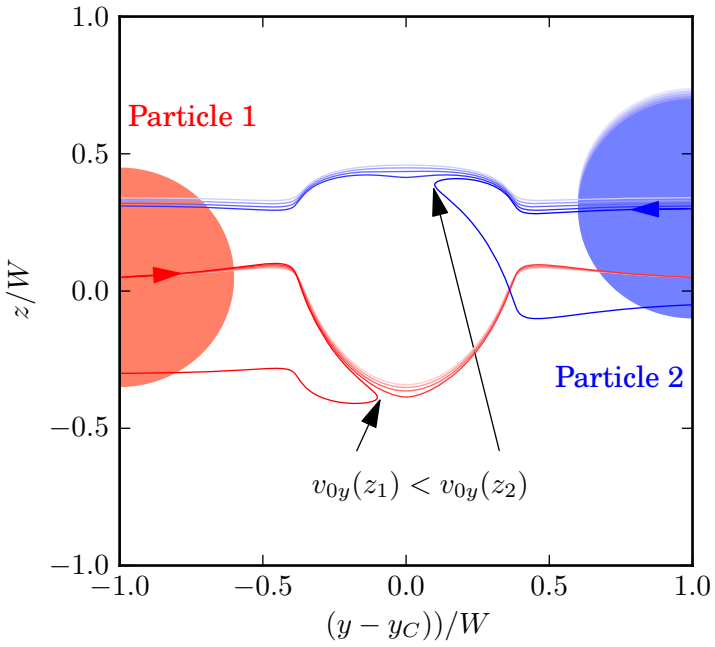

Figure 5.9: Passing trajectories of two identical spheres with radius $a/W = 0.4$ turn into cross-swapping trajectories (plotted in the center-of-mass frame): sphere 1 starts at a lateral position of $z_1/W = 0.005$ while the lateral coordinate z_2 of sphere 2 is gradually decreased. The transition to cross-swapping occurs when $v_{0y}(z_1) < v_{0y}(z_2)$.

state occupies a larger area in the accessible region of the z_1, z_2 state diagram, as figure 5.8 (b) and (c) demonstrate. So, when the confinement becomes stronger, the oscillatory bound state becomes more important. In figure 5.10 we plot the oscillation frequencies in the bound state against the particle radius a for different initial axial distances y_{21}. In plot a) we fix the initial lateral positions to $z_1/W = 0.1$ and $z_2/W = 0$. Small spheres then lie outside the narrow region of the bound states [see figure 5.8(a)] and do not oscillate ($\omega = 0$). When the particles size increases, this region expands and at a critical radius $a_{crit.}$ the particle system enters the regime of the oscillating 8P trajectories. The oscillation frequency increases from zero with increasing a. Larger initial distances y_{21} reduce the hydrodynamic coupling. Therefore the spheres have to be larger to initiate the bound state and the frequency is smaller. Increasing the particle separation even further, would require particle radii $a/W > 1$. Since this cannot be, oscillatory states do not occur anymore.

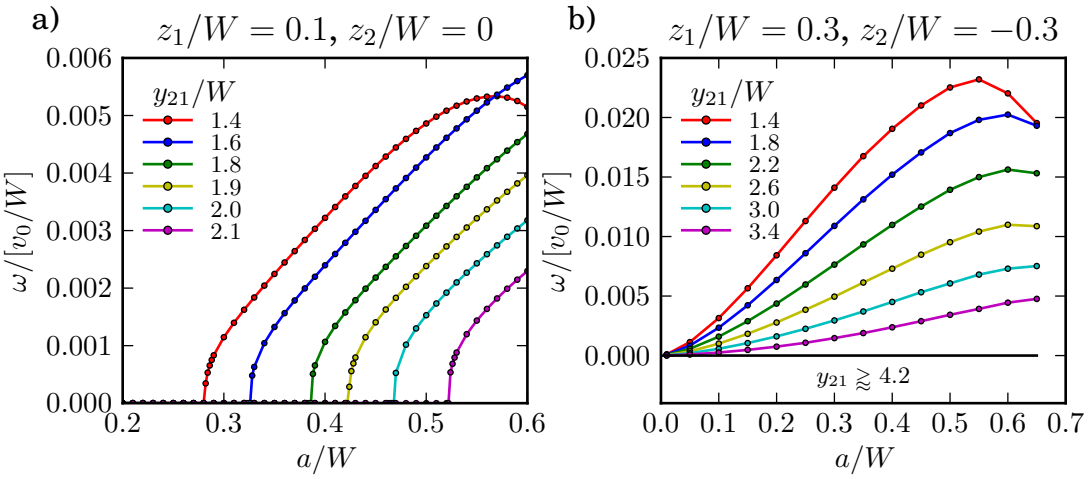

Figure 5.10: Oscillation frequency ω in the bound states plotted versus particle radius a for different initial axial distances y_{21}. The lateral coordinates are set to a) $z_1/W = 0$, $z_2/W = 0.1$ and b) $z_1/W = 0.3$, $z_2/W = -0.3$.

In figure 5.10(b) we choose initial lateral coordinates $z_1/W = 0.3$ and $z_2/W = -0.3$. They lie on the diagonal in our z_1, z_2 state diagrams where the spheres move on oscillatory trajectories of type OT. Obviously, decreasing the particle radius to zero at fixed y_{21}, the width of the oscillatory region goes to zero. This explains that the oscillation frequency also continuously approaches zero with a. With increasing axial distance y_{21}, the whole curve rises less and there is a limiting axial distance $y_{21} \approx 4.2$ where the bound state vanishes completely.

5.3.3 Linear array of particles

Particles in bound states do not pass each other and do no separate as they do when moving on passing, swapping, or cross-swapping trajectories. This may have significant consequences for microfluidic systems, where precise manipulation of linear arrays of, e.g, nearly aligned particles is very important [8, 145] The bound two-particle states now suggest that particles in such particle trains do not aggregate when they move with slightly different velocities on different streamlines. Instead, they stay separated while moving on oscillatory trajectories. To investigate this question, we implemented linear arrays of particles as shown in Figs. 5.11 and 5.12 using approximate periodic boundary conditions. We extend the particle train to the right and to the left by a respective group of three particles which we copy to the other side of the microchannel after each time step in our simulations. In Figs. 5.11 and 5.12 we illustrate the dynamics

of the particle trains.

In figure 5.11(a) we first investigate a particle train where the particles of radii $a/W = 0.6$ are approximately arranged along the centerline. Each sphere starts with a small random lateral offset $\Delta z_i/W \in [-0.05, 0.05]$ relative to the centerline at $z = 0$ which may mimic experimental conditions. In addition, the initial axial distance between two neighboring particles is set to $y_{i+1,i}/W = 1.6$ to ensure that they belong to the two-particle oscillatory bound state of type 8P. Indeed, the snapshots in figure 5.11(a) show that the particle train is stable. Between the snapshots the particles travel several times through the simulated piece of microchannel. The particles do not aggregate and each particle moves on an approximately oscillatory trajectory. It oscillates around the centerline as illustrated at the bottom of figure 5.11(a), where we plot the z coordinate of the blue particle versus time. It also oscillates between its two neighbors as the y coordinate relative to the center-of-mass coordinate y_C shows but with a much smaller frequency compared to the lateral direction. A closer inspection reveals slightly irregular oscillations which we attribute to the two neighboring particles. In total, these oscillations demonstrate that the particle train does not disintegrate.

In figure 5.11(b) we illustrate the dynamics of a particle train when we initially arrange the spheres in a zig-zag pattern. The lateral positions of neighboring particles approximately fulfill $z_{i+1} = -z_i$ to which we also add a small random offset $\Delta z_i/W \in [-0.05, 0.05]$. Together with the initial axial distance of two neighboring particles, $y_{i+1,i}/W = 1.6$, we expect that each particle moves on a trajectory of type OT as in the two-particle bound state. Indeed, the snapshots again reveal a stable particle train. The lateral and relative axial displacements are less regular than in a). However, they are both bound so that each particle in the center-of-mass frame moves on a restricted area similar to the two-particle trajectories of type OT. As soon as we disturb the regular particle trains too much, they are no longer stable. We show this in figure 5.12 for the two cases of the linear (a) and the zig-zag (b) pattern. The blue particle starts with a sufficiently large vertical offset so that with one of its neighbors it belongs to a two-particle unbound state. Hence, all the particles no longer perform oscillatory trajectories. They approach each other and migrate across streamlines until they arrange in a zig-zag order. Here they constantly form transient clusters which then dissolve in time at the downstream end of the cluster. The completely irregular particle motion also becomes clear from the lateral position and the relative axial displacement of the blue particle plotted versus time at the bottom of Figs. 5.12a) and b).

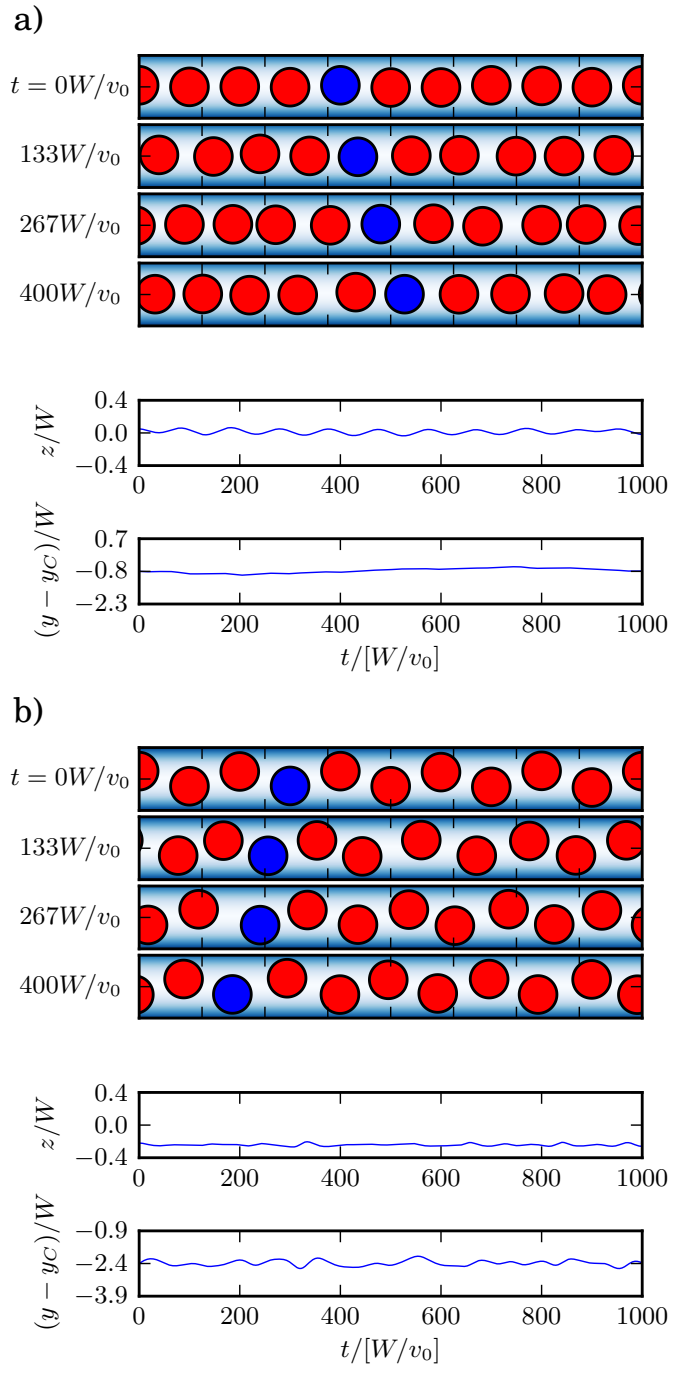

Figure 5.11: Snapshots of a linear array of particles with radius $a/W = 0.6$ at different times t. In addition, the lateral coordinate z and the relative axial displacement $y - y_C$ in the center-of-mass frame is plotted versus time for the blue colored particle. a) Initially, the spheres are placed close to the centerline with a small random offset Δz_i relative to $z = 0$. b) Initially, the spheres are arranged in a zig-zag pattern, where the particles have a small random offset Δz_i relative to $z_{j+1} = -z_j = \pm 0.25W$.

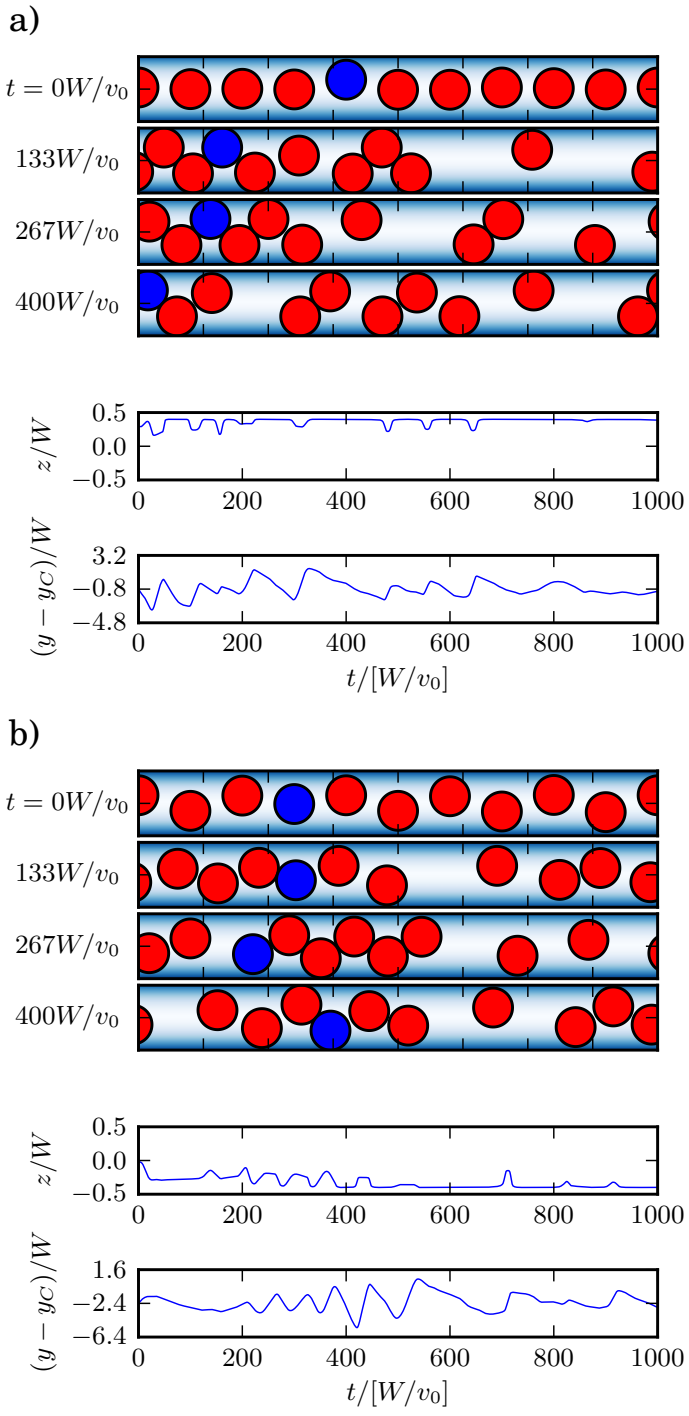

Figure 5.12: Same setting as in figure 5.11. Now the offset of the blue colored particle is larger so that neighboring particles belong to the unbound state.

5.4 Summary and conclusion II

We identified and analyzed the different classes of trajectories for two identical spherical colloids subject to Poiseuille flow under creeping-flow condition. The distance of the bounding walls was comparable to the particle diameter. In addition, we investigated the stability of particle trains. To treat hydrodynamic interactions between the particles, we determined the grand mobility matrix (2.91) using a multipole expansion for the hydrodynamic force densities induced on the particle surfaces. To be sufficiently accurate, we included multipoles up to the fifth order and applied a lubrication correction to the friction matrix.

Two identical particles move either in an unbound or an oscillatory bound state depending on their initial separation and lateral positions in the microchannel. In the unbound state the spheres follow swapping-, cross-swapping or even passing trajectories when the particles are sufficiently small. Whereas the passing and swapping trajectories were already observed in bounded linear shear flow [35], the cross-swapping trajectories are a distinct feature of the bounded Poiseuille flow. Here, the particles move first on passing trajectories until the trailing sphere migrates to a lateral position with lower velocity compared to the leading particle. As a consequence, the particles separate before they can pass each other. For initial small axial distances y_{21} even bound states exist which do not occur in linear shear flow. Here, the particles follow oscillatory trajectories while staying together in the Poiseuille flow. Depending on the initial lateral positions, they move on trajectories tracing either an eight or an oval shape. To categorize the different states of motion, we provided state diagrams in the lateral positions for different initial axial distances and also analyzed how the diagrams changed with the particle radii. In addition, we determined the oscillation frequencies in the bound states.

Particles moving on bound oscillatory trajectories do not separate which may have significant consequences for microfluidic systems. The bound two-particles states can explain why particle trains that either are nearly straight or have a zig-zag pattern are stable. Defects in these ordered particle trains correspond to particles with distinctly different flow velocities so that the particle trains become unstable. They disintegrate and aggregate to transient clusters. Thus, a proper understanding of the migration pattern in the two-particle bound state may contribute towards finding better methods of controlling particle motion in microfluidic devices.

6 Conclusions

«In science one tries to tell people, in such a way as to be understood by everyone, something that no one ever knew before. But in the case of poetry, it's the exact opposite!»

Paul Adrien Maurice Dirac

The aim of this work was to explore the potential of hydrodynamic interactions to induce novel motional patterns in confined flow, which then provides a deeper understanding for relevant physical and biological processes, such as the cross streamline migration of semiflexible polymers [37] or the collective dynamics of dense particle arrays [31].

We started by introducing the theoretical framework of this work. In chapter 2, we presented the hydrodynamic equations, which are the basis to describe the hydrodynamic interactions of suspended particles. Then we presented concepts to describe these interactions between spherical particles suspended in an unbounded fluid as well as in a bounded fluid under the influence of a pressure driven Poiseuille flow. In chapter 3, we introduced the basic concept of Brownian motion. First we presented the Langevin equation, a stochastic differential equation describing the time evolution of the suspended particles. Then we introduced an equivalent approach to consider the probability distribution of the particles, which is given by the Smoluchowski equation.

In chapter 4, we investigated the dynamics of a bead-spring chain confined between two parallel walls under the influence of a pressure driven Poiseuille flow. The hydrodynamic interactions between the point-like beads of the model polymer were taken into account by the two-wall Green tensor of the Stokes equations [55]. Performing Brownian dynamics simulations, we showed that the characteristic bimodal probability distribution for the polymer's center of mass is governed by the hydrodynamic interactions along the bead-spring chain and with the bounding walls. Without these interactions, the center of mass is distributed homogeneously across the channel. In addition, we presented numerical results on the orientational order of the end-to-end vector of the model polymer together with analytical hard-needle expressions at zero flow velocity. To gain a better understanding of the migration mechanism of the polymer, we derived a Smoluchowski equation for the center-of-mass distribution and carefully analyzed the different contributions to the probability current. In contrast to Refs. [37, 38, 52], where the migration away from the centerline was explained by a position-dependent diffusivity, we clearly identified a deterministic drift current as the major cause for migration away from the centerline. We even showed that diffusional currents due to a position-dependent diffusivity became less important with increasing polymer stiffness.

Therefore, with our results, we provide a full understanding of the migration mechanism of semiflexible polymers in confining geometries. In particular, we clarified how the polymers migrate away from the centerline. Thereby we are now able to describe the observed bimodal concentration profiles completely.

In chapter 5 we investigated the relative motion of a pair of force and torque-free spherical particles in Poiseuille flow. Since the particle's diameter was comparable to the channel width, we could no longer work with the simplified point

particles but had to take into account their finite extent. We determined the grand mobility matrix using a multipole expansion of the force densities on the spheres supplemented by a lubrication correction. Performing Stokesian dynamics simulations, we showed, that the bounded Poiseuille flow gives rise to new classes of trajectories resulting in cross-streamline migration of the two spheres. Particles moving on these new trajectories exhibited either bound or unbound states. In the unbound state the spheres followed swapping-, cross-swapping or even passing trajectories. Whereas the passing and swapping trajectories were already observed in bounded linear shear flow [35], the cross-swapping trajectories are a distinct feature of the bounded Poiseuille flow. Here, the particles moved first on passing trajectories until the trailing sphere migrated to a lateral position with lower velocity compared to the leading particle. As a consequence, the particles separated before they can pass each other. In the bound state, which do not occur in linear shear flow, the particles followed oscillatory trajectories while staying together in the Poiseuille flow. Depending on the initial lateral positions, they moved on trajectories tracing either an eight or an oval shape.

We analyzed the different classes of trajectories depending on the initial positions of the two particles and their size, and presented state diagrams, where we categorized the trajectories and color coded the oscillation frequencies of the bound states. Finally, we discussed how the results on the two-particle system help to understand the stability of particle trains composed of several particles.

With help of our results we offer a deeper understanding of the cross-streamline migration of colloidal particles in confined geometries under the influence of a Poiseuille flow. This can have potential consequences for microfluidic devices. For example, we showed that the center-of-mass distribution of semiflexible polymers strongly depend on the stiffness of the filament, which may offer potential applications in separation of different species of biopolymers. We also understood the stability of linear particle trains, which is important for microfluidic systems, where a precise manipulation of linear arrays of particles is necessary.

A possible extension of this work is to include external forces and torques in our system. For example, one can think to add permanent dipole moments to the colloids and use an electric or magnetic field to control their directions. As a possible next step, it would be interesting to investigate the dynamics of suspensions of different species (e.g. different in size) under confined flow. Also, a very challenging task would be to change the system geometry, which may be realized by fixed colloids. For example, one could add spherical obstacles inside the channel or simulate a constriction of the channel by a linear array of fixed particles.

To summarize: We investigated the nonlinear dynamics in two different col-

loidal model systems where the particles are confined between two planar walls and driven out of equilibrium by an imposed Poiseuille flow. We showed, that the bounded Poiseuille flow gives rise to interesting dynamic pattern formations.

On the one hand, our results reproduced the characteristic bimodal distribution of the the center of mass of a semiflexible polymer. For the first time, we were able to identify the mechanism for the migration away from the centerline. Therefore, our results provides a full understanding of the migration mechanism of semiflexible polymers in confining geometries, which may offer potential applications in separation of biopolymers.

On the other hand, we showed that the bounded Poiseuille flow gives rise to new and interesting classes of trajectories for a pair of force and torque-free particles. With the help of our results, we were able to understand the stability of particle trains composed of several particles, which may have significant consequences for microfluidic systems, where precise manipulation of linear arrays of particles is very important.

A

Appendix

In order to determine the matrices $M_L(ilm\sigma, jl'm'\sigma)$ and $Z_L(ilm\sigma, jl'm'\sigma')$ (see section 2.5.3), we closely follow the implementation described in Ref. [55], where one particle in Poiseuille flow is treated, and generalize it to N particles by appropriate modifications.

In section 2.5.1 we showed that the two-wall Green tensor splits up into the Oseen tensor and a reflectional part. The reflectional part is given by

$$\boldsymbol{T}^{\mathrm{R}}(\boldsymbol{r}, \boldsymbol{r}') = \int e^{i\boldsymbol{q}\cdot\boldsymbol{s}} \hat{\boldsymbol{T}}^{\mathrm{R}}(\boldsymbol{q}, z, z') e^{-i\boldsymbol{q}\cdot\boldsymbol{s}'} \mathrm{d}^2 q \ , \tag{A.1}$$

where $\boldsymbol{s} = (x, y)$ and $\boldsymbol{s}' = (x', y')$ are the two dimensional space vectors and $\boldsymbol{q} = (q_x, q_y)$ is the wave vector. In Fourier space, the reflectional part reads

$$\begin{aligned} \hat{\boldsymbol{T}}^{\mathrm{R}}(\boldsymbol{q}, z, z') &= \frac{1}{16\pi\eta q} \left[t_{1nn} \boldsymbol{e}_z \boldsymbol{e}_z + i t_{1np} \boldsymbol{e}_z \hat{\boldsymbol{q}} + i t_{1pn} \hat{\boldsymbol{q}} \boldsymbol{e}_z \right. \\ &\quad \left. - t_{1pp} \hat{\boldsymbol{q}} \hat{\boldsymbol{q}} + r_{1pp} (\mathbf{1} - \boldsymbol{e}_z \boldsymbol{e}_z) \right], \end{aligned} \tag{A.2}$$

where the scalar functions are given by

$$\begin{aligned} t_{1..} &= t_{1..}(\boldsymbol{q}, z, \bar{z}) = \mathcal{F}(w)^{\mathrm{T}} \mathcal{E}_{..}(u) \mathcal{F}(v), \\ r_{1pp} &= r_{1pp}(\boldsymbol{q}, z, \bar{z}) = \mathcal{F}(w)^{\mathrm{T}} \mathcal{G}_{pp}(u) \mathcal{F}(v). \end{aligned} \tag{A.3}$$

Here, we have introduced the scalars $u = qW$, $v = qz'$ and $w = qz$, the vector $\mathcal{F}(v) = (f_1(v), f_2(v), f_3(v), f_4(v)) = (\cosh v, \sinh v, v\cosh v, v\sinh v)$ and the

matrices

$$
\begin{aligned}
\mathcal{E}_{pp}(u) &= \begin{pmatrix} E_-C_- - 2u\tanh uE_- & 0 & 0 & -E_-A_- \\ 0 & E_+D_- - 2u\coth uE_+ & -E_+B_- & 0 \\ 0 & -E_+B_- & E_+ & 0 \\ -E_-A_- & 0 & 0 & E_- \end{pmatrix} , \\
\mathcal{G}_{pp}(u) &= \begin{pmatrix} -\frac{2e^{-u}}{\cosh u} & 0 & 0 & 0 \\ 0 & -\frac{2e^{-u}}{\sinh u} & 0 & 0 \\ 0 & 0 & 0 & 0 \\ 0 & 0 & 0 & 0 \end{pmatrix} , \\
\mathcal{E}_{nn}(u) &= \begin{pmatrix} -E_+C_+ & 0 & 0 & E_+A_+ \\ 0 & -E_-D_+ & E_-B_+ & 0 \\ 0 & E_-B_+ & -E_- & 0 \\ E_+A_+ & 0 & 0 & -E_+ \end{pmatrix} , \\
\mathcal{E}_{np}(u) &= \begin{pmatrix} 0 & u^2E_+ & -E_+A_+ & 0 \\ u^2E_- & 0 & 0 & -E_-B_+ \\ -E_-A_- & 0 & 0 & E_- \\ 0 & -E_+B_- & E_+ & 0 \end{pmatrix} , \\
\mathcal{E}_{pn}(u) &= -\mathcal{E}_{np}^T(u) ,
\end{aligned} \tag{A.4}
$$

with

$$
\begin{aligned}
A_\pm &= A_\pm(u) = u \pm \sinh ue^{-u} , \\
B_\pm &= B_\pm(u) = u \pm \cosh ue^{-u} , \\
C_\pm &= C_\pm(u) = u(1+u) \pm \sinh ue^{-u} , \\
D_\pm &= D_\pm(u) = u(1+u) \pm \cosh ue^{-u} , \\
E_\pm &= E_\pm(u) = \frac{1}{\sinh u\cosh u \pm u} .
\end{aligned} \tag{A.5}
$$

With the help of the adjoint set of functions

$$
\boldsymbol{w}_{lm0}^+ = \frac{1}{l(2l+1)} r^{-l} \left(\boldsymbol{A}_{lm} - \frac{2l+3}{2} \boldsymbol{B}_{lm} \right) , \tag{A.6}
$$

$$
\boldsymbol{w}_{lm1}^+ = \frac{i}{l(l+1)} r^{-l-1} \boldsymbol{C}_{lm} , \tag{A.7}
$$

$$
\boldsymbol{w}_{lm2}^+ = \frac{1}{(l+1)(2l+1)} r^{-l-2} \boldsymbol{B}_{lm} , \tag{A.8}
$$

with

$$\begin{aligned}
\boldsymbol{A}_{lm} &= lY_{lm}\boldsymbol{e}_r + \frac{\partial Y_{lm}}{\partial\theta}\boldsymbol{e}_\theta + \frac{1}{\sin\theta}\frac{\partial Y_{lm}}{\partial\phi}\boldsymbol{e}_\phi, && \text{(A.9)}\\
\boldsymbol{B}_{lm} &= -(l+1)Y_{lm}\boldsymbol{e}_r + \frac{\partial Y_{lm}}{\partial\theta}\boldsymbol{e}_\theta + \frac{1}{\sin\theta}\frac{\partial Y_{lm}}{\partial\phi}\boldsymbol{e}_\phi, && \text{(A.10)}\\
\boldsymbol{C}_{lm} &= \frac{1}{\sin\theta}\frac{\partial Y_{lm}}{\partial\phi}\boldsymbol{e}_\theta - \frac{\partial Y_{lm}}{\partial\theta}\boldsymbol{e}_\phi && \text{(A.11)}
\end{aligned}$$

where Y_{lm} are the spherical harmonics, we can calculate the matrix elements (see section 2.5.3)

$$\begin{aligned}
T^{\mathrm{R}}(ilm\sigma, jl'm'\sigma') &= \left\langle \boldsymbol{w}^{+}_{lm\sigma}(i)\delta_i \right| \boldsymbol{T}^{\mathrm{R}}(\boldsymbol{r},\boldsymbol{r}') \left| \boldsymbol{w}^{+}_{l'm'\sigma'}(j)\delta_j \right\rangle\\
&= \int \boldsymbol{w}^{*+}_{lm\sigma}(\boldsymbol{r}-\boldsymbol{r}_i)\frac{1}{a}\delta(|\boldsymbol{r}-\boldsymbol{r}_i|-a)\cdot\ldots\\
&\ldots \cdot\left[\int \boldsymbol{T}^{\mathrm{R}}(\boldsymbol{r},\boldsymbol{r}')\cdot\boldsymbol{w}^{+}_{l'm'\sigma'}(\boldsymbol{r}'-\boldsymbol{r}_j)\frac{1}{a}\delta(|\boldsymbol{r}'-\boldsymbol{r}_j|-a)\mathrm{d}^3r'\right]\mathrm{d}^3r\\
&= \int \boldsymbol{w}^{*+}_{lm\sigma}(\bar{\boldsymbol{r}})\frac{1}{a}\delta(\bar{r}-a)\cdot\ldots\\
&\ldots \cdot\left[\int \boldsymbol{T}^{\mathrm{R}}(\bar{\boldsymbol{r}}+\boldsymbol{r}_i,\bar{\boldsymbol{r}}'+\boldsymbol{r}_j)\cdot\boldsymbol{w}^{+}_{l'm'\sigma'}(\bar{\boldsymbol{r}}')\frac{1}{a}\delta(\bar{r}'-a)\mathrm{d}^3\bar{r}'\right]\mathrm{d}^3\bar{r}
\end{aligned} \qquad \text{(A.12)}$$

with $\bar{\boldsymbol{r}} = \boldsymbol{r}-\boldsymbol{r}_i$ and $\bar{\boldsymbol{r}}' = \boldsymbol{r}'-\boldsymbol{r}_j$. Inserting equation A.1, we obtain

$$\begin{aligned}
T^{\mathrm{R}}(ilm\sigma, jl'm'\sigma') &= \int \boldsymbol{w}^{*+}_{lm\sigma}(\bar{\boldsymbol{r}})\frac{1}{a}\delta(r'-a)\cdot\ \ldots\\
&\ldots \cdot\left[\int\left[\int e^{i\boldsymbol{q}\cdot(\bar{\boldsymbol{s}}+\boldsymbol{s}_i)}\hat{\boldsymbol{T}}^{\mathrm{R}}(\boldsymbol{q},\bar{z}+z_i,\bar{z}'+z_j)e^{-i\boldsymbol{q}\cdot(\bar{\boldsymbol{s}}'+\boldsymbol{s}_j)}\mathrm{d}^2q\right]\cdot\ldots\right.\\
&\ldots \left.\cdot\,\boldsymbol{w}^{+}_{l'm'\sigma'}(\bar{\boldsymbol{r}}')\frac{1}{a}\delta(\bar{r}'-a)\mathrm{d}^3\bar{r}'\right]\mathrm{d}^3\bar{r}.
\end{aligned} \qquad \text{(A.13)}$$

Defining $v = qz' = q\bar{z}' + qz_j =: \bar{v}'_j + \rho_j$ and $w = qz = q\bar{z} + qz_i =: \bar{w}_i + \rho_i$ with $\rho_{i/j} = qz_{i/j}$, we can express $f_i(v)$ in terms of $f_i(\bar{v}'_j)$ by a matrix operation

$$\begin{aligned}
\mathcal{F}(v) &= \mathcal{M}(\rho_j)\mathcal{F}(\bar{v}'_j),\\
\mathcal{F}(w) &= \mathcal{M}(\rho_i)\mathcal{F}(\bar{w}_i)
\end{aligned} \qquad \text{(A.14)}$$

with

$$\mathcal{M}(\rho) = \begin{pmatrix} f_1(\rho) & f_2(\rho) & 0 & 0\\ f_2(\rho) & f_1(\rho) & 0 & 0\\ f_3(\rho) & f_4(\rho) & f_1(\rho) & f_2(\rho)\\ f_4(\rho) & f_3(\rho) & f_2(\rho) & f_1(\rho)\end{pmatrix}. \qquad \text{(A.15)}$$

Thus from equations (A.2), (A.3) and (A.14) we find that $\hat{\boldsymbol{T}}^{\mathrm{R}}$ is a sum of terms, each of which is separable in the variables $\bar{v}'_j$ and $\bar{w}_i$, while the $\bar{\boldsymbol{s}}$ and $\bar{\boldsymbol{s}}'$ dependence in equation (A.13) is already separable, so the calculation of the matrix element reduces to a product of integrals, one over $\bar{\boldsymbol{r}}$ and one over $\bar{\boldsymbol{r}}'$. Explicit results for the integrals over $\bar{\boldsymbol{r}}$ and $\bar{\boldsymbol{r}}'$ in equation (A.13) are given in Ref. [55]. Therefore, to determine the matrix elements $T^{\mathrm{R}}(ilm\sigma, jl'm'\sigma)$, we have to solve the remaining integral over $\boldsymbol{q}$ in equation (A.13), which is calculated by quadrature. Note, that for $i = j$ equation A.13 is identical to the equation given in Ref. [55].

In order to obtain the whole matrix M (see section 2.5.3), we additional need the matrix elements $M_0(ilm\sigma, il'm'\sigma)$ and $M_1(ilm\sigma, jl'm'\sigma)$ $(i \neq j)$, which are given in Ref. [56] and [146], respectively.

List of Publications

[A] Sebastian Reddig & Holger Stark, *Cross-streamline migration of a semiflexible polymer in a pressure driven flow*, Journal of Chemical Physics, **135**, 165101 (2011)

[B] Sebastian Reddig & Holger Stark, *Nonlinear dynamics of spherical particles in Poiseuille flow under creeping-flow condition*, Journal of Chemical Physics, **138**, 234902 (2013)

References

[1] D. N. Breslauer, P. J. Lee, and L. P. Lee. *Mol. BioSyst.*, **2**:97, 2006.

[2] S.K. Sia and G.M. Whitesides. *Electrophoresis*, **24**:3563, 2003.

[3] M. B. Romanowski, A. R. Abate, A. Rotem, Holtze C., and D. A. Weitz. *Lab Chip*, **12**:802, 2012.

[4] H. Stone, A. Stroock, and A. Ajdari. *Annu. Rev. Fluid Mech.*, **36**:381, 2004.

[5] S. Köster, D. Steinhauser, and T. Pfohl. *J. Phys.: Condens. Matter*, **17**:4091, 2005.

[6] H. Yun, K. Kim, and W. G. Lee. *Biofabrication*, **5**(2):022001, 2013.

[7] R. D. Sochol, B. P. Casavant, M. E. Dueck, L. P. Lee, and L. Lin. *J. Micromech. Microeng.*, **21**:054019, 2011.

[8] G. F. Christopher and Anna S. L. *J. Phys. D: Appl. Phys.*, **40**:R319, 2007.

[9] J. L. M. Poiseuille. *Ann. Sci. Nat.*, **5**:111, 11836.

[10] G. Segré and A. Silberberg. *J. Fluid Mech.*, **14**:115, 1962.

[11] R. Fåhræus and T. Lindqvist. *Amer. J. Physiol.*, **96**:562, 1931.

[12] S. S. Kuntaegowdanahalli, A. A. S. Bhagat, and I. Papautsky. *Lab on a Chip*, **9**:2973, 2009.

[13] D. Di Carlo, J. F. Edd, D Irimia, and M. Tompkins. *Anal. Chem.*, **80**:2204, 2008.

[14] Z. Wu, B. Willing, J. Bjerketorp, J. Jansson, and K. Hjort. *Lab on a Chip*, **9**:1193, 2009.

[15] R. C. Jeffrey and J. R. A. Pearson. *J. Fluid Mech.*, **22**:721, 1965.

[16] T. W. Pan and R. Glowinski. *J. Comput. Phys.*, **181**:260, 2002.

[17] A. Karnis, H. L. Goldsmith, and S. G. Mason. *Can. J. Chem. Eng.*, **44**:181, 1966.

[18] D. Di Carlo, D. Irimia, R. G. Tompkins, and M. Toner. *Proc. Natl. Acad. Sci.*, **104**:18892, 2007.

[19] C. L. Darabaner and S. G. Mason. *Rheol. Acta*, **6**:273, 1967.

[20] E. S. Asmolov. *J. Fluid Mech.*, **381**:63, 1999.

[21] J. A. Schonberg and E. J. Hinch. *J. Fluid Mech.*, **203**:517, 1989.

[22] L. G. Leal. *Ann. Rev. Fluid Mech.*, **12**:435, 1980.

[23] C. Prohm, M. Gierlak, and H. Stark. *Phys. J. E*, **35**:80, 2012.

[24] J. K. G. Dhont. *An introduction to dynamics of colloids*. Elsevier Science, Amsterdam, 1996.

[25] H. L. Goldsmith and S. G. Mason. *The Microrheology of Dispersions in Rheology Theory and Applications*, **4**. Academic Press, New York, 1967.

[26] D. Semwogerere, J. F. Morris, and E. R. Weeks. *J. Fluid. Mech.*, **581**:437, 2007.

[27] T. Beatus, T. Tlusty, and R. Bar-Ziv. *Nature Physics*, **2**:743, 2006.

[28] P. Garstecki. *Nature Phys.*, **2**:733, 2006.

[29] T. Beatus, R. Bar-Ziv, and T. Tlusty. *Phys. Rev. Lett.*, **99**:124502, 2007.

[30] M. Baron, J. Bĺawzdziewicz, and E. Wajnryb. *Phys. Rev. Lett.*, **100**:174502, 2008.

[31] J. Bławzdziewicz and E. Wajnryb. *J. Phys.: Conf.Ser.*, **392**:012008, 2012.

[32] S. Bhattacharya. *J. Chem. Phys.*, **128**:074709, 2008.

[33] M. Zurita-Gotor, J. Bławzdziewicz, and E. Wajnryb. *Phys. Rev. Lett.*, **108**:068301, 2012.

[34] G. K. Batchelor and J. T. Green. *J. Fluid Mech.*, **56**:375, 1972.

[35] M. Zurita-Gotor, J. Bławzdziewicz, and E. Wajnryb. *J. Fluid Mech.*, **592**:447, 2007.

[36] C. W. Hsu and Y. L. Chen. *J. Chem. Phys.*, **133**:034906, 2010.

[37] D. Steinhauser, S. Köster, and T. Pfohl. *ACS Macro Letters*, **1**:541, 2012.

[38] R. Chelakkot, R. G. Winkler, and G. Gompper. *Europhys. Lett.*, **91**:14001, 2010.

[39] A. M. Slowicka, E. Wajnryb, and M. L. Ekiel-Jezewska. *Eur. Phys. J. E*, **36**:31, 2013.

[40] K. Sadlej, E. Wajnryb, and M. L. Ekiel-Jezewska. *J. Chem. Phys.*, **133**:054901, 2010.

[41] O. B. Usta, D. Perchak, A. Clarke, J. M. Yeomans, and A. C. Balazs. *J. Chem. Phys.*, **130**:234905, 2010.

[42] H. Noguchi and G. Gompper. *Proc. Natl. Acad. Sci.*, **102**:14159, 2005.

[43] G. Danker, P. Vlahovska, and C. Misbah. *Phys. Rev. Lett.*, **102**:148102, 2009.

[44] R. M. Jendrejack, E. T. Dimalanta, D. C. Schwartz, M. D. Graham, and J. J. De Pablo. *Phys. Rev. Lett.*, **91**:38102, 2003.

[45] R. M. Jendrejack, D. C. Schwartz, J. J. De Pablo, and M. D. Graham. *J. Chem. Phys.*, **120**:2513, 2004.

[46] O. B. Usta, J. E. Butler, and A. J. C. Ladd. *Phys. Fluids*, **18**:031703, 2006.

[47] O. B. Usta, J. E. Butler, and A. J. C. Ladd. *Phys. Rev. Lett.*, **98**:98301, 2007.

[48] J. P. Hernández-Ortiz, H. Ma, J. J. De Pablo, and M. D. Graham. *Phys. Fluids*, **18**:123101, 2006.

[49] D. Stein, F. H. J. Van Der Heyden, W. J. A. Koopmans, and C. Dekker. *Proc. Natl. Acad. Sci.*, **103**:15853, 2006.

[50] L. Fang, H. Hu, and R. G. Larson. *J. Rheol.*, **49**:127, 2005.

[51] A. Balducci, C. C. Hsieh, and P. S. Doyle. *Phys. Rev. Lett.*, **99**:238102, 2007.

[52] R. Chelakkot, R. G. Winkler, and G. Gompper. *J. Phys.: Condens. Matter*, **23**:184117, 2011.

[53] H. Ma and M. D. Graham. *Phys. Fluids*, **17**:083103, 2005.

[54] C. Sendner and R. R. Netz. *Europhys. Lett.*, **79**:58004, 2007.

[55] R. B. Jones. *J. Chem. Phys.*, **121**:483, 2004.

[56] B. Cichocki, R. B. Jones, R. Kutteh, and E. Wajnryb. *J. Chem. Phys.*, **112**:2548, 2000.

[57] A. J. C. Ladd. *Phys. Rev. Lett.*, **70**:1339, 1993.

[58] S. Chen and G. D. Doolen. *Annu. Rev. Fluid Mech.*, **30**:329, 1998.

[59] P. J. Hoogerbrugge and J. M. V. A. Koelman. *Europhys. Lett.*, **19**:155, 1992.

[60] R. D. Groot and P. D. Warren. *J. Chem. Phys.*, **107**:4423, 1997.

[61] A. Malevanets and R. Kapral. *J. Chem. Phys.*, **110**:8605, 1999.

[62] R. Kapral. *Advances in Chemical Physics*, **140**:89, 2008.

[63] T. Ihle and D. M. Kroll. *Phys. Rev. E*, **67**:066705, 2003.

[64] J. Happel and H. Brenner. *Low Reynolds Number Hydrodynamics*. Kluwer, Dordrecht, 1983.

[65] J. F. Brady and G. Bossis. *Annu. Rev. Fluid Mech.*, **20**:111, 1988.

[66] G. K. Batchelor. *An Introduction to Fluid Dynamics*. Cambridge University Press, Cambridge, 2000.

[67] L. D. Landau and E. M. Lifshitz. *Fluid Mechanics*. Pergamon Press, London, 1959.

[68] S. Vogel. *Life in Moving Fluids: The Physical Biology of Flow*. Princeton University Pres, Princeton, 1994.

[69] S. Kim and S. J. Karrila. *Microhydrodynamics: Principles and Selected Applications*. Butterworth-Heinemann, Boston, 1991.

[70] H. Faxén. *Annalen der Physik*, **373**:89, 1922.

[71] J. Rotne and S. Prager. *J. Chem. Phys.*, **50**:4831, 1969.

[72] J.M.J. den Toondor and P.R. Onck. *Artificial Cilia*. RSC Publishing, Cambridge, 1994.

[73] H. Yamakawa. *J. Chem. Phys.*, **53**:436, 1970.

[74] S. Köster. *Biological matter in microfluidic environment - from single molecules to self-assembly*. PhD thesis, Göttingen, 2006.

[75] M. Sharan and A. S. Popel. *Biorheology*, **38**:415, 2001.

[76] R. Skalak and P. I. Branemark. *Science*, **164**:717, 1969.

[77] H. Míguez, S. M. Yang, and G. A. Ozin. *Langmuir*, **19**:3479, 2003.

[78] H. N. Unni and C. Yang. *J. Colloid Interface Sci.*, **291**:28, 2005.

[79] E. Kumacheva, P. Garstecki, H. Wu, and G. M. Whitesides. *Phys. Rev. Lett.*, **91**:128301, 2003.

[80] J. R. Blake and A. T. Chwang. *J. Eng. Math.*, **8**:23, 1974.

[81] N. Liron and S. Mochon. *J. Eng. Math.*, **10**:287, 1976.

[82] C. Chang and R. L. Powell. *Part. Sci. Technol.*, **12**:189, 1994.

[83] S. Weinbaum, P. Ganatos, and Z. Yan. *Annu. Rev. Fluid Mech.*, **22**:275, 1990.

[84] B. Cichocki, B. U. Felderhof, K. Hinsen, E. Wajnryb, and J. Bławzdziewicz. *J. Chem. Phys.*, **100**:3780, 1994.

[85] S. Bhattacharya, J. Bławzdziewicz, and E. Wajnryb. *Phys. Fluids.*, **18**:053301, 2006.

[86] R. Schmitz and B. U. Felderhof. *Physica A*, **113**:90, 1982.

[87] H. Lamb. *Hydrodynamics*. Cambridge University Press, Cambridge, 1932.

[88] G. Perkins and R. B. Jones. *Physica A*, **171**:575, 1991.

[89] B. Cichocki, B. U. Felderhof, and R. Schmitz. *PhysicoChem. Hydrodyn.*, **10**:383, 1988.

[90] R. Schmitz and B. U. Felderhof. *Physica A*, **116**:163, 1982.

[91] B. Cichocki, M. L. Ekiel-Jezewska, and J. Wajnryb. *J. Chem. Phys.*, **111**:3265, 1999.

[92] D. J. Jeffrey and Y. Onishi. *J. Fluid Mech.*, **139**:261, 1984.

[93] D. J. Jeffrey. *Phys. Fluids A*, **4**:16, 1992.

[94] G. Bossis and J. F. Brady. *J. Chem. Phys.*, **80**:5141, 1984.

[95] B. Cichocki and R. B. Jones. *Physica A*, **258**:273, 1998.

[96] G. Wanner and E. Hairer. *Solving Ordinary Differential Equations II*. Springer-Verlag, Berlin, 1991.

[97] W. H. Press, S. A. Flannery, and W. T. Vetterling. *Numerical Recipes in C: The Art of Scientific Computing*. Cambridge University Press, Cambridge, 1992.

[98] G. Sewell. *The Numerical Solution of Ordinary and Partial Differential Equations*. Academic Press, San Diego, 1988.

[99] D. F. Griffiths and D. J. Higham. *Numerical Methods for Ordinary Differential Equations*. Springer-Verlag, Berlin, 2010.

[100] I. Karatzas and S. E. Shreve. *Brownian Motion and Stochastic Calculus*. Springer-Verlag, Berlin, 1991.

[101] J. Argyris, G. Faust, M. Haase, and R. Friedrich. *Die Erforschung des Chaos: Eine Einführung in die Theorie nichtlinearer Systeme*. Springer-Verlag, Berlin, 2010.

[102] D. S. Lemons. *An introduction to stochastic processes in physics: containing "On the theory of Brownian motion" by Paul Langevin*. Johns Hopkins University Press, Baltimore, 2002.

[103] R. F. Fox and G. E. Uhlenbeck. *Phys. Fluids*, **13**:1893, 1970.

[104] P. Mazur. *Physica A*, **110**:128, 1982.

[105] H. C. Öttinger. *Stochastic Processes in Polymeric Fluids*. Springer-Verlag, Berlin, 1996.

[106] W. Paul and J. Baschnagel. *Stochastic Processes: From Physiscs to Finance*. Springer-Verlag, Berlin, 1999.

[107] C. W. Gardiner. *Handbook of Stochastic Methods: For Physics, Chemistry, and the Natural Sciences*. Springer-Verlag, Berlin, 1986.

[108] W. T. Coffey, Y. P. Kalmykov, and J. T. Waldron. *The Langevin Equation With Applications to Stochastic Problems in Physics, Chemistry and Electrical Engineering*. World Scientific Publishing Co. Pte. Ltd., Singapore, 2004.

[109] U. Hassler. *Stochastische Integration Und Zeitreihenmodellierung: Eine Einführung mit Anwendungen aus Finanzierung und Ökonometrie*. Springer-Verlag, Berlin, 2007.

[110] H. Risken. *The Fokker-Planck Equation: Methods of Solution and Applications*. Springer-Verlag, Berlin, 1996.

[111] W. Hess and R. Klein. *Physica A*, **94**:71, 1978.

[112] M. Fixman. *J. Chem. Phys.*, **69**:1527, 1978.

[113] T. J. Murphy and J. L. Aguirre. *J. Chem. Phys.*, **57**:2098, 1972.

[114] M. Reichert. *Hydrodynamic Interactions in Colloidal and Biological Systems*. PhD thesis, Konstanz, 2006.

[115] M. Hütter and H. C. Öttinger. *J. Chem. Soc., Faraday Trans.*, **94**:1403, 1998.

[116] J. C. Butcher. *Numerical Methods for Ordinary Differential Equations*. John Wiley & Sons, New York, 2003.

[117] P. Grassia, E. J. Hinch, and L. C. Nitsche. *J. Fluid Mech.*, **282**:373, 1995.

[118] J. Wilkie. *Phys. Rev. E*, **70**:017701, 2004.

[119] G. H. Golub and C. F. Van Loan. *Matrix computations*. Johns Hopkins University Press, Baltimore, 1996.

[120] L. N. Trefethen and D. Bau. *Numerical linear algebra*. Society for Industrial and Applied Mathematics, Philadelphia, 1997.

[121] G. E. P. Box and M. E. Muller. *Ann. Stat. Mech.*, **29**:610, 1958.

[122] J. Bell. *Communications of the ACM*, **11**:498, 1968.

[123] M. P. Stevens. *Polymer chemistry: An introduction*. Oxford University Press, New York, 1999.

[124] R. M. Jendrejack, D. C. Schwartz, M. D. Graham, and J.J. De Pablo. *J. Chem. Phys.*, **119**:1165, 2003.

[125] R. Khare, M. D. Graham, and J. J. De Pablo. *Phys. Rev. Lett.*, **96**:224505, 2006.

[126] L. Cannavacciuolo, R. G. Winkler, and G. Gompper. *Europhys. Lett.*, **83**:34007, 2008.

[127] O. Kratky and G. Porod. *Rec. Trav. Chim. Pays-Bas.*, **68**:1106, 1949.

[128] P. S. Doyle and P. T. Underhill. *Handbook of Materials Modeling*, page 2619. Springer-Verlag, Berlin, 2005.

[129] L. D. Landau and E. M. Lifshitz. *Statistical Physics*. Pergamon Press, London, 1958.

[130] P. A. Wiggins and P. C. Nelson. *Phys. Rev. E*, **73**:031906, 2006.

[131] D. L. Ermak and J. A. McCammon. *J. Chem. Phys.*, **69**:1352, 1978.

[132] D. Frenkel and R. Eppenga. *Phys. Rev. E*, **31**:1776, 1985.

[133] B. U. Felderhof. *J. Chem. Phys.*, **137**:084906, 2012.

[134] J. Bławzdziewicz, M. L. Ekiel-Jezewska, and E. Wajnryb. *J. Chem. Phys.*, **133**:114703, 2010.

[135] B. U. Felderhof and A. Sellier. *J. Chem. Phys.*, **136**:054703, 2012.

[136] D. R. Mikulencak and J. F. Morris. *J. Fluid Mech.*, **520**:215, 2004.

[137] G. Subramanian and D. L. Koch. *Phys. Fluids*, **18**:074402, 2006.

[138] P. M. Kulkarni and J. F. Morris. *J. Fluid Mech.*, **596**:413, 2008.

[139] P. J. Mucha, S. -Y. Tee, D. A. Weitz, B. I. Shraiman, and M. P. Brenner. *J. Fluid Mech.*, **501**:71, 2004.

[140] S. Bhattacharya, J. Bławzdziewicz, and E. Wajnryb. *Physica A*, **356**:294, 2005.

[141] S. Bhattacharya, J. Bławzdziewicz, and E. Wajnryb. *J. Comput. Phys.*, **212**:718, 2006.

[142] J. P. Hernández-Ortiz, J. J. De Pablo, and M. D. Graham. *J. Chem. Phys.*, **125**:164906, 2006.

[143] J. W. Swan and J. F. Brady. *J. Fluid Mech.*, **687**:254, 2011.

[144] M. E. Staben, A. Z. Zinchenkom, and H. D. Robert. *Phys. Fluids*, **15**:1711, 2003.

[145] T. M: Squires and S. R. Quake. *Rev. Mod. Phys.*, **77**:977, 2005.

[146] B. U. Felderhof and R. B. Jones. *J. Math. Phys.*, **30**:339, 1989.

Zusammenfassung

In den letzten Jahrzehnten wurden nicht nur die Computerchips immer kleiner, auch die Größe von mikrofluidischen Geräten hat sich drastisch geändert. Diese sogenannten *Hosentaschenlabore* haben sich enorm weiterentwickelt und finden mittlerweile Anwendung in vielen physikalischen, biologischen oder chemischen Systemen. Ein wesentlicher Bestandteil all dieser Geräte ist die präzise Manipulation von suspendierten Teilchen auf der Mikrometerskala. Nicht nur für die Entwicklung solcher Geräte, sondern auch für ein tieferes Verständnis biologischer Vorgänge ist es von fundamentaler Bedeutung die nichtlineare Dynamik von kolloidalen Systemen in begrenzten Geometrien zu verstehen.

In dieser Arbeit präsentieren wir zwei verschiedene kolloidale Modellsysteme, bei denen die suspendierten Teilchen zwischen zwei parallelen Platten begrenzt sind und durch eine druckgetriebene *Poiseuille Strömung* aus dem thermodynamischen Gleichgewicht herausgetrieben werden.

Im ersten Modell untersuchen wir die *Cross-Streamline-Migration* von semiflexiblen Polymeren. Dazu beschreiben wir das Polymer mit dem Bead-Spring-Modell, eine diskrete Realisierung des bekannten Worm-Like-Chain Modells. Die hydrodynamischen Wechselwirkungen zwischen den Punktteilchen dieses Modells beschreiben wir mit dem *Zweiwand-Green-Tensor* der Stokesschen Gleichungen. Mit der Hilfe von Brownsche Dynamik Simulationen untersuchen wir die Schwerpunktverteilung des Polymers quer des Kanals. Unsere Ergebnisse reproduzieren die typische bimodale Verteilung, welche in früheren Experimenten und Simulationen beobachtet wurde. Um die Ursache dieser Verteilung besser zu verstehen, leiten wir die Smoluchowski Gleichung für die Schwerpunktverteilung her und analysieren die verschiedenen Anteile der Wahrscheinlichkeitsstromdichte, welche diese bimodale Verteilung verursachen. Im Gegensatz zu früheren Arbeiten, bei denen die ortsabhängige Diffusionskonstante des Schwerpunktes als Verursacher

der Migrationsbewegung weg von der Kanalmitte galt, identifizieren wir eindeutig den deterministischen Drift als Hauptverursacher. Wir zeigen sogar, dass der diffusive Anteil der Wahrscheinlichkeitsstromdichte immer mehr an Bedeutung verliert, je mehr wir die Biegesteifigkeit des Modellpolymers erhöhen. Als zweites System untersuchen wir die nichtlineare Dynamik kräftefreier kugelförmiger Kolloide, deren Durchmesser in der Größenordnung der Kanalbreite liegt. Im Gegensatz zum vorherigen System können wir hier nicht mehr das vereinfachte Modell von Punktteilchen annehemen. Demnach bestimmen wir die hydrodynamischen Wechselwirkungen über eine Multipolentwicklung um die endliche Ausdehnung der Teilchen zu berücksichtigen. Wir zeigen, dass zusätzlich zu den Trajektorien eines Teilchenpaares, welche bereits in begrenzter und unbegrenzter Scheerströmung beobachtet wurden, die begrenzte Poiseuille Strömung neue Klassen von Trajektorien entstehen lässt. Je nach Anfangsbedingungen und Teilchengröße, bewegen sich zwei Kugeln auf geschlossenen oder offenen Bahnen. Wir kategorisieren diese Trajektorien in einem Zustandsdiagramm und diskutieren wie die Ergebnisse des Zweiteilchensystems dazu beitragen die Stabilität in einer Reihe von vielen Teilchen zu verstehen.

Abstract

In the recent years, not only the physical size of computer chips decreased, also the size of microfluidic devices changed drastically. These so called Lab on a chip devices have seen great progress and find applications in many physical, biological or chemical systems. An essential part of all these devices is the precise manipulation of suspended particles on the micron scale. Therefore, it is of fundamental importance to understand the nonlinear dynamics of colloidal systems in confined geometries, not only for the development of such devices, but also to gain a better understanding of biological processes.

In this work we present two different colloidal model systems, where the suspended particles are confined between two planar walls and are driven out of equilibrium using the pressure driven *Poiseuille flow*.

In the first model, we investigate the *cross-streamline migration* of semiflexible polymers. We introduce the semiflexible polymer as a bead-spring chain, which is a discrete representation of the well known worm-like chain. We take the hydrodynamic interactions between the pointlike beads into account by the *two-wall Green tensor* of the Stokes equations. With the help of *Brownian dynamics simulations* we investigate the probability distribution of the center-of-mass of the polymer across the channel. Our simulations reproduce the typical bimodal distribution, as observed in previous experiments and simulations. To gain a better understanding of the origin of this distribution, we derive a Smoluchowski equation for the center-of-mass distribution and carefully analyze the different contributions to the probability current that causes the bimodal distribution. In contrast to previous studies, where the migration away from the centerline was explained by a position-dependent diffusivity, we clearly identify a deterministic drift current as the major cause for migration away from the centerline. We even show that diffusional currents due to a position-dependent diffusivity become less

important with increasing polymer stiffness.

In the second model, we investigate the dynamics of force- and torque-free spherical colloids, whose diameter is comparable to the distance of the two walls. In contrast to the previous model, we can no longer work with the simplified point particles. Instead we have to take the finite size of the spheres into account and determine the hydrodynamic interactions by a multipole expansion. In addition to the trajectories of a pair of particles, which were already observed in bounded and unbounded shear flow, we show that the bounded Poiseuille flow gives rise to new classes of trajectories resulting in cross-streamline migration. Depending on their initial positions and their size, two particles move along either closed or open trajectories (thus exhibiting bound or unbound states). We categorize these trajectories in a state diagram and discuss how the results on the two-particle system help to understand the stability of particle trains composed of several particles.

Danksagung

Es gibt eine Reihe von Menschen, bei denen ich mich bedanken möchte. Als erstes möchte ich mich bei meinem Doktorvater Prof. Dr. Holger Stark bedanken, der mir überhaupt erst meine Promotion ermöglicht hat. Er stand mir immer mit Rat und Tat zur Seite und gab mir stets die Freiheit meinen eigenen Weg zu gehen. Die konstruktiven Gespräche und Kritiken stellen einen wertvollen Beitrag dieser Arbeit dar.

Auch möchte ich mich für die freundlichen und konstruktiven Gespräche bei meinem Zweitbetreuer Prof. Dr. Alexander Mikhailov bedanken.

Mein Dank richtet sich auch an die ganze Arbeitsgruppe der AG Stark. Hervorheben möchte ich insbesondere Reinhard Vogel, Andreas Zöttl, Christopher Prohm, Katrin Wolff und Oliver Pohl, die mich immer wieder mit Ratschlägen unterstützt haben und mir beim Korrekturlesen geholfen haben.

Desweiteren bedanke ich mich bei der Deutsche Forschungsgemeinschaft, welche mich im Rahmen des Graduiertenkollegs GRK 1558 finanziell unterstützt hat.

Zu guter Letzt möchte ich mich bei meiner Familie bedanken, die mich immer unterstützt haben und mir motivierend beiseite stand.